Protection Scheme of an Integrated Photovoltaic and Type 3 Wind Turbines System

A Thesis

Presented in Partial Fulfillment of the Requirements for the

Degree of Master of Science

with a

Major in Electrical Engineering

in the

College of Graduate Studies

University of Idaho

by

Xiaoqing Chen

Major Professor: Brian K. Johnson, Ph.D.

Committee Members: Karen Frenzel, Ph.D.; Hangtian Lei, Ph.D.

Department Administrator: Joseph D. Law, Ph.D.

December 2019

Authorization to Submit Thesis

This thesis of Xiaoqing Chen, submitted for the degree of Master of Science with a Major in Electrical Engineering and titled "Protection Scheme of an Integrated Photovoltaic and Type 3 Wind Turbines System," has been reviewed in final form. Permission, as indicated by the signatures and dates below, is now granted to submit final copies to the College of Graduate Studies for approval.

Major Professor: _____ Date: _____
Brian K. Johnson, Ph.D.

Committee Members: _____ Date: _____
Karen Frenzel, Ph.D.

_____ Date: _____
Hangtian Lei, Ph.D.

Department Administrator: _____ Date: _____
Joseph D. Law, Ph.D.

Abstract

The increasing penetration of renewable energy sources into power grids has been driven by the rapid growth of both renewable technologies and economic benefits. Among various renewable generation sources, photovoltaic (PV) and wind energy have grown faster than others. Normally most installations use the same type of renewables integrated into a collector bus. In this thesis a system with different renewables, PVs and Type 3 WTGs integrated into the same collector bus is proposed for the greater usage of the renewable energy sources, especially in a resource rich area. A PV model using an averaged voltage source converter representation is designed and implemented, and the real power characteristic of the PV site with daily insolation and temperature variation in steady-state is investigated with the simulation in RTDS/RSCAD and data post-processed in MATLAB. A Type 3 WTG using averaged voltage source converters is also modelled for the integrated system. An overcurrent protection scheme using symmetrical components is applied on the collector feeder of the integrated PVs and Type 3 WTGs system, and the good performance is shown with the simulation results of the system response to unbalanced and balanced faults. The protection scheme is also verified with the fault responses when different wind speeds are among WTGs, and the same protection performance is achieved.

Acknowledgements

I thank my major advisor, Dr. Brian Johnson, for all his support throughout my research and Master's program.

I am thankful to Dr. Karen Frenzel, and Dr. Hangtian Lei for their patience and time to evaluate my work and thesis.

I am also thankful to the staff of the ECE department for their support.

Dedication

"Dedicated to my parents, Xinglan & Bangming Chen, for their endless support, and my husband Feng, for his constant encouragement."

Table of Contents

List of Tables

List of Figures

Acronyms

ANSI- American National Standards Institute

CAISO- California Independent System Operator

CT- Current transformer

DFIG- Doubly fed induction generator

DLG- Double line to ground

HPF- High pass filter

HVRT- High voltage ride through

IDMT- Inverse definite minimum time

IEEE- The Institute of Electrical and Electronics Engineers

IRENA- The International Renewable Energy Agency

LVRT- Low voltage ride through

LL- Line to line

LG- Line to ground

MPPT- Maximum power point tracking

NREL- National Renewable Energy Laboratory

PCC- Point of common coupling

PI- Proportional integral

PLL- Phase locked loop

PT- Potential transformer

PV- Photovoltaic

PWM- Pulse width modulation

RMS- Root mean square

RTDS- Real time digital simulator

RSCAD- RTDS simulator computer aided design

SCIG- Squirrel cage induction generator

SLG- Single line to ground

SSCI- Sub-synchronous control interactions

STC- Standard temperature condition

VSC- Voltage source converter

WRIG- Wound rotor induction generator

WTG- Wind turbine generator

Chapter 1 Introduction

With the global population increasing, the energy demand has reached unprecedented levels. Over eighty percent of global energy consumption is met with fossil fuels [1], which only exist in a limited supply in the earth. With the current usage rate the world reserves of oil will deplete in 50 years, and coal will last 150 years [2]. Mining and burning fossil fuels result in negative impacts on the environment and human health. The carbon dioxide emission from burning fossil fuels has been a leading contributor of climate change. These trends and predictions of climate change create an urgent need to develop renewable energy alternatives to burning fossil fuels.

By definition, renewable energy resources, such as wind and solar energy, are constantly replenished by the natural processes and will never run out. To support countries in their transition to a sustainable energy future, intergovernmental organizations were founded, such as the International Renewable Energy Agency (IRENA) [3]. These organizations promote the widespread adoption and sustainable use of all forms of renewable energy. Supportive policies and a dramatic fall in technology cost have led to the rapid growth of renewable energy technologies, in particular wind and solar photovoltaic.

1.1 Renewable Energy Growth

The global renewable energy deployment continues to expand significantly. Renewable generation increased at an annual average rate of 6.4% in the years between 2009 and 2014, and represented almost 60% of the electric power generation capacity added worldwide in 2016. Meanwhile non-renewable generation increased with a lower annual average growth rate of 2.6%. In 2015, renewable energy provided about 23.5% of all electricity generated, and 3.5% of the total came from wind energy and 1% from solar PV [3]. The global power

generation forecast from McKinsey Energy Insights shown in Figure 1-1 predicts that renewable generation will account for more than 50% of power supply post-2035 and grow to close to 75% by mid-century. In 2035 the total share of solar PV is predicted to be 29%, onshore wind 14%, and offshore wind 3% [4].

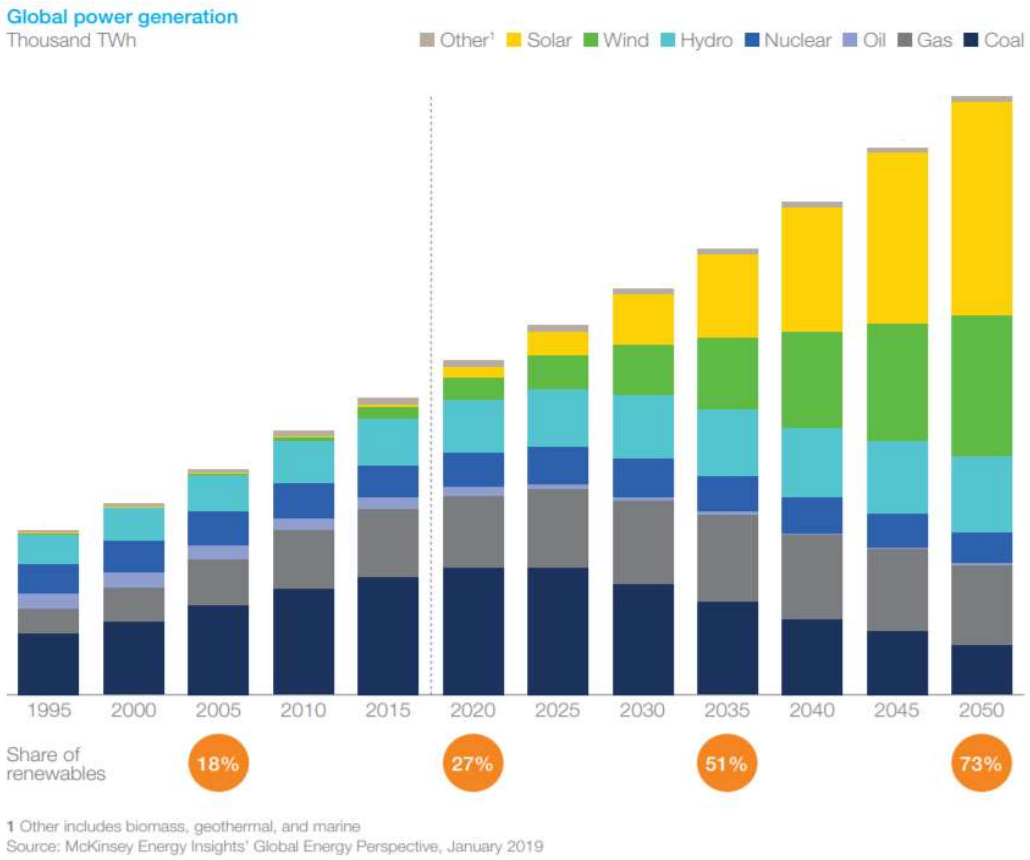

Figure 1-1. Predicted trends in global power generation [4].

This expansion was driven mainly by a combination of dedicated policies, technological advancement and falling costs. In the years between 2010 and 2017, the price of PV modules dropped by more than 80% and the cost of electricity from solar PV fell by almost 75%. The price of wind turbines dropped by about 50% over the same period, and the costs of onshore wind electricity fell by almost 25%. The average global prices resulting from solar PV and onshore wind auctions from 2010 to 2016 is shown in Figure 1-2.

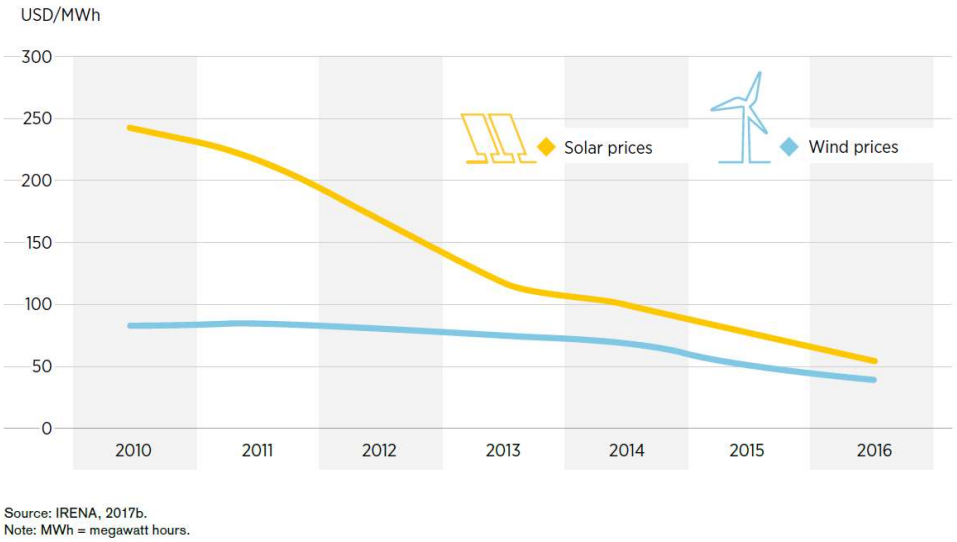

Figure 1-2. Average global prices resulting from solar PV and onshore wind auctions [3].

1.2 Research Objective

Increasing penetration of variable renewable generation into an electric grid is changing the ways power system operators manage their systems. Strategies for system integration of renewables, consisting of a coordinated sequence of measures, are crucial to minimize negative impacts, maximize benefits and improve the cost effectiveness of the power system [3]. Normally renewable generation sources are integrated into the power grid through a collector bus. The way that installations are normally built out results in a collector interfacing one type of generation. In this thesis a system integrated with both photovoltaic and Type 3 variable speed doubly fed induction generator (DFIG) wind turbine is introduced. This integration method with different type renewable generators on same collector bus provides an option for resource rich areas, potentially with less cost, and improves the flexibility of power system.

Variable wind and solar generation sources integrated into the power system via power electronics have different fault current characteristics than conventional synchronous generators, which has led to the need for either new protection schemes or for renewable generation to contribute fault current suitable for existing power system protection schemes to

operate. To address this concern, this work develops a protection scheme for the system with integrated photovoltaic and Type 3 wind turbine generator (WTG) sources that makes the system more reliable. Since photovoltaic generation and Type 4 WTG are fully converter based, the fault currents contributed from them are same, and limited and maintained by power electronics. Generally the fault current from Type 4 WTG will be slightly above rated current, around 1.1 to 1.2 pu, and mostly balanced. However the fault response of Type 3 WTG is affected by the crowbar circuit connected at the rotor for close-in faults. When the crowbar circuit is active, the fault applied directly to the WTG terminals would have 5 to 6 pu fault current contribution from the WTG, and the crowbar circuit shorts the rotor terminals or the DC link capacitor via an external resistor to dissipate all of the energy stored in the machine. When the crowbar is inactive and DFIG rotor power controller remains active, the fault current contribution of Type 3 WTG would be limited between 1.1 to 2.5 pu of the machine rated current. In this thesis the integrated system adopts photovoltaic generation and Type 3 WTG, instead of Type 4 WTG, to have a varied response.

In this research, a PV system with grid side voltage source converter is modelled, and a hybrid renewable generation integration system with two PVs and five Type 3 WTGs is simulated. The fault behavior of the system is studied, and the performance with an overcurrent protection scheme using symmetrical components on the collector feeder is investigated. The protection performance is verified in the case with mixed wind conditions.

1.3 Scope of the Thesis

This thesis aims to model an integrated PVs and Type 3 WTGs system and study the protection scheme performance on the collector feeder. Chapter 2 reviews photovoltaic technology including the structure of solar cells, modules and arrays, mathematical modelling

of PV and maximum power point tracking of PV cell output. This chapter also describes some grid codes for PV and the concept of solar smoothing. Chapter 3 introduces wind energy technology with different types of WTGs and their fault characteristics and examples of grid codes. Chapter 4 describes the PV generation model in RSCAD, including the averaged voltage source converter model and control schemes. A general AC grid model with a three-winding transformer collector station is also introduced in Chapter 4. Chapter 5 describes the RSCAD implementation of Type 3 WTG, including wound rotor machine, step up transformer and DC crowbar circuit.

In Chapter 6 the integrated system with one PV converter from Chapter 4 and one Type 3 WTG from Chapter 5 is implemented. MATLAB is used to retrieve instantaneous data from the RTDS simulation and process them in order to obtain the real power characteristic of PV model with daily insolation and temperature variation in steady-state. The system is expanded to integrate two PVs and five Type 3 WTGs and the normal operation of the system is tested. Chapter 7 reviews the existing protection schemes used in the research, including overcurrent relays and directional relays. Differential relays and distance relays are also briefly described in this chapter. In Chapter 8 an overcurrent protection scheme using symmetrical components is applied on the collector feeder protection in the integrated system with two PVs and five Type 3 WTGs. The sequence networks of the system are illustrated. The system responses for unbalanced and balanced faults are analyzed, and the protection performance with the mixed wind condition is verified. Chapter 9 summarizes and concludes the work done in this thesis and proposes future work based on the PV model and the integrated system.

Chapter 2 Photovoltaic Technology

2.1 Introduction

The photovoltaic effect is the process of converting sunlight directly into electricity using solar cells. The PV effect was discovered in 1954 at Bell Telephone [5]. Soon solar cells have long been used to power space satellites and smaller items like calculators and watches.

In the 1980s research into silicon solar cells paid off and solar cells began to increase their efficiency. In 1985 silicon solar cells achieved the milestone of 20% efficiency. Over the next decade, the photovoltaic industry experienced steady growth of installed systems, and the growth rates were between 15% and 20%, largely promoted by the remote power supply market. In the year 1997 a growth rate of 38% was achieved [5]. Today solar cells are recognized not only as a means for providing power and increased quality of life to those who do not have grid access, but they are also a significant means of environmental protection and sustainable development.

2.2 Solar Energy

Solar energy in one form or another is the source of nearly all energy on the earth [5]. The conventional power source fossil fuels is essentially just stored solar energy from millions of years ago. Besides PV, the renewable energy, biomass, wind energy and hydropower, all are different forms of energy derived from solar energy. PV is a simple and well known method of harnessing the solar energy. Because the process of PV directly converts the solar radiation into electricity, PV devices have advantages of no noise, limited pollution and few moving parts, making them robust, reliable and long lasting. Solar energy from PV is an important component of renewable energy and plays a key role in the modern power market.

2.3 Photovoltaic Solar Cells

2.3.1 PV Cell, Module and Array

Photovoltaic cells are manufactured using several types of semiconductor materials, for example silicon and germanium, which produce an electric charge when exposed to electromagnetic radiation in a range of wavelengths, such as in the case of direct sunlight. A single PV cell is small, typically producing about 1 or 2 watts of power at 0.5 of a volt. To boost the voltage output of PV cells, they are connected in series, and in parallel to increase current, forming larger units known as modules or panels. A typical module will have 36 or 72 cells connected in series. The module shown in Figure 2-1 has 36 cells connected in series to produce a voltage sufficient to charge a 12 V battery [5].

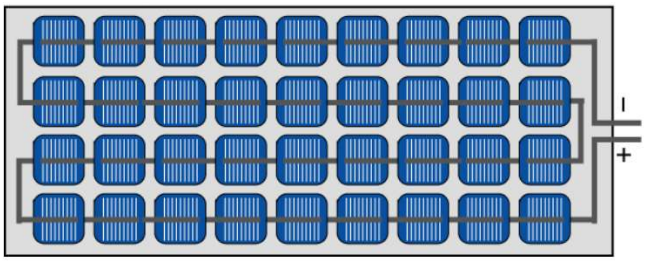

Figure 2-1. A typical module with 36 cells connected in series [5].

Modules can be used individually, or several can be connected to form arrays. The relationship of PV cell, module and array is illustrated in Figure 2-2. One or more arrays are connected to the electrical grid through a power converter as part of a complete PV system. Due to this modular structure, PV systems are size-flexible, small or large, to meet almost any electric power need.

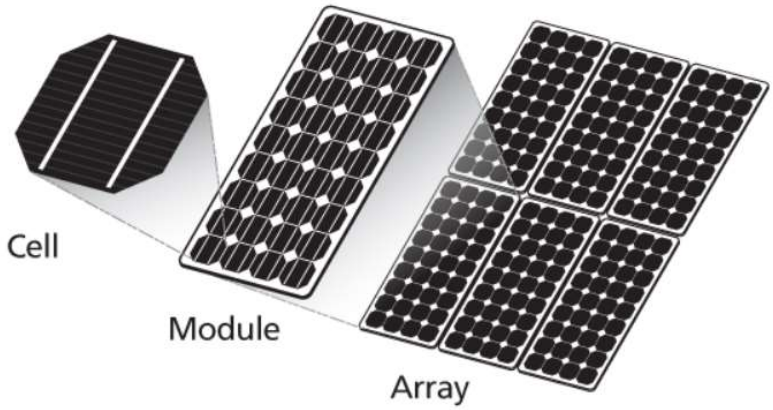

Figure 2-2. PV Cell, Module and Array [6].

2.3.2 Mathematical Model of PV Cell

An ideal PV cell can be electrically represented as a current source in parallel with a single diode. The behavior of PV cell is predominantly affected by the two parameters, irradiance and temperature. In order to accurately represent the nonlinear current-voltage diode characteristics, a single diode model with a shunt and series resistance was developed as shown in Figure 2-3. The model takes into account different properties of PV cell, including:

- The series resistance R_s is the sum of several structural resistances in the solar cell.
- The shunt resistance R_{sh} represents the leakage current of the semiconductor material resulting from the manufacturing process of the solar cell [7].

However this model has neglected recombination effect of diode.

To account for the recombination losses within the depletion region, a two diode model has been proposed [7], and the research in [8] shows that a two diode model possesses better accuracy than its single diode counterpart at low levels of irradiance. This section concentrates on the single diode model to maintain consistency with the PV model used for the research work of the thesis, which is available in a component provided with the simulation software.

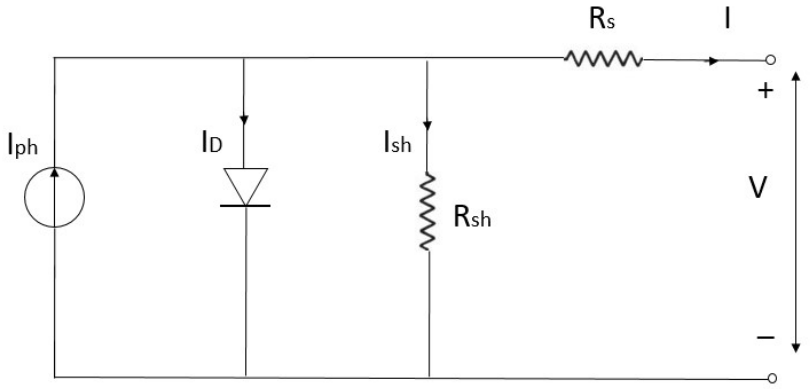

Figure 2-3. Single Diode PV Cell Model

Using the equivalent circuit of PV cell shown in Figure 2-3, the output current of the single diode model is given by:

$$I = I_{ph} - I_D - I_{sh} \tag{2-1}$$

Where I_{ph} is the photocurrent generated by a PV cell, which is directly proportional to solar irradiance. I_D is the diode current and defined by:

$$I_D = I_0(\exp\left(\frac{V+R_sI}{n_s n V_t}\right) - 1) \tag{2-2}$$

Where, I_0 is the diode reverse saturation current.

n_s is number of cells in series.

n is the diode ideality factor, a measure of how closely the diode matches the ideal diode equation.

V_t is the diode thermal voltage constant which is defined at any given temperature T (in K) by:

$$V_t = kTq \tag{2-3}$$

Where, q is the magnitude of an electron charge ($1.602176 \times 10^{-19}C$).

k is the Boltzmann's constant ($1.3806503 \times 10^{-23}J/K$).

The current across the shunt resistor, I_{sh}, is given in Equation (2-4).

$$I_{sh} = \frac{V+R_s I}{R_{sh}} \tag{2-4}$$

Substituting Equation (2-2) and (2-4) to Equation (2-1) results in Equation (2-5) which is the current-voltage relationship of the single diode model.

$$I = I_{ph} - I_0(\exp\left(\frac{V+R_s I}{n_s n V_t}\right) - 1) - \frac{V+R_s I}{R_{sh}} \tag{2-5}$$

In many publications the single diode model shown in Figure 2-3 is also termed as a single diode, five parameter model ($I_{ph}, I_0, n, R_s, R_{sh}$) [9].

The photocurrent, I_{ph} , in Equation (2-1) and (2-5) is defined by [8]:

$$I_{ph} = [I_{scr} + K_i(\Delta T)]\frac{G}{G_{STC}} \tag{2-6}$$

Where, $\Delta T = T_{cell} - T_{STC}$

T_{STC} is the temperature at the standard temperature condition (STC) which is normally taken at room temperature i.e. at $25℃$.

T_{cell} is the cell's operating temperature.

I_{scr} is the short-circuit current at STC.

K_i is the short-circuit temperature coefficient in $A/℃$.

G is the insolation at the surface area of a PV cell in W/m^2.

G_{STC} is the insolation at STC, which is normally taken as 1000 W/m^2.

The two parameters I_{scr} and K_i are provided by the manufacturer.

The output current-voltage (I-V) characteristic of the PV cell depends on the variation of the solar parameters with the given insolation, G, and temperature, T_{cell}, as described by Equations (2-5) and (2-6). Figure 2-4 shows the I-V curves for different G and T_{cell} values. With the increase of the solar insolation and temperature, the I-V curve also increases.

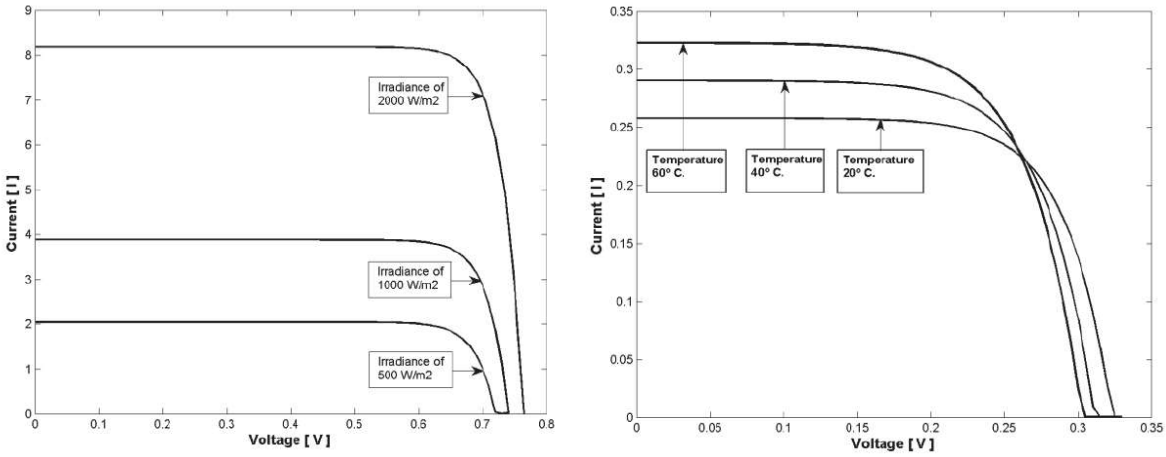

Figure 2-4. I-V curves for different solar insolation and temperature [10].

2.3.3 Maximum Power Point of PV cell

The I-V characteristics define potential operating point for the PV array at a given isolation and temperature as shown in Figure 2-5. The red curve represents the current-voltage relationship, and the blue curve shows the power-voltage characteristics. The curves range from the short circuit current (I_{sc}, 0) to the open circuit voltage (0, V_{oc}), with a knee point (I_{mp},V_{mp}) defined as the maximum power point where the PV array generates maximum electrical power, P_{max}.

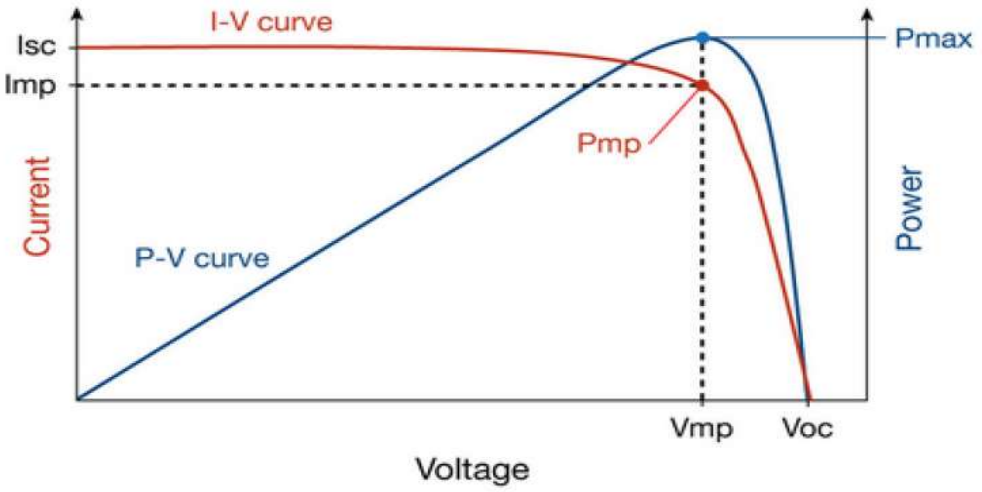

Figure 2-5. Maximum power point of PV cell [11].

The power converter interface for the PV array biases the voltage applied to the PV cells to ensure operation at the maximum power point. This control is referred to as a maximum power point tracking (MPPT) scheme, which will be described in Chapter 4.

2.4 Grid codes for Photovoltaic Installations

Grid code regulations are defined by power system operators to ensure safe and reliable operation of the power system. Grid codes outline the rights and the responsibilities of all the owners or operators of generators and loads connected to the transmission system. The worldwide rapid increasing penetration of renewable energy has raised some serious concerns regarding the negative impacts of large WTG plants and PV plants on the stability of power networks. Modern grid codes require WTGs not only withstand various grid disturbances, but also to contribute to network stability, support and provide ancillary services. For PVs, solar smoothing is increasingly becoming a major discussion point [12].

The grid codes for PV plants are primarily targeting the inverters and their control functionalities, and involve various scale PVs with different voltage levels. These grid codes mainly focus on voltage and frequency deviations, power quality (current harmonics and DC current injection), and anti-islanding. Typically local regulations imposed by the grid operators apply in specific countries but large efforts are made worldwide to create some standard grid requirements that can be adopted by many countries.

2.4.1 Voltage and Frequency Requirements

The PV inverters need to disconnect from the grid in case of severe abnormal grid conditions in terms of voltage and frequency. This response is to ensure the safety of utility maintenance personnel and the general public, as well as to avoid damage to connected equipment, including the photovoltaic system.

2.4.2 Current Harmonics

The PV system output should have low current distortion levels to insure that no adverse effects are caused to other equipment connected to the utility system.

2.4.3 DC Current Injection

DC current injection in the utility can saturate distribution transformers, leading to overheating, excessing reactive power demand and protection trips. For the conventional PV systems with galvanic isolation, this problem is minimized, but with the new generation of non-transformer coupled PV inverters increased attention is required in this matter.

2.4.4 Anti-islanding Requirements

Unintentional islanding for grid connected PV system takes place when a PV inverter does not disconnect after the feeder breaker for the local system is tripped. In the typical case of a residential electrical system co-supplied by a roof-top PV system, grid disconnection can occur as a result of a local fault detected by feeder protection or of an intentional disconnection of the line for maintenance [13]. In both situations, if the PV inverter does not disconnect the following consequences can occur.

- Re-closing the line or connected equipment can cause damage due to an out of phase closure.
- Safety hazard for utility line workers who assume de-energize lines for maintenance during islanding.

In order to avoid these serious consequences, safety measures to detect islanding condition called anti-islanding requirements have been issued and are embodied in standards.

2.5 Solar Smoothing

High levels of penetration of renewable generation displaces significant energy consumption that would have normally come from conventional generators. But unfortunately some renewables are intermittent in nature, most notably wind and PV. Figure 2-6 shows the net load (actual load minus PV and wind generation) for the California Independent System Operator (CAISO) for 2012-2013 with prediction through 2020. This is often referred to as the duck curve due to its shape as PV generation increases.

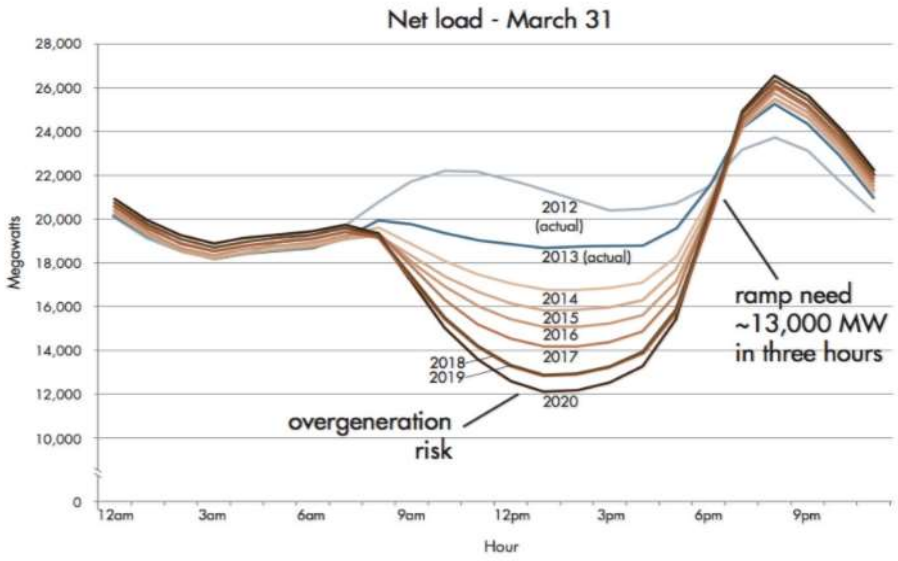

Figure 2-6. Duck curve for the CAISO System 2012-2022 [14].

Figure 2-6 shows the projected change in the net load of the CAISO system in a typical spring day from 2012 to 2020. The net load demand during the mid-day could drop from 21 GW to just 12 GW by the year 2020, while the net load could ramp by as much as 13 GW in three hours when the sun sets. This situation puts enormous challenges on the system operator in balancing load and generation and maintaining sufficient reserves to avoid system failures or blackouts.

The intermittent nature of solar generation is such that when passing clouds or system disturbance occurs, the energy output of many solar PV systems can drop sharply, and this manifests itself as a rapid transfer of load away from the PV generation and onto the spinning reserve generation equipment [12]. This rapid transfer of generation has impacts on the operation of the remaining power systems. The situation is even more serious for a small islanded power system. The ability of the power system to meet this sudden increase in load is dependent on two factors. One is the characteristics of the generator sets, and the other is how many load are online at the time of the event. Similarly when the cloud event finishes, there is a spike in PV system production and a sudden excess of energy flowing into the network caused by the sometimes rapid reappearance of the sun. Both these scenarios could have severe impact on voltage and frequency.

2.6 Summary

This chapter explains photovoltaic technology including the structure of solar cell, modules and arrays, single diode PV cell model and maximum power point of PV cell. The grid codes for PV and the concept of solar smoothing are also described.

Chapter 3 Wind Generation Technology

3.1 Wind Energy

Wind generation is a significant component of renewable energy generation source options. The use of wind energy to generate electricity can be traced back to the late nineteenth century [16]. However the technology was not mature to produce electricity efficiently until the 1980s. Over the past two decades, the development of a variety of wind power technologies have improved the efficiency of conversion and reduced the production costs. The size of wind turbines has increased to over 10 megawatts each, and the installation has been expanded from on land to offshore where more energy can be harvested with less impact on land use and wildlife.

Wind generation is the process of creating electricity using the wind that occurs naturally in the earth's atmosphere. When the wind blows past a wind turbine, its blades capture the wind's kinetic energy and rotate a machine, turning it into mechanical energy. This rotation turns an internal shaft connected to a gearbox, which increases the speed of rotation. The rotation spins a generator to produce electricity. Wind power can be characterized using Equation (3-1) as per [17].

$$P_{mech} = \frac{1}{2}\rho A {v_w}^3 \tag{3-1}$$

Where, P_{mech} is the mechanical power in W,

ρ is the air mass density in kg/m^3,

$A = \pi r^2$ is the turbine swept area in m^2,

r is the turbine radius in m,

v_w is the wind speed in m/s.

According to Betz's law no turbine can capture more than 16/27 of the kinetic energy [17]. The factor 16/27 (0.59) is called the Betz coefficient. This characteristic is independent of the design of wind turbine. Actual wind turbines achieve, at peak, 75-80% of the Betz limit.

$$P_{avail} = \frac{1}{2} C_P \rho A {v_w}^3 \tag{3-2}$$

Where, P_{avail} is the available power for conversion to electrical power,

C_P is the efficiency coefficient.

The method to convert the wind turbine output to electricity to inject into the power grid varies for different type of WTGs, and the classification will be discussed in the following section.

3.2 Types of Wind Turbine Generators

Wind turbine generators are broadly classified in the following four types:

- Type 1 – Fixed speed, squirrel cage induction generator
- Type 2 – Variable slip, wound rotor induction generator with variable rotor resistance
- Type 3 – Variable speed, doubly-fed induction generator with active rotor-side converter
- Type 4 – Variable speed generator with full converter interface

In addition to these four types of WTGs, one other wind energy system, Type 5 WTG, is also discussed in this section.

3.2.1 Type 1 WTG

The schematic diagram of Type 1 WTG is illustrated in Figure 3-1. A squirrel cage induction generator (SCIG) is used, and its rotational speed is determined by the grid frequency, the generated power and the number of poles of the stator winding. At different wind speeds within a narrow operating range, the generator speed varies within 1% of its rated speed [16]. The speed range of the generator is so small that this system is often known as a fixed speed WTG.

A gearbox is required to match the speed difference between the turbine and generator such that the generator can deliver its rated power at the rated wind speed. A capacitor bank is required to compensate the reactive power drawn by the induction generator. Because of the simplicity, Type 1 WTG has low manufacturing and maintenance costs, and reliable operation. The most common point of failure is the gear box. However the system delivers the rated power to the grid only at its rated wind speed, leading to low energy conversion efficiency at other wind speeds. Type 1 WTG also requires a sturdy mechanical design to absorb high mechanical stresses [16]. This type WTGs are rarely deployed in new installations.

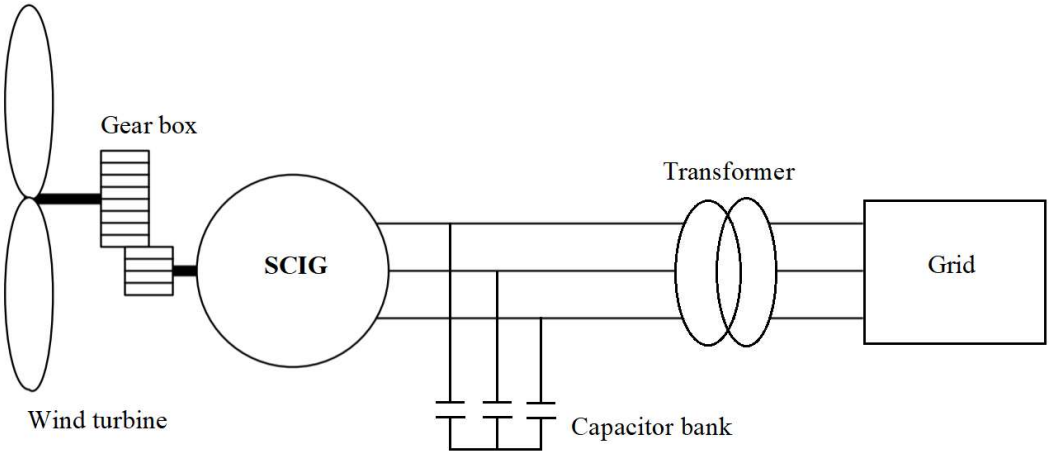

Figure 3-1. Schematic diagram of Type 1 wind turbine generator

3.2.2 Variable Speed Wind Turbines

Type 2, 3 and 4 are all variable speed wind turbines. Comparing with the fixed speed WTG, variable speed WTGs can achieve maximum energy conversion efficiency over a wider range of wind speeds. The turbine can continuously adjust its rotational speed according to the wind speed. This ability increases the energy conversion efficiency and reduces mechanical stress caused by wind gusts. Also variable speed WTGs have a positive impact on the design of the structure and mechanical parts of the turbine, enabling the construction of larger wind turbines.

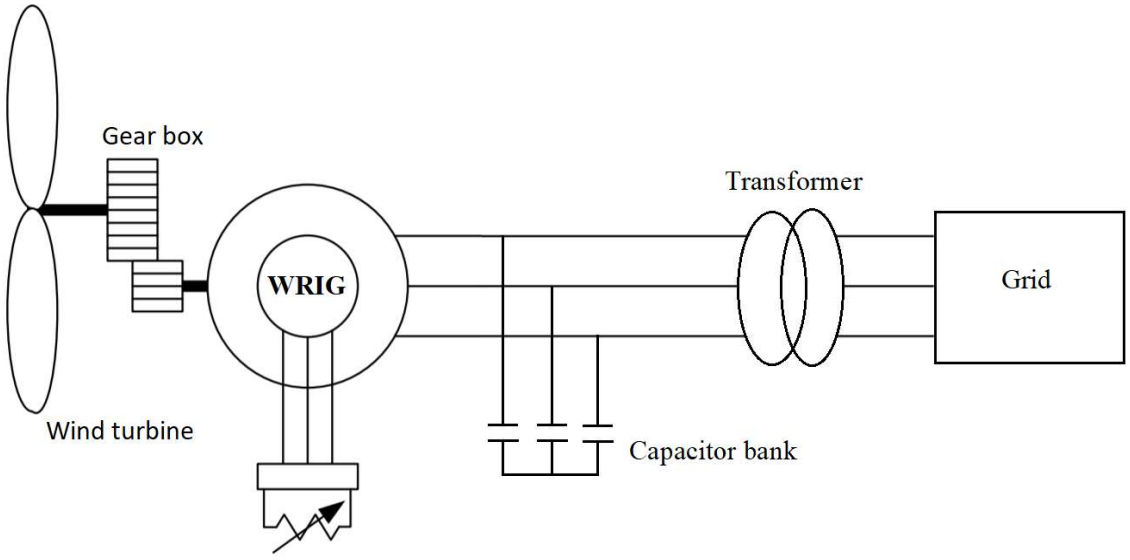

Figure 3-2. Schematic diagram of Type 2 wind turbine generator

3.2.2.1 Type 2 WTG

Figure 3-2 presents the schematic diagram of Type 2 WTG, wound rotor induction generator (WRIG) with a variable resistance in the rotor circuit. The change in the rotor resistance affects the torque-speed characteristic of the generator as shown in Figure 3-3, enabling limited variable speed operation of the turbine. The speed adjustment range is typically limited to about 10% above the synchronous speed of the generator [16]. With limited variable speed operation, a Type 2 WTG can capture more power from the wind, but has energy loss in the rotor resistance at higher wind speeds. This configuration also requires a capacitor bank for reactive power compensation.

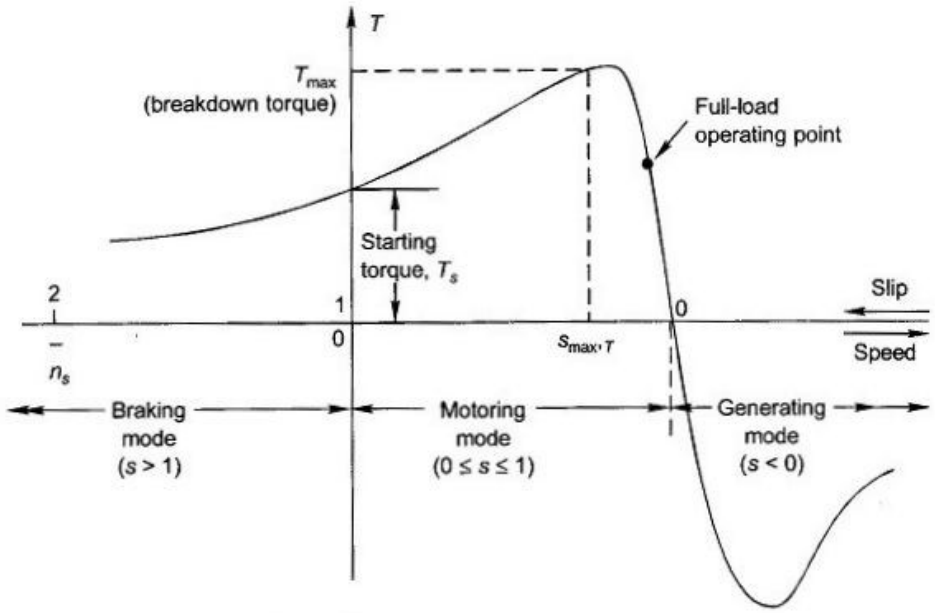

Figure 3-3. Torque-speed characteristic of induction machine [18] .

3.2.2.2 Type 3 WTG

The schematic diagram of Type 3 WTG system is shown in Figure 3-4. A doubly fed induction machine is a wound rotor induction machine with its stator windings directly connected to the grid and its rotor windings connected to the grid through a converter. The converter includes two parts, the rotor side voltage source converter (AC/DC) and the grid side converter (DC/AC). A capacitor connected on the DC side of the converter acts as a temporary DC voltage source. These converters adjust the power factor of the WTG system. There is no need for a capacitor bank since the reactive power required by the machine is provided by changing the rotor excitation voltage by means of a PWM controlled rotor side converter. The converters only have to process the slip power in the rotor circuits, which is approximately 30% of the rated power of the generator at the limits of typical wind speed range for Type 3 WTGs, resulting in reduced converter cost in comparison to Type 4 WTG with full-capacity converters [16]. The use of two voltage source converters in Type 3 WTGs allows bidirectional

power flow in the rotor circuit and increases the speed range of the generator. Compared to Type 1 and 2 WTGs, Type 3 WTG extends generator speed range to ±30% of synchronous speed, improves overall power conversion efficiency, and enhances dynamic performance. These features have made Type 3 WTGs widely accepted in the market for on shore applications.

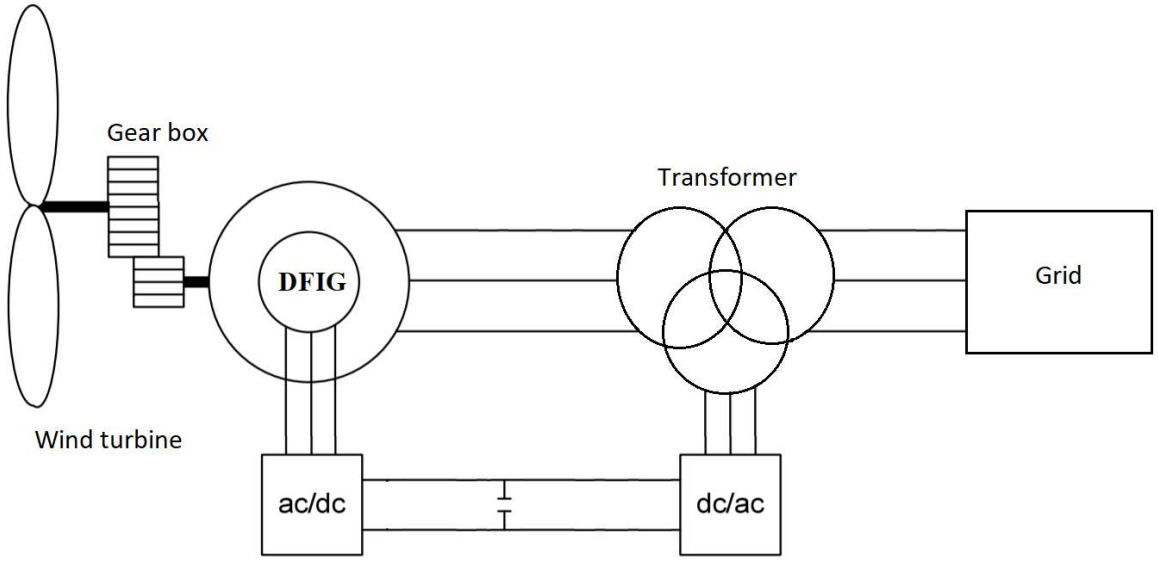

Figure 3-4. Schematic diagram of Type 3 wind turbine generator

3.2.2.3 Type 4 WTG

A Type 4 WTG is connected to the grid via the full converter interface, and the schematic diagram is shown in Figure 3-5. Squirrel cage induction generators, and permanent magnet synchronous generators (PMSG) have all found applications in this type of configuration with a power ratings of over 10 megawatts. The power rating of the converter is normally the same as that of the generator. In Type 4 PMSG WTG, a diode bridge rectifier is used to face the generator terminals and a VSC is needed to face the grid. However in Type SCIG WTG, either two-level voltage source converters or three-level neutral point clamped converters connected in a back-to-back configuration are most commonly used. With the use of the power converter,

the generator is fully decoupled from the grid, and can operate in a wide speed range without need for a gearbox. This also enables the system to perform reactive power compensation at lower wind speeds.

Type 4 WTGs are preferred for offshore generation since they have less maintenance need due to not having a gearbox or having a simpler one than is needed by a Type 3 WTG. Also having a generator without a wound field reduces maintenance needs. Type 4 WTG have the highest power ratings over 10 megawatts to reduce number of turbines needed offshore. Type 3 WTGs are more common on shore because they have lower costs, but Sub-Synchronous Control Interactions (SSCI) [15] problems are becoming a bigger issue.

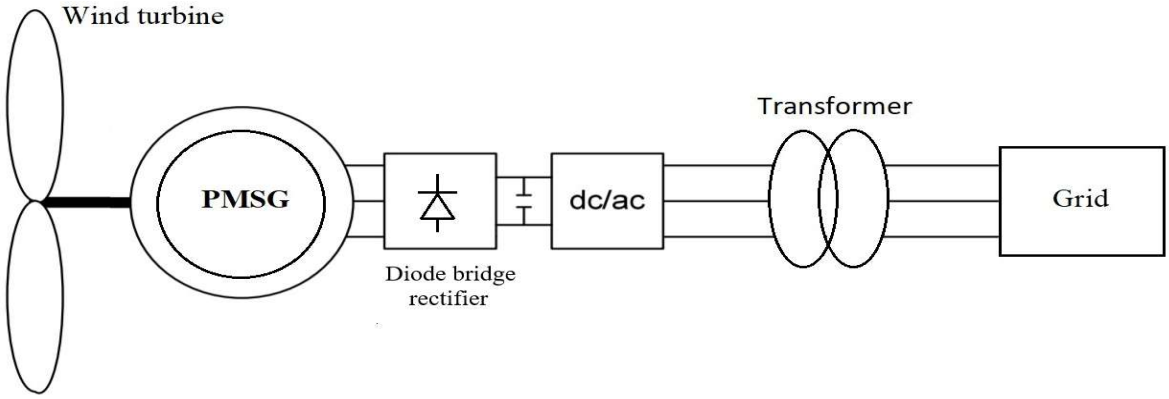

(a) Type 4 PMSG WTG

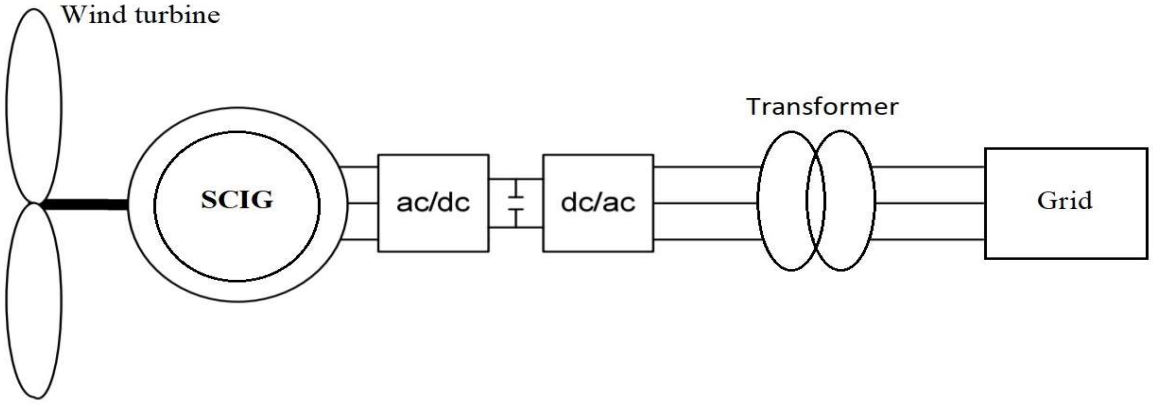

(b) Type 4 SCIG WTG

Figure 3-5. Schematic diagram of Type 4 wind turbine generator

3.2.3 Type 5 WTG

In [19] a wind energy system was described, and the schematic diagram is illustrated in Figure 3-6. This system was referred as a Type 5 WTG. Unlike other four standard types of WTGs, it has not been used in application. In this configuration variations in wind turbine speed are compensated in the hydraulic transmission instead of gearbox. A synchronous generator, operating at a fixed speed (corresponding to the grid frequency), can be directly connected to the grid via a circuit breaker. The reactive power is controlled by the field current. During an AC short circuit, the Type 5 WTG exhibits classical synchronous generator behavior.

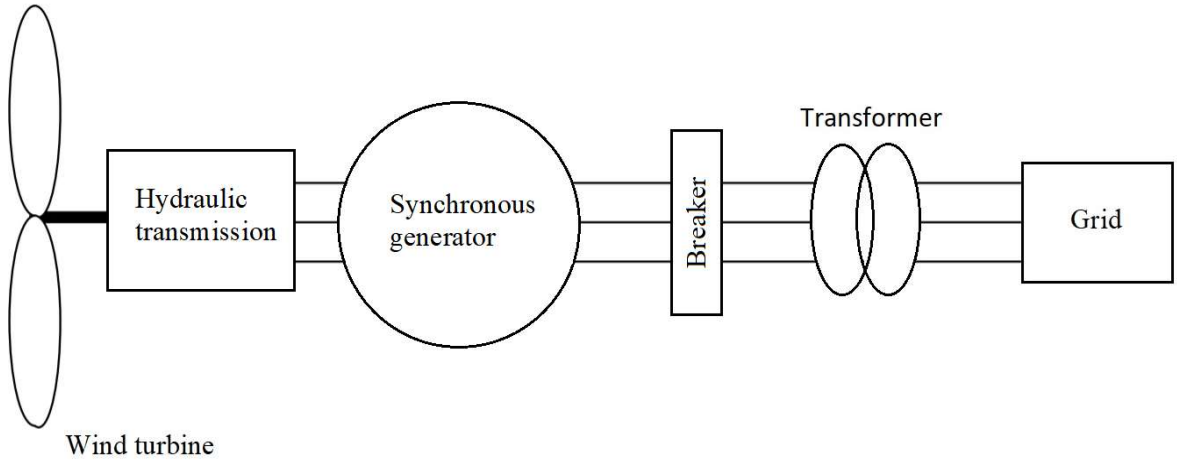

Figure 3-6. Schematic diagram of Type 5 Wind turbine generator

3.3 Fault Characteristics of WTGs

The fault response of WTGs to short circuits on the ac system depends mainly on the type of WTG. The fault characteristics of Type 1 and Type 2 WTGs are essentially the same as those of large induction machines used in industrial applications, while the fault characteristics of Type 3 and 4 WTGs are dominated by the WTG controls.

In short circuit calculations, a Type 1 WTG can be represented as a voltage source behind the direct axis sub-transient inductance (locked rotor inductance) of the SCIG. A Type 1 WTG can contribute short circuit current up to the value of its locked rotor current which is usually on the order of 5 to 6 pu on its current base for a few cycles [20].

Type 2 WTGs have the similar short circuit behavior to Type 1 WTGs when the external resistance control is at minimum resistance value, short-circuiting the generator rotor. But if the control action is enabled at or shortly after fault inception, the insertion of the full external roto resistance limits the fault current [20].

The fault response of Type 3 WTG is largely affected by the crowbar circuit connected at the rotor. In order to survive severe faults, crowbar circuit is added to short the rotor terminal or the DC link capacitor via an external resistor to dump all the extra energy stored in the machine. When the crowbar circuit shorts the rotor terminal, the DFIG will act like Type 2 WTG, while shorting the DC link capacitor will retain rotor current regulation. When the crowbar circuit is active, the fault applied directly to the WTG terminals would have 5 to 6 pu fault current contribution from the WTG. When the crowbar is inactive and DFIG rotor power controller remains active, the fault current contribution of Type 3 WTG would be limited between 1.1 to 2.5 pu of the machine rated current.

Since Type 4 WTGs employ full stator power rated converters as the interface to the grid, the fault current from WTG will be limited to slightly above rated current, around 1.1 to 1.2 pu for most vendors, and is usually balanced positive sequence, unity power factor current. This limitation is affected by the power converter control, and is generally necessary to protect the power semiconductor switches [20]. Since PV generations has the same converter interface

connected to the grid, the fault contribution of PV generation is same as that of Type 4 WTG. The integrated system of this thesis did not adopt Type 4 WTGs to have a more varied response.

Type 5 WTGs exhibit typical synchronous generator behavior during grid short circuits. The generator contribution to grid faults can be calculated from the machine parameters, which are obtainable from the generator manufacturer.

3.4 Grid Codes for WTGs

In order to reduce the effects of high degrees wind power penetration on power system stability in response to faults or other events, grid codes have been developed in different countries. There is no a common grid code applied in all countries. Even in one country, grid codes sometimes change in different jurisdictions. In this section grid codes are discussed on a general basis and not particular to any jurisdiction. These grid codes have been extended to PV generation connected to the bulk energy system in many jurisdictions.

3.4.1 Voltage and Frequency Requirements

Wind power plants are required to operate within a range around the rated voltage and frequency at the PCC and avoid disconnection due to transient disturbances. Typically this requirement is described using different zones of voltage magnitude or frequency versus time.

- Continuous operation within a limited range below and above the rated operating voltage magnitude or frequency.
- Time-limited operation with possible reduced power output over extended time ranges during faults, the recovery period following fault and in response to other dynamic disturbances.

3.4.2 Reactive Power Control

Reactive power is required for the voltage stability, and a voltage sag due to a load change or disturbance requires positive reactive current injection. Some grid codes require large wind power plants to provide reactive power support during the fault period and exhibit fast active power recovery during the supply voltage restoration [12], especially for Type 1 and 2 installations. Some vendors control converters to supply reactive power to increase local voltage to enable the generation to meet the ride through requirements.

3.4.3 Fault Ride-Through Requirements

Grid faults result in local voltage sags or swells, which have led to tripping of wind power plants, which can potentially unbalance the grid and may yield local blackouts. As wind power constitutes a significant part of the total network generation, the disconnection of wind power plants under voltage disturbances was viewed unacceptable. The grid codes were adapted to require wind power plants to continue uninterrupted operation under voltage sags according to given voltage-time profiles as introduced in Section 3.4.1. Such requirements became referred to as low voltage ride-through (LVRT) capability. Under voltage swell circumstances, the requirement for wind power plants to withstand without disconnection is commonly referred to as high voltage ride-through (HVRT) capability. The voltage ride through requirements represent minimum performance requirements. If the WTG or PV generation is able to keep operating longer without damaging the equipment, they are allowed to do so. An example of typical voltage ride-through requirements is illustrated in Figure 3-7. WTGs are required to set their controls and relays to remain connection through low voltage fault conditions, including least 9 cycles at 0V for the characteristics in this figure. During the high voltage conditions, such as a voltage equal to or higher than 1.175 pu but less than 1.2 pu, the characteristics in

Figure 3-7 require the WTG to stay connected for up to 0.2 second. If the overvoltage continues, the WTG is allowed to trip if there is risk of equipment damage.

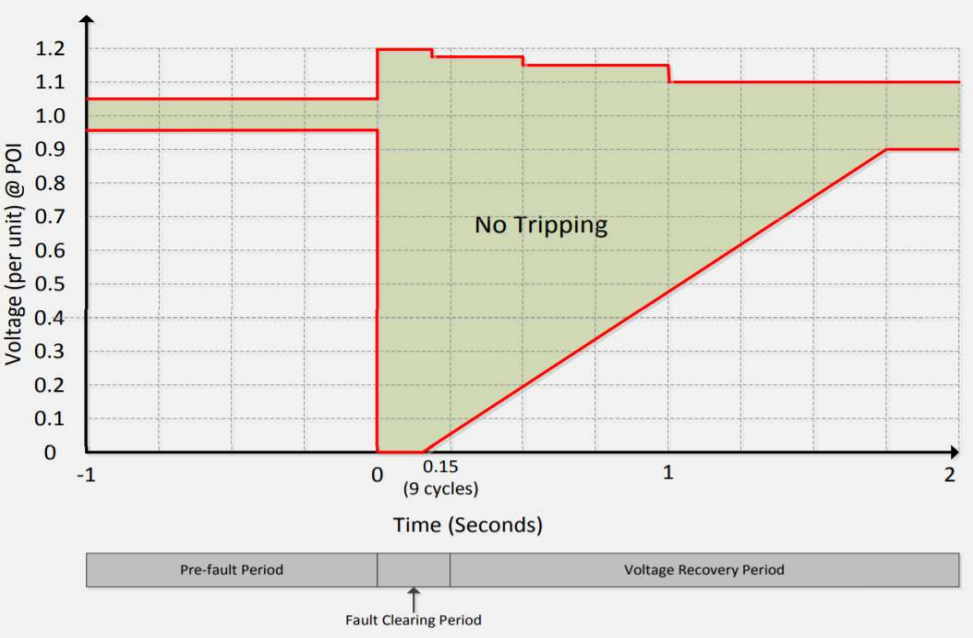

Figure 3-7. Typical voltage ride-through requirements [21].

3.5. Summary

This chapter introduces wind energy technology, the models for different types of WTGs and their fault characteristics. Three common grid codes for WTGs are also described.

Chapter 4 Modeling of Photovoltaic System

4.1 Objective

The objective of this chapter is to develop a model for the PV system and design controls for the grid connected voltage source converter (VSC). The implemented model uses averaged VSC models, where outer control loop and inner current control loop are designed. The model implemented in this chapter is used in the proposed integrated PV and Type 3 WTG system.

4.2 Simulation Software

In this research two simulation software tools are used, Real Time Digital Simulator (RTDS) with the RSCAD graphical interface, and MATLAB. RTDS simulator operates continuously in real time to allow a real-time interface to external protection and control hardware. The simulated power system can run in a manner similar to a real power system. As simulation parameters are modified, the user can watch the power system respond in real time. The modeled power circuit and control system are created using a graphical user interface. The input/output cards integrated in the hardware allow the simulator to be interfaced with external equipment.

The RTDS simulator provides the user the real-time simulation results, however this feature limits the analysis of results on the scale of time. MATLAB can be used to retrieve instantaneous data from the simulation results of RTDS and post-process them on line.

4.3 PV System Model

The schematic diagram of a grid-connected PV system is shown in Figure 4-1. The AC grid block will be described in detail in Section 4.8. The PV array model available in RSCAD is shown in Figure 4-2, where the estimation of maximum power point (Vmppe) is enabled. The model represents how the insolation level and temperature affect the output DC voltage and

current, which are converted to AC through a three-phase DC/AC voltage source converter. The goal of grid converter control system design is to operate within grid standards and codes specified for power quality and reliability. As the topology of the actual control systems is not available to make a detailed simulation model due to the manufacturer's intellectual property, so a reasonable approximation is implemented. In this research an averaged, non-switching, converter model is adopted and the controls are designed to function in the synchronous dq reference frame. Designs for anti-islanding detection and harmonic mitigation [11] are not included in the implementation.

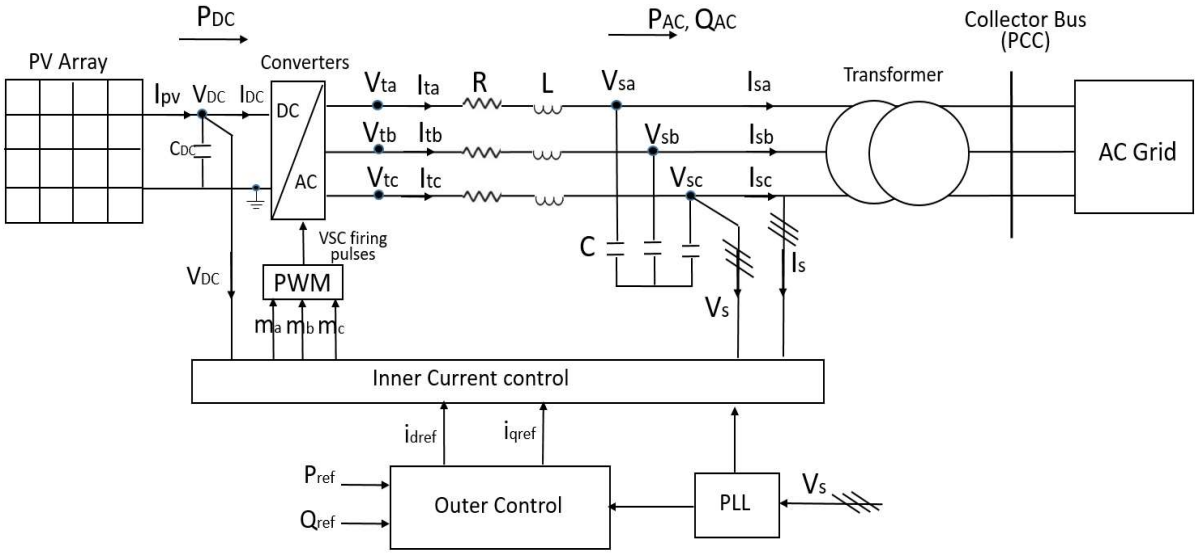

Figure 4-1. Grid-connected PV system.

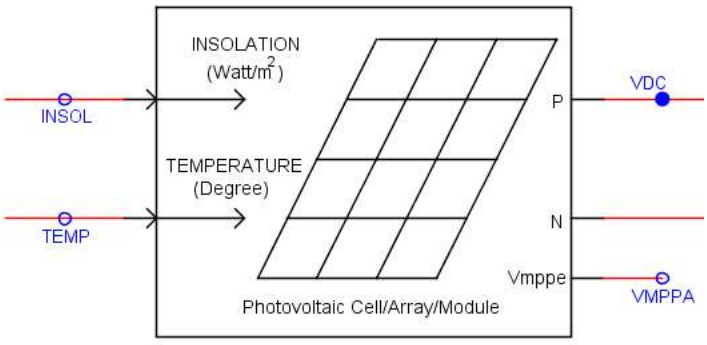

Figure 4-2. RTDS PV array model.

The PV system parameters used in the RSCAD implementation in this research are listed in Table 4-1.

Table 4-1. Parameters in PV system.

PV power rating	1.77 MW
DC voltage rating	2 kV
DC side filter capacitance	5000 μF
AC Frequency	60 Hz
AC side filter reactance R	120 mH
AC side filter resistance L	4 mΩ
AC side filter Capacitance C	2500 μF
Transformer MVA rating	2.5 MVA
Transformer LV winding (Wye)	0.48 kV
Transformer HV winding (Delta)	13.2 kV
Transformer leakage reactance	0.15 pu
Transformer no load losses	0.001 pu

4.4 Averaged VSC model

The grid converter is considered as a half-bridge based, three-phase, two-level voltage sourced converter with three legs of switches as shown in Figure 4-3. The fundamental component of the AC-side voltage is controlled based on a pulse-width modulation (PWM) technique. For a phase a, the half-bridge converter operates based on the alternate switching of S1 and S4.

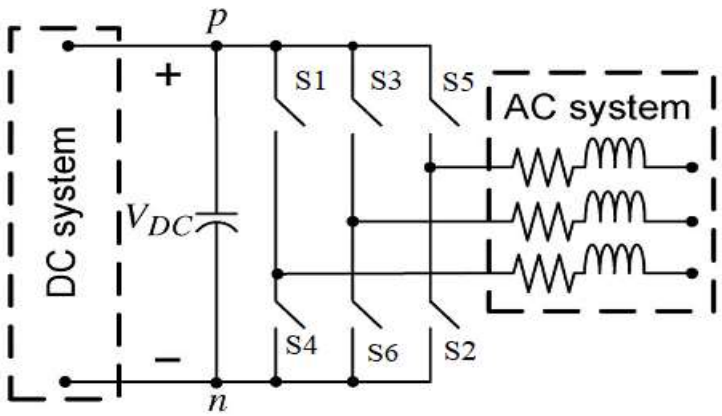

Figure 4-3. Schematic diagram of the three-phase, two-level VSC [17].

In the PWM strategy, a high frequency triangular waveform carrier signal on the order of 5-10 kHz is compared with the low frequency modulating signal at power system frequency. The intersections of the carrier and the modulating signals determine the switching instants of S1 and S4. The PWM process is illustrated in Figure 4-4. The switched model approximates the steady-state and dynamic behavior of a converter, since it doesn't include blanking time, turn-on/turn-off behavior and losses. A switching model of the converter represents the switch state changes of each device as shown in Figure 4-3.

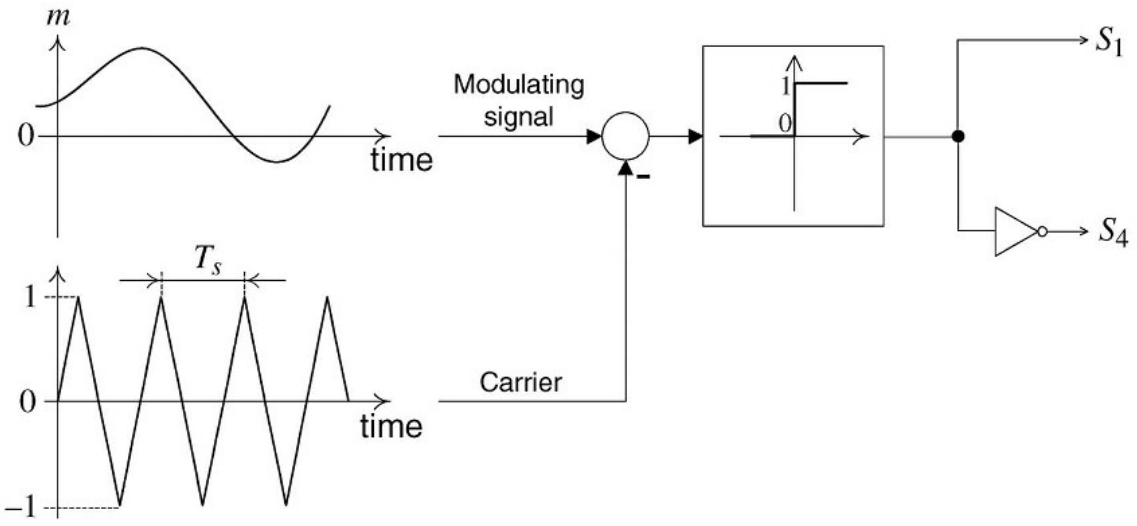

Figure 4-4. Schematic diagram of a PWM scheme for two-level VSC [17].

The switched model can represent the steady-state and dynamic behavior of the converter, along with an approximation of switching behavior where that is needed for high frequency interactions with the local system. In many cases the slower dynamics of the behavior of outer control loop variables is of more interest for power system studies, rather than the dynamics of the high frequency switching values. In an averaged model the converter dynamics can be described as a function of the modulating signal, reducing complexity of the converter model, and the ability to model larger system is available. In the reference [17], the detailed circuit

analysis describes the averaged model for a PWM switched VSC. The relationships between the voltage and current of DC and AC sides for the VSC can be used directly for the control system implementation. An averaged model for a single phase DC/AC is shown in Figure 4-5. The model could also be used to represent a DC/DC converter with a suitable modulating functions, $m(t)$.

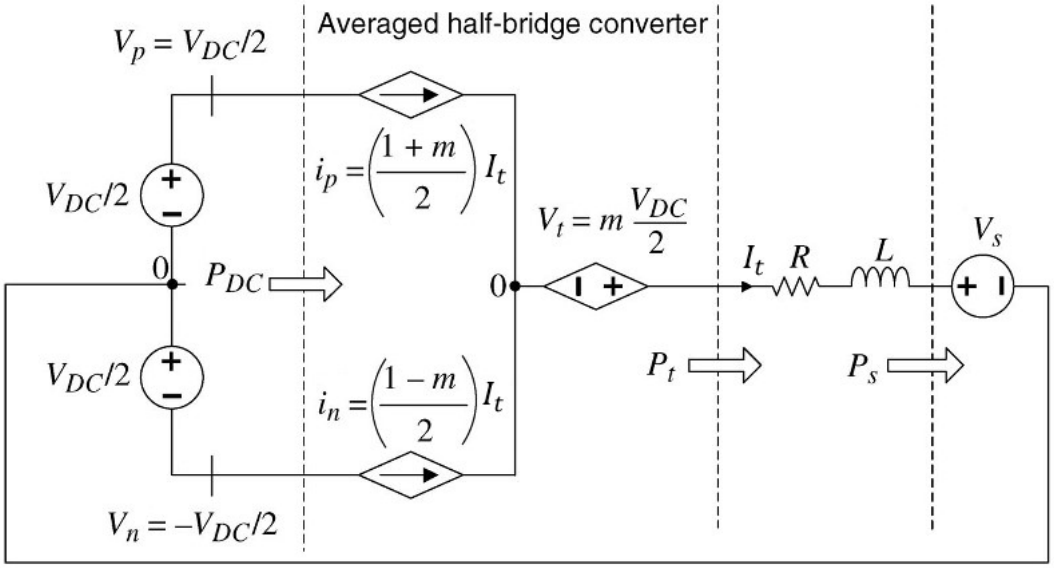

Figure 4-5. Averaged single phase equivalent circuit of the half-bridge converter [17].

The equivalent circuit is based on Equations (4-1) through (4-4),

$$V_t = m\frac{V_{DC}}{2} \tag{4-1}$$

$$i_p = (\frac{1+m}{2})I_t \tag{4-2}$$

$$i_n = (\frac{1-m}{2})I_t \tag{4-3}$$

$$P_t = P_{DC} = m\frac{V_{DC}}{2}I_t \tag{4-4}$$

Where, V_t is the AC side terminal voltage,

I_t is the AC side current,

P_t is the AC side active power,

V_{DC} is the DC side terminal voltage,

i_p and i_n are the DC side currents,

P_{DC} is the DC side active power,

m is the modulating signal, which describes the shape of desired output voltage.

The single phase averaged model for a half-bridge DC/AC converter can be extended to a three-phase model, which is implemented in RSCAD as shown in Figure 4-6, which uses the relationships presented in Equation (4-1) to (4-3) on each phase.

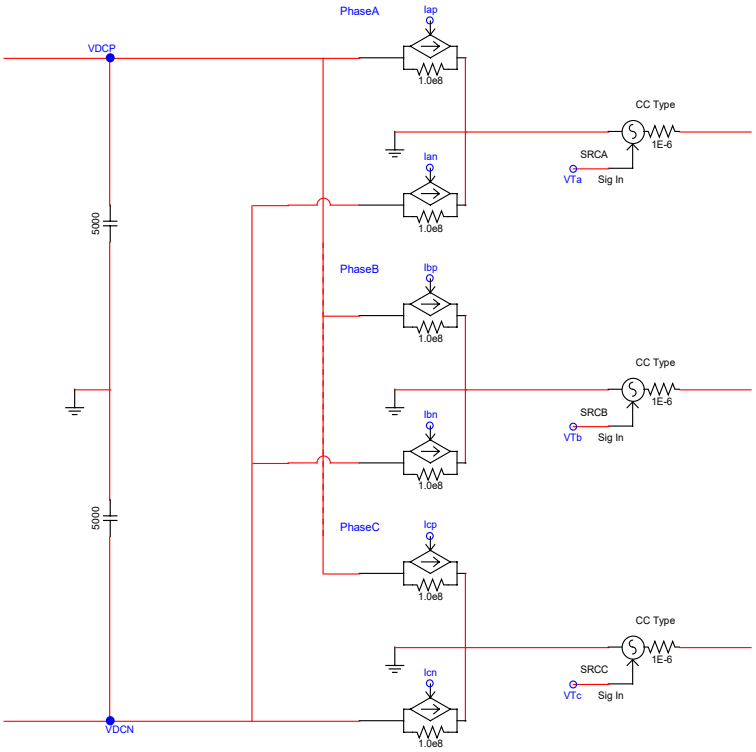

Figure 4-6. Circuit of averaged DC/AC converter modeled in RSCAD.

RTDS also provides a three-phase averaged DC/AC model as a pre-built component in RSCAD as shown in Figure 4-7. This model requires three-phase AC side voltage signal V_t

defined in Equation (4-1) as the input control signal, it still needs the modulating signal m to generate V_t and hence does not reduce the complexity of the model.

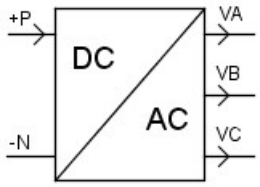

Figure 4-7. RTDS Averaged DC/AC VSC model.

There is no essential difference between the two half-bridge averaged models shown in Figure 4-6 and Figure 4-7. Both models require the modulating signals from other control loops. However, since the averaged model provided in RSCAD integrates the AC side filter, it is used for the simulation to reduce the number of circuit components.

4.5 Park's Transformation

Park's transformation converts the time domain components of a three-phase system in an abc reference frame to direct, quadrature, and zero ($dq0$) components in an arbitrary rotating reference frame. For balanced three-phase variables, the direct and quadrature axis components are constant if the reference frame is rotating at synchronous frequency, and the zero component is 0. For this reason Park's transformation is also known as a three-phase to two-axis transformation. It was introduced initially for the analysis of three-phase synchronous machines to eliminate the effect of time varying inductances to simplify calculation. Due to the slow variation of voltage and current, the Park's transformation to the synchronous reference frame is used in the control system of three-phase converters to reduce the control complexity.

To create an a-phase to d-axis alignment, Park's transformation can be represented by Equation (4-5).

$$\begin{bmatrix} d \\ q \\ 0 \end{bmatrix} = \frac{2}{3} \begin{bmatrix} \cos(\theta) & \cos(\theta - \frac{2}{3}\pi) & \cos(\theta + \frac{2}{3}\pi) \\ -\sin(\theta) & -\sin(\theta - \frac{2}{3}\pi) & -\sin(\theta + \frac{2}{3}\pi) \\ \frac{1}{2} & \frac{1}{2} & \frac{1}{2} \end{bmatrix} \begin{bmatrix} a \\ b \\ c \end{bmatrix} \quad (4\text{-}5)$$

Where,

a, b and c are the instantaneous variables of the three-phase system in the abc reference frame.

d and q are the instantaneous components of the two-axis system in the rotating reference frame.

θ is the angle of the rotational transformation: $\theta(t) = \omega * t + \theta_0$.

The phasor relationship of Equation (4-5) is illustrated in Figure 4-8. For stationary frame the value of θ is 0, and for a rotating reference frame it is ωt, where ω is the rotational speed of the dq reference frame relative to the abc frame. In the VSC applied in PV system, the

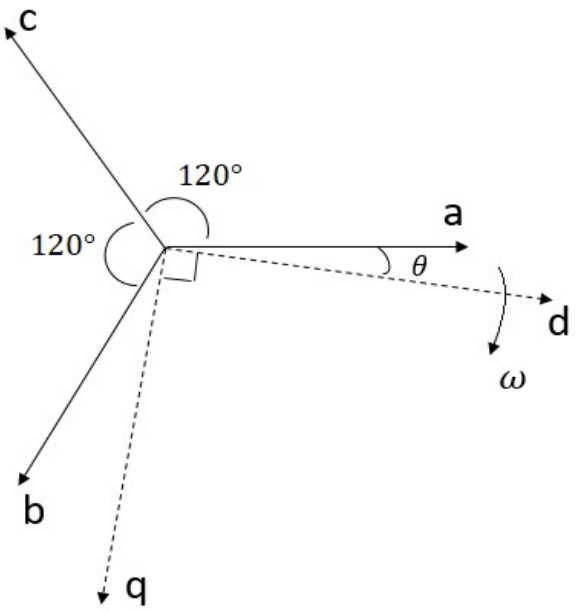

Figure 4-8. Park's transformation a-phase to d-axis alignment.

reference angle θ is calculated from the frequency of AC grid. A phase locked loop (PLL) is used to synchronize the converter control system to the AC grid voltage measured at the PCC [22]. The built-in RTDS blocks used for PLL, Park's transformation and inverse transform from the abc frame to the dq reference frame are shown in Figure 4-9.

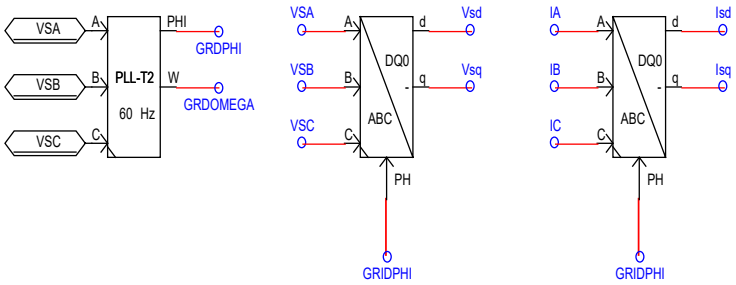

Figure 4-9. RTDS blocks for PLL, Park's transformation and inverse transform.

The complex power of three-phase system calculated in the phase domain can be given by the equation:

$$S_{3ph} = P_{3ph} + jQ_{3ph} = V_a I_a^* + V_b I_b^* + V_c I_c^* \tag{4-6}$$

When the three-phase quantities transform to $dq0$ components with an a-phase to d-axis alignment shown in Equation (4.5), Equation (4-6) changes to (4-7) and (4-8).

$$P_{3ph} = \frac{3}{2}(V_d I_d + V_q I_q + V_0 I_{0p}) \tag{4-7}$$

$$Q_{3ph} = \frac{3}{2}(V_q I_d - V_d I_q + V_0 I_{0q}) \tag{4-8}$$

Where, V_d is aligned with the positive peak voltage of a-phase at the PCC.

V_q has the value of 0.

Equation (4-7) and (4-8) can be simplified with a balanced three-phase set in which the value of zero components are 0.

$$P_{3ph} = \frac{3}{2}(V_d I_d) \tag{4-9}$$

$$Q_{3ph} = \frac{3}{2}(-V_d I_q) \tag{4-10}$$

In normal operation, it is common to measure voltages and calculate V_d and V_q. If P_{3ph} and Q_{3ph} are given as commands, Equation (4-9) and (4-10) can be arranged as current reference equations.

$$I_d = \frac{2}{3V_d} P_{3ph} \tag{4-11}$$

$$I_q = -\frac{2}{3V_d} Q_{3ph} \tag{4-12}$$

According to Equation (4-11) and (4-12), the currents on d / q axes can be regulated by open loop real/reactive power commands, and this relationship will be used in the controls, described in the following section.

4.6 Outer Control Loop

A hierarchical control scheme is used. A fast inner control loop performs closed loop current regulation to determine modulating functions m_a, m_b and m_c. The current references are generated by a slower outer control loop. One option for the outer control loops is to obtain the reference values for the currents on dq axis from the set point references for real and reactive power. In most renewable generation applications the VSC regulates the DC bus voltage. If the PV generation is higher than the AC power output, the dc voltage will rise. A DC bus controller will increase P_{ref} to bring V_{DC} to set point. A similar control can be used to regulate ac voltage magnitude by controlling Q_{ref}.

4.6.1 DC Bus Voltage Regulation

For the PV inverter application, the DC bus voltage is regulated to a reference value obtained from the maximum power point tracking control of the PV array. As shown in Figure 4-10, V_{DC}^2 is regulated by comparing it with the V_{DCref}^2 [23], the error signal is controlled by a proportional–integral (PI) controller or compensator which is used to improve steady-state

error without affecting the transient response. The d-axis current control reference, i_{dref}, is obtained from P_{ref}.

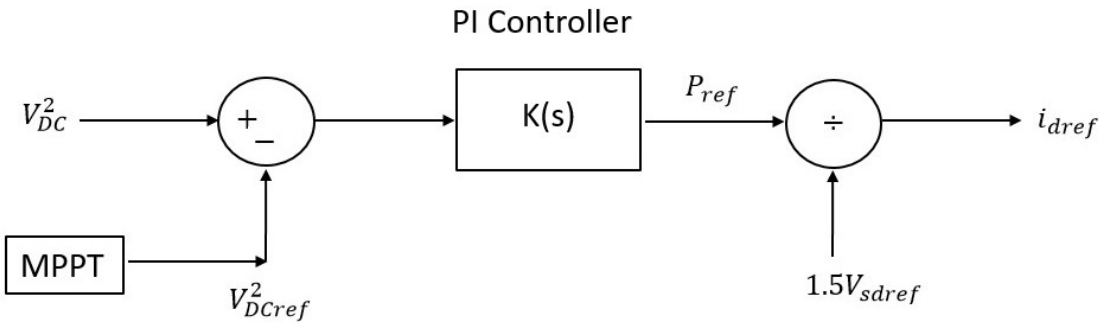

Figure 4-10. DC bus voltage control for d-axis current reference.

The RSCAD implementation of DC bus voltage control for d-axis current reference is presented in Figure 4-11. In this case V_{DCref} is the MPPT voltage which can be obtained from MPPT block or PV array model provided by RTDS. The purpose of the MPPT model is to follow the maximum power point as it changes with the ambient operating conditions of the PV generation system, the insolation level and temperature. The MPPT voltage control implementation as shown in Figure 4-11 is a direct way to choose the dc voltage from the built-in MPPT model (Vmppt) or PV array model (Vmppa). The built-in MPPT model uses the dc voltage and current generated from PV array as inputs to track the maximum power point and outputs the dc voltage at that point.

The PI controller uses the feedback information to reduce the remaining difference between the deviation of actual measured value (V_{DC}^2) from the set-point (V_{DCref}^2) and the feedback value. The transfer function of PI controller can be written as:

$$K(s) = K_p + \frac{K_i}{s} \tag{4-13}$$

The proportional gain K_p and the integral gain K_i are determined by the below two equations.

$$K_p = \frac{L}{\tau} \tag{4-14}$$

$$K_i = \frac{R}{\tau} \tag{4-15}$$

Where R and L are the resistance and inductance values of the VSC interface reactor between the converter terminals and the PCC and the time constant τ is a design parameter based on desired response.

The reference d-axis voltage V_{sdref} is the voltage of a-phase at the PCC and can be calculated from Equation (4-16) in steady state.

$$V_{sdref} = \frac{\sqrt{2}}{\sqrt{3}} V_{rms} \tag{4-16}$$

Where V_{rms} is the desired rms value of the voltage at the PCC, and the nominal value is 480V for this PV system.

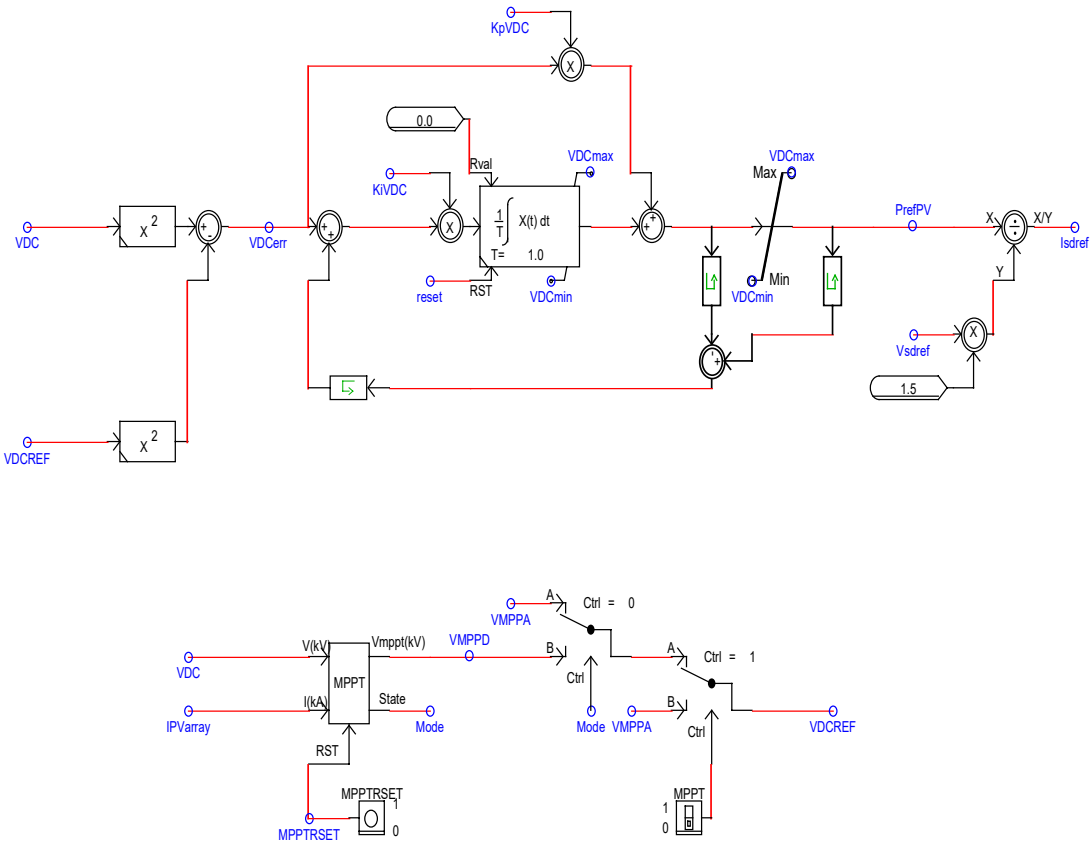

Figure 4-11. DC bus voltage regulation for d-axis current reference implemented in RSCAD.

4.6.2 AC Bus Voltage Regulation

The q-axis current reference, i_{qref}, can be set to a fixed value. Typically to maintain close to unity power factor regulation, i_{qref} is set to zero. The current reference can also be set based on a desired Q_{ref} using Equation (4-12). In addition current reference i_{qref} can also be obtained from an AC bus voltage regulation loop if the VSC is programmed to provide grid voltage support functions. Figure 4-12 shows the control block diagram of this regulation method. A PI controller is also used for control compensation, and the implementation in RSCAD is illustrated in Figure 4-13.

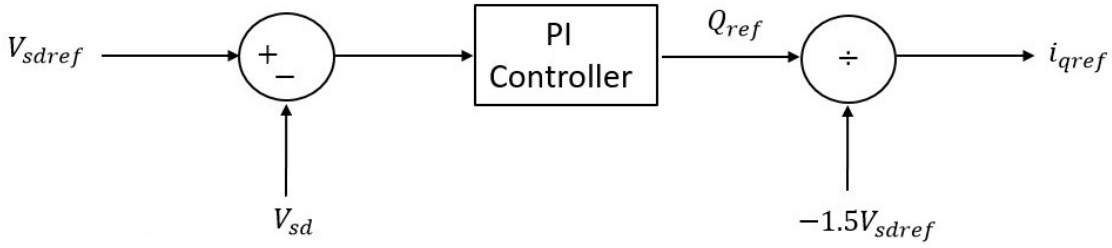

Figure 4-12. AC bus voltage control for q-axis current reference.

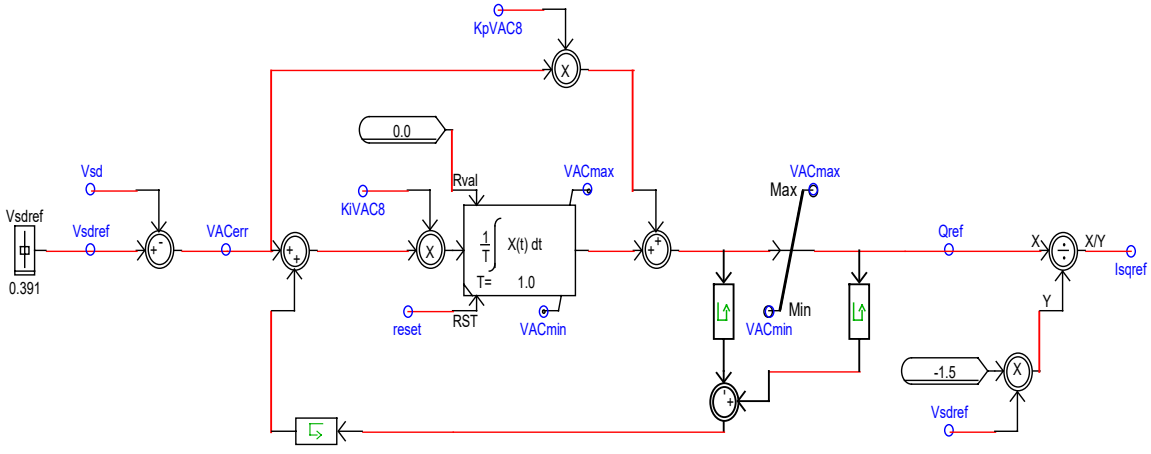

Figure 4-13. AC bus voltage regulation for q-axis current reference implemented in RSCAD.

4.7 Inner Current Control Loop

The inner current control loop has a faster time constant than outer control and designed to ensure that i_d and i_q can rapidly track their respective reference commands i_{qref} and i_{qref}. The inner current control also enhances protection of the VSC against overload and excessive current due to external faults.

For the PV system shown in Figure 4-1, the dynamics of the VSC ac-side current are described by the following space phasor equation:

$$L\frac{di}{dt} = -Ri + V_t - V_s \tag{4-17}$$

Substituting for V_t from Equation (4-1) in Equation (4-17),

$$L\frac{di}{dt} = -Ri + \frac{V_{DC}}{2}m - V_s \tag{4-18}$$

The dq-frame equivalents to Equation (4-18) are,

$$L\frac{di_d}{dt} = -Ri_d + L\omega i_q + \frac{V_{DC}}{2}m_d - V_{sd} \tag{4-19}$$

$$L\frac{di_q}{dt} = -Ri_q + L\omega i_d + \frac{V_{DC}}{2}m_q - V_{sq} \tag{4-20}$$

Where ω is the frequency of the reference frame. In Equation (4-19) and (4-20) i_d and i_q are the state variables and the outputs, m_d and $m_q$are the control inputs, and V_{sd} and V_{sq} are the disturbance inputs [23]. Due to the factor $L\omega$, the dynamics of i_d and i_q are coupled and nonlinear. To decouple and linearize the dynamics of i_d and i_q, m_d and m_q are determined based on the equations:

$$m_d = \frac{2}{V_{DC}}(u_d - L\omega_0 i_q + V_{sd}) \tag{4-21}$$

$$m_q = \frac{2}{V_{DC}}(u_q + L\omega_0 i_d + V_{sq}) \tag{4-22}$$

Where u_d and u_q are new control inputs, which can be obtained from PI compensator $k_d(s)$ and $k_q(s)$ respectively in Figure 4-14. The control signal u_d is the output of a compensator $k_d(s)$ processing the error signal $e_d = i_{dref} - i_d$. Similarly, u_q is the output of another compensator $k_q(s)$ that processes the error signal $e_q = i_{qref} - i_q$. The PWM modulating signals, $m_a(t)$, $m_b(t)$ and m_c(t) are generated by applying the inverse Park's transformation to m_d and m_q. The gating pulses for the VSC valves that could be generated by a switching model for the converters is applied. The implementation for inner current control in RSCAD is illustrated in Figure 4-15.

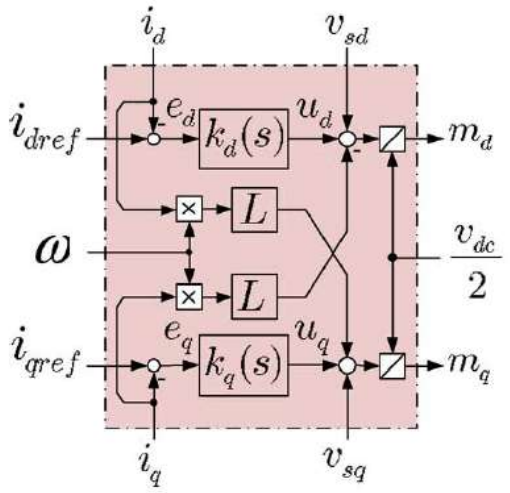

Figure 4-14. Inner current control diagram in dq-frame [23].

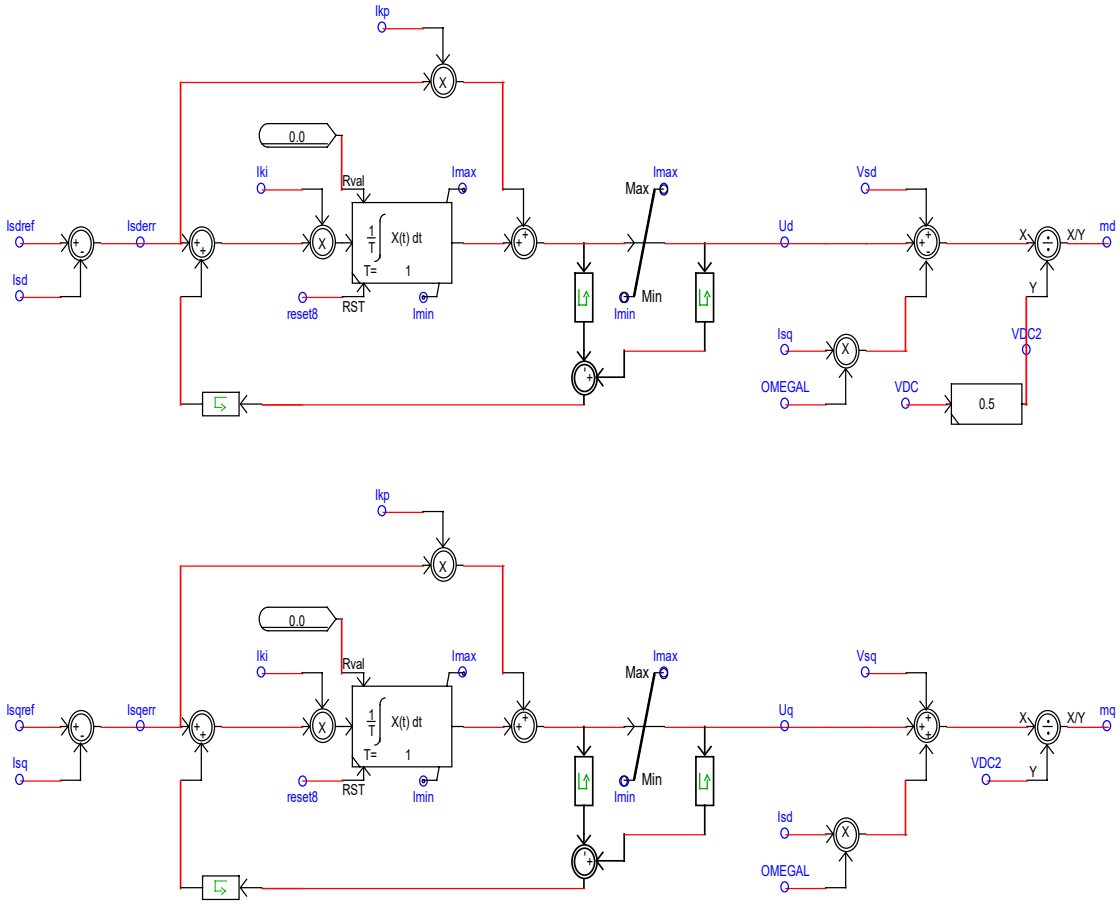

Figure 4-15. Inner current control implemented in RSCAD.

4.8 AC Grid model

The connection to AC grid is modelled with three winding step up transformer, transmission line and voltage source behind a Thevenin equivalent impedance as shown in Figure 4-16. This grid side model is a general one used throughout the research, while the transformer MVA rating and the voltage of winding 1 of the transformer and the length of the transmission line will vary for the different systems.

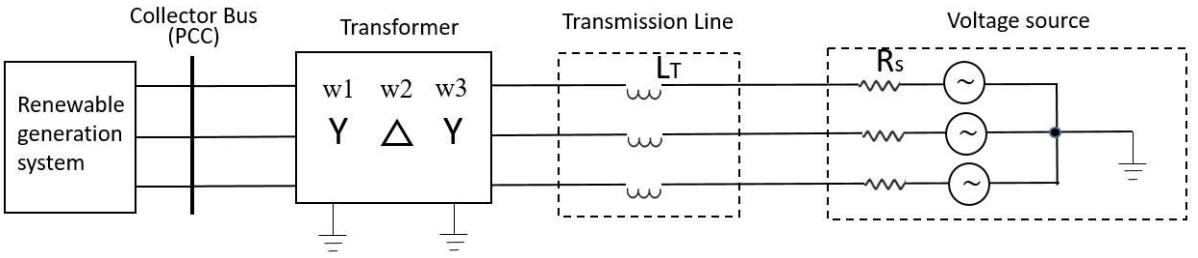

Figure 4-16. Grid model.

4.8.1 Three Winding Transformer Model

Three winding transformers are widely used for interconnecting generation sources to transmission lines. The delta connected tertiary winding can balance the zero sequence component of unbalanced loading and also greatly reduce the zero sequence impedance of transformer with Yg-Delta-Yg connection. The three winding transformer parameters used for PV system are listed in Table 4-2.

Table 4-2. Three winding transformer parameters for PV system.

MVA rating	25 MVA
Frequency	60 Hz
Primary winding 1 voltage (Wye)	13.2 kV
Secondary winding 2 voltage (Delta)	0.6 kV
Tertiary winding 3 voltage (Wye)	230 kV
Leakage reactance	0.01 pu
No load losses	0.001 pu

4.8.2 Transmission Line Model

Transmission lines are modelled using travelling wave algorithms within the RTDS in this research. The RSCAD software module known as T−LINE was used to generate the required transmission line model data from physical line configuration data. In this research the Bergeron line model is chosen. This line model represents the line's characteristic impedance and travel time at only a single frequency when forming a travelling wave model of the line. Table 4-3 lists the transmission line model parameters.

Table 4-3. 230 kV transmission line model parameters.

Line Data			
Model	Bergeron		
Line length	50 km		
Ground resistivity	100 Ω-m		
Rated frequency	60 Hz		
Tower Data			
Number of Conductors on Tower	3		
Number of Circuits on Tower	1		
Number of Ground Wires on Tower	2		
Conductor Data			
Transposition	Transposed		
Conductor Name	Chukar		
Sub-Conductor Radius	2.03454 cm		
DC Resistance per Sub-Conductor	0.03206 Ω/km		
Shunt Conductance	1.0e-11 mho/m		
Number of Sub-Conductors per Bundle	2		
Bundle Configuration	Symmetrical		
Sub-Conductor Spacing	45.72 cm		
Conductor Bundle	Bundle #1	Bundle #2	Bundle #3
Horizontal Distance (x)	-10.0 m	0.0m	10.0m
Conductor Height at Tower (y)	30.0 m	30.0 m	30.0 m
Sag at Mid-Span	10.0 m		
Ground Wires Data			
Ground Wire Name	7/16 Steel		
Ground Wire Radius	0.55245 cm		
DC Resistance per Wire	2.8645 Ω/km		
Ground Wire Number	Ground wire #1	Ground wire #2	
Horizontal Distance (x)	-5.0 m	5.0 m	
Height at Tower (y)	35.0 m	35.0 m	
Sag at Mid-Span	10.0 m		

Figure 4-17 and Figure 4-18 illustrate the physical structure of the transmission line tower generated in RSCAD T-LINE module. Figure 4-19 shows the conductor bundle components for the transmission line model.

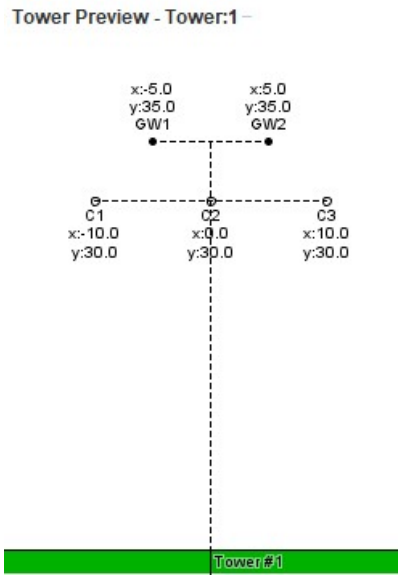

Figure 4-17. Tower preview with measurements (m).

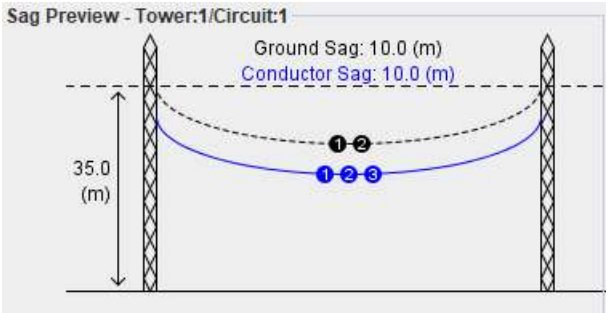

Figure 4-18. Conductor sag for line model.

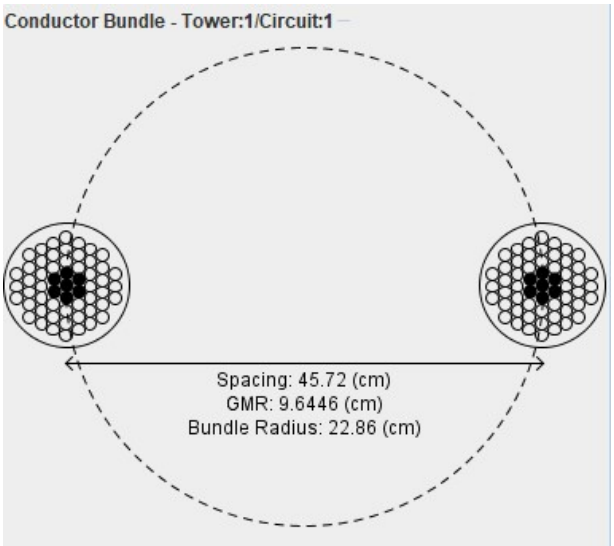

Figure 4-19. Conductor bundle in Tower 1.

4.8.3 Thevenin Equivalent Voltage Source Model

A voltage behind a Thevenin equivalent reactance is used to represent the rest of the ac system. In RSCAD if there is at least one ideal AC source model anywhere in the user's power system circuit, all generators connected to that circuit will operate at the source's specified power system frequency in steady-state. For this reason, the system using a single AC source model does not need frequency droop control to maintain its electrical frequency within a safe range. In this research a voltage source of 230kV 60Hz and the Thevenin impedance of 0.1 ohm is used in the AC grid model for the simulation.

4.9 Summary

Chapter 4 describes PV generation model in RSCAD, including the averaged voltage source converter model and control schemes. A general AC grid model with three-winding transformer is also introduced in this chapter.

Chapter 5 Modeling of Type 3 WTG

5.1 RTDS Implementation of Type 3 WTG Model

A Type 3 WTG is a doubly fed induction machine with its stator windings directly connected to the grid and its rotor windings connected to the grid through a back to back converter. As described in Chapter 3, the converter includes a rotor side converter (AC/DC) and a grid side converter (DC/AC). The topology of the converter is similar to that of PV system discussed in Chapter 4. The control schemes with dq-frame are also used in Type 3 WTG model, however the frequency in the rotor side AC/DC converter is the desired slip frequency for the induction machine state instead of the AC system frequency in the grid side DC/AC converter. The use of the converters in Type 3 WTG allows bidirectional power flow in the rotor circuit to increase the wind speed range of the generator. This chapter focuses on the RTDS implementation of Type 3 WTG, and a description of the detailed control scheme can be referred to [24].

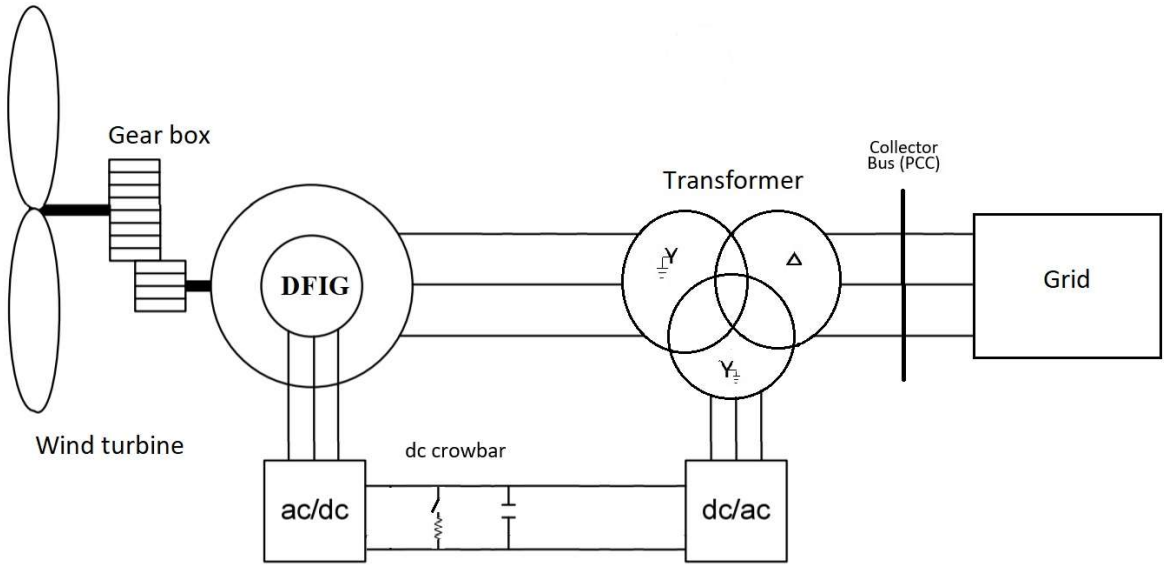

Figure 5-1. The schematic diagram of Type 3 WTG with dc crowbar.

A Type 3 WTG model with a dc crowbar is illustrated in Figure 5-1, and the RTDS implementation is shown in Figure 5-2.

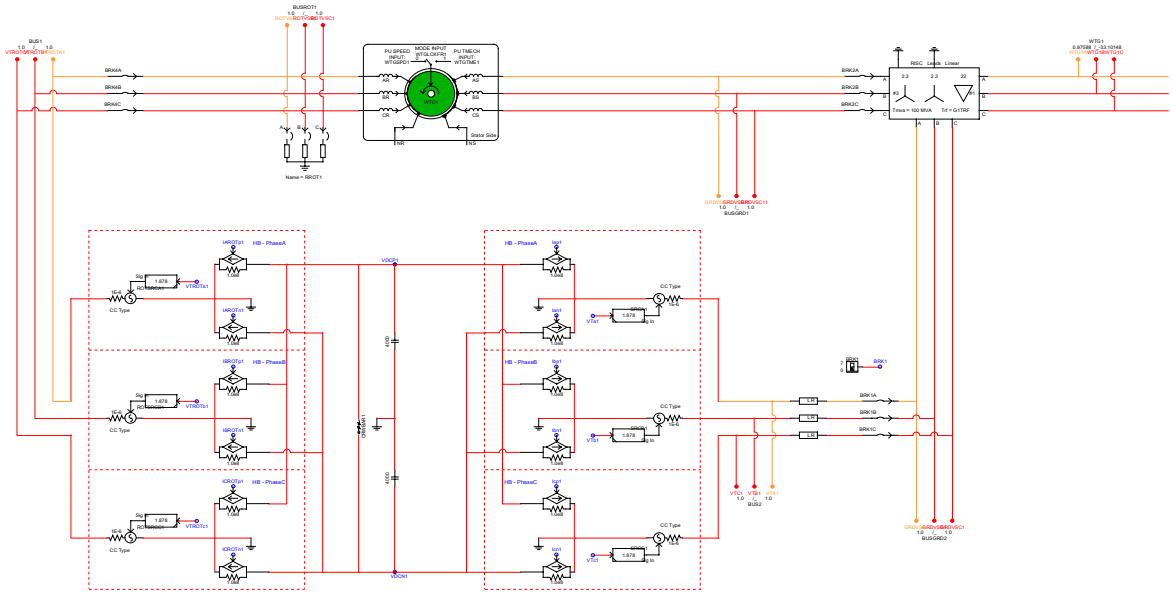

Figure 5-2. RTDS implementation of Type 3 WTG

Figure 5-3 shows the RTDS doubly fed induction machine model. The mechanical speed of the machine can be made to either respond directly to a speed order, or the speed can be made to vary according to the applied mechanical torque. As indicated on the machine icon, when the Lock/Free mode switch input is set to 1 (Lock mode), the machine will respond to applied torque. On the other hand, when the Lock/Free switch input is set to 0 (Free mode), the machine will respond to a speed input. The reference direction for applied torque is in the direction of positive rotation. Therefore, a positive applied torque will cause the induction machine to generate electrical power into the power system as an induction generator. The parameters of the induction machine are listed in Table 5-1.

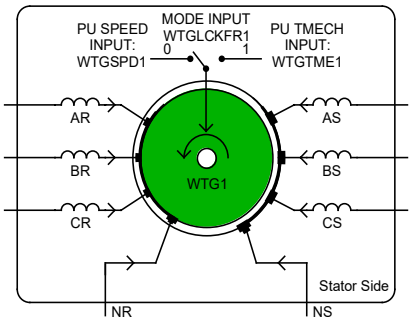

Figure 5-3. RTDS induction machine model.

Table 5-1. Parameters of the wound rotor in the Type 3 WTG.

Rated voltage (L-L RMS)	2.3 kV
MVA rating	1.678 MVA
Rated frequency	60 Hz
Rated current	596 A
Stator Resistance	29 mΩ (0.0092 pu)
Stator Inductance	34.12 mH (0.072 pu)
Rotor Resistance	26 mΩ (0.00825 pu)
Rotor Inductance	34.12 mH (0.072 pu)

The three-winding transformer used in the Type 3 WTG model steps up the power produced at the WTG terminals 2.3 kV line-to-line (L-L) voltage to 22 kV L-L for the collector feeder. Its parameters are given in Table 5-2.

Table 5-2. Three winding transformer parameters in the Type 3 WTG.

MVA rating	100 MVA
Frequency	60 Hz
Primary winding 1 voltage (Delta)	22 kV
Secondary winding 2 voltage (Wye)	2.3 kV
Tertiary winding 3 voltage (Wye)	2.3 kV
Leakage reactance	0.01 pu
No load losses	0.001 pu

The crowbar circuit is implemented by a resistor on the DC link as shown in Figure 5-4, which is controlled by a built-in switch in the RTDS resistor component. The DC link is

grounded in the midpoint of two capacitors to provide a ground reference to the Type 3 WTG. The DC link parameters is given in Table 5-3. The switch control logic of the crowbar is that, when the DC link voltage is greater than 1.05 times the rated dc voltage, 4.2 kV, the crowbar circuit will be activated, and the theoretical power dissipated by the crowbar resistor at the voltage of 4.2 kV will be 0.0176 MW which is calculated from Equation (5-1).

$$P_{diss} = \frac{V_{DC}^2}{R} = \frac{(4.2\ kV)^2}{1\ k\Omega} = 0.0176\ MW \tag{5-1}$$

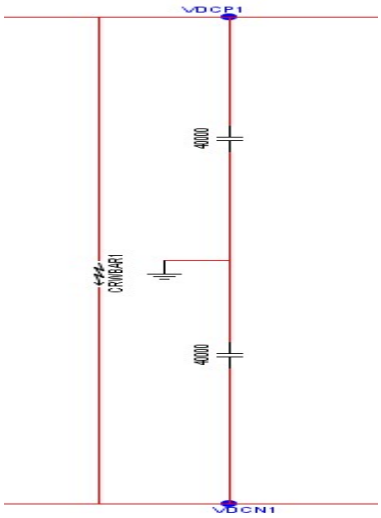

Figure 5-4. Crowbar circuit implementation in RSCAD.

Table 5-3. DC link parameters in the Type 3 WTG.

Rated DC link voltage	4.0 kV
Crowbar resistance	1000 Ω
Capacitance	4000 μF

5.2 Summary

Chapter 5 describes the RSCAD implementation of Type 3 WTG, including wound rotor machine, step up transformer and DC crowbar circuit.

Chapter 6 Integrated PV and Type 3 WTG System

6.1 Introduction

In most cases the same type of renewable generation sources are integrated into the same collector bus. In this chapter a system with different types of renewables, PV and WTG integrated into a collector bus is proposed for the greater usage of the renewable energy. First an integrated system with one PV system designed from Chapter 4 and one Type 3 WTG from Chapter 5 is introduced. To check the performance of this system, the real power characteristic of the PV model with daily insolation and temperature variation in steady-state is modeled with simulation software.

To improve reality of the model, the integrated system is extended to include more PV models and WTGs. This expansion flexibility allows the system to integrate different amount of PV and WTG at the same collector bus according to the geographical and climate condition. In this research the extended system with two PVs and five Type 3 WTGs is considered. The simulation results during normal operation of the integrated system are presented in this chapter, and the protection scheme study will be discussed in later chapters.

6.2 Integrated system with one PV and one WTG

As shown in Figure 6-1 one PV generator and one Type 3 WTG are connected to the AC grid through transmission lines. The AC grid model is same as the one described in Section 4.8. The 5 km long transmission lines for the collector of PV and WTG are implemented with equivalent PI sections since the travel time of travelling wave for the short line section is smaller than the minimum time step of the simulation circuit [11]. Travelling wave transmission line models and PI section models are both available to represent transmission

lines on the RTDS. However, travelling wave models are generally preferred unless the desired line is very short, in which case a PI section model must be used. The PI section model is essentially a lumped RLC parameter representation. Normally as lines become shorter, the error due to the approximations resulting from using PI section modelling become less significant.

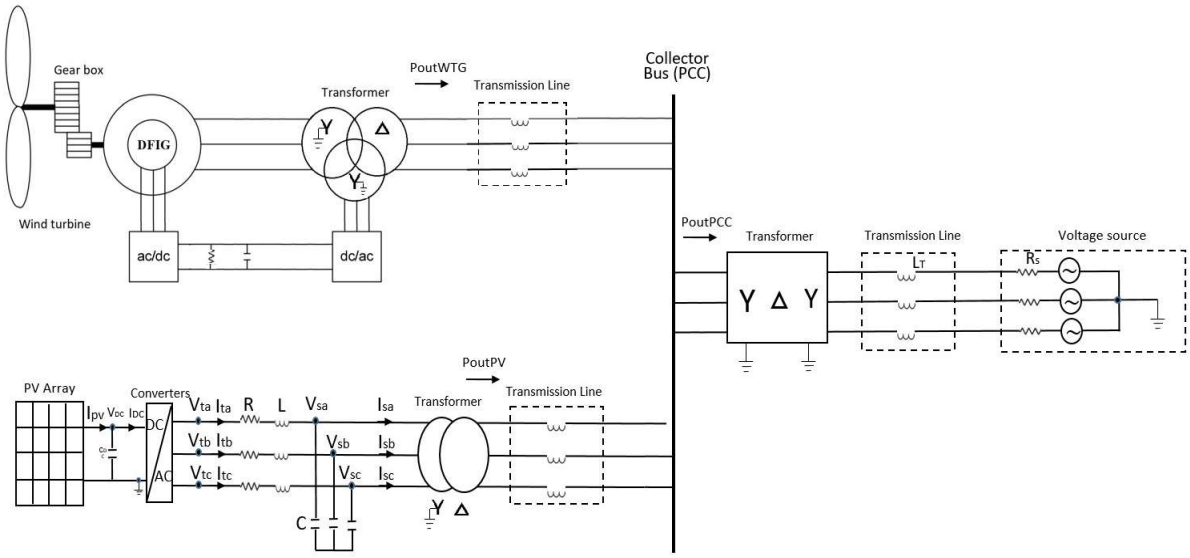

Figure 6-1. The schematic diagram of the integrated one PV and one WTG system.

6.2.1 Real Power Test in Steady-State

In order to check the performance of the integrated system, and the control of the PV model, a real power test on the integrated system in steady-state is executed. With insolation fixed at 1000 w/m^2, temperature 77° F, wind speed 10 m/s, the real powers of PV, WTG and at the collector bus (PCC) in steady-state are shown in Figure 6-2, Figure 6-3 and Figure 6-4 respectively. The real power output for PV is 1.77 MW, for WTG is 1.67 MW and at the PCC is 3.42 MW.

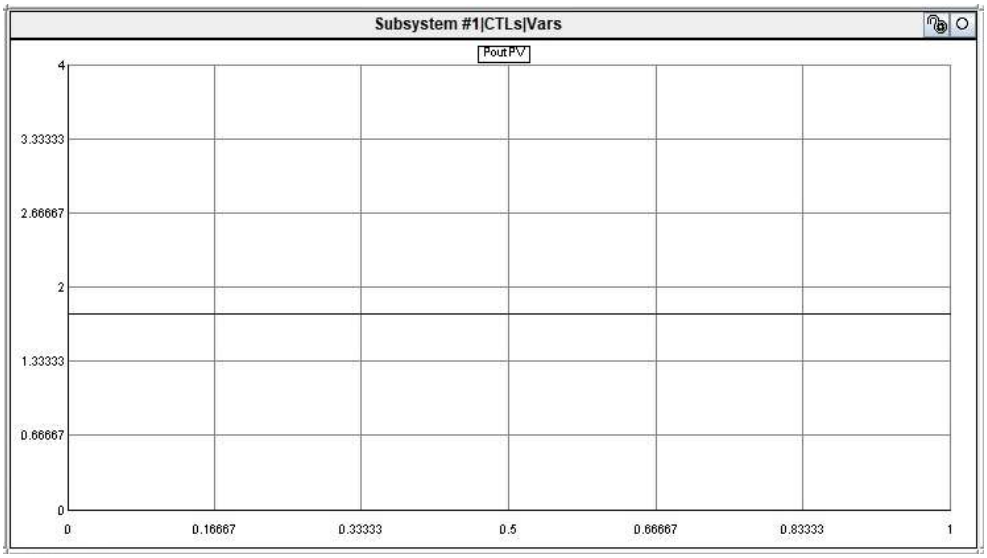

Figure 6-2. The real power of PV in steady-state.

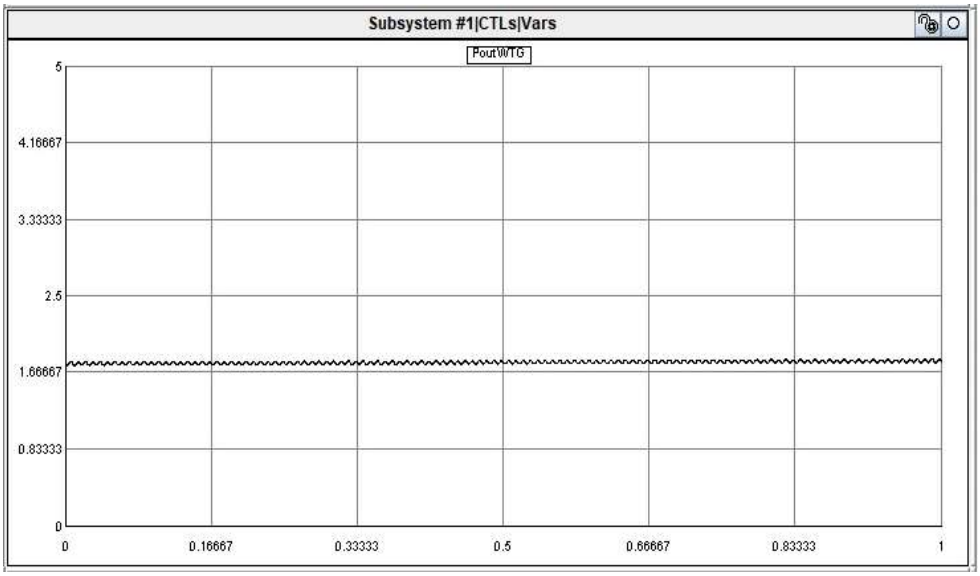

Figure 6-3. The real power of WTG in steady-state.

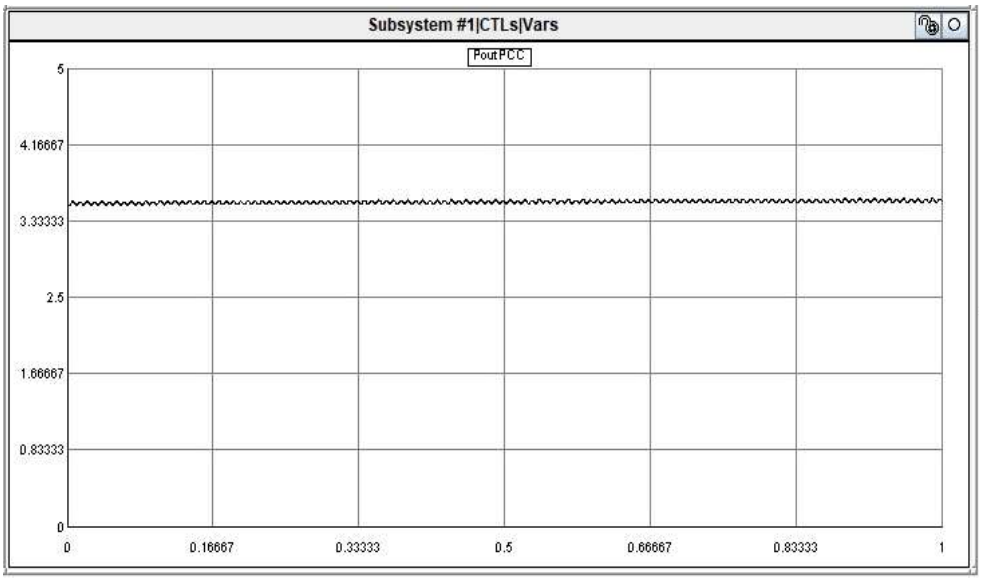

Figure 6-4. The real power at the PCC for one PV and one WTG system in steady-state.

The real power of PV is affected by the insolation and temperature. For the tested location, Moscow Idaho with coordinates: 46.73°N 117.00°W, the half-hourly insolation data from sunrise to sunset on August 18, 2010 can be obtained from National Solar Radiation Data Base [25] and is listed in Table 6-1. The half-hourly temperature data for Moscow Idaho [26] at the same day is given in Table 6-2. The insolation data can be drawn in MATLAB as shown in Figure 6-5.

Table 6-1. Insolation data on August 18, 2010 in Moscow Idaho

Time (hour)	5.0	5.5	6.0	6.5	7.0	7.5	8.0	8.5	9.0	9.5	10.0
Insolation (w/m^2)	0	30	136	280	365	460	586	680	782	860	940
Time (hour)	10.5	11.0	11.5	12.0	12.5	13.0	13.5	14.0	14.5	15.0	15.5
Insolation (w/m^2)	990	1049	1070	1101	1100	1093	1060	1026	1000	903	840
Time (hour)	16.0	16.5	17.0	17.5	18.0	18.5	19.0	19.5	20.0		
Insolation (w/m^2)	733	630	529	420	304	150	100	20	0		

Table 6-2. Temperature data on August 18, 2010 in Moscow Idaho

Time (hour)	5.0	5.5	6.0	6.5	7.0	7.5	8.0	8.5	9.0	9.5	10.0
Temperature (F)	45	48	49	50	56	57	58	60	62	64	66
Time (hour)	10.5	11.0	11.5	12.0	12.5	13.0	13.5	14.0	14.5	15.0	15.5
Temperature (F)	70	72	76	80	84	86	87	89	90	90	90
Time (hour)	16.0	16.5	17.0	17.5	18.0	18.5	19.0	19.5	20.0		
Temperature (F)	89	88	87	87	86	86	84	80	70		

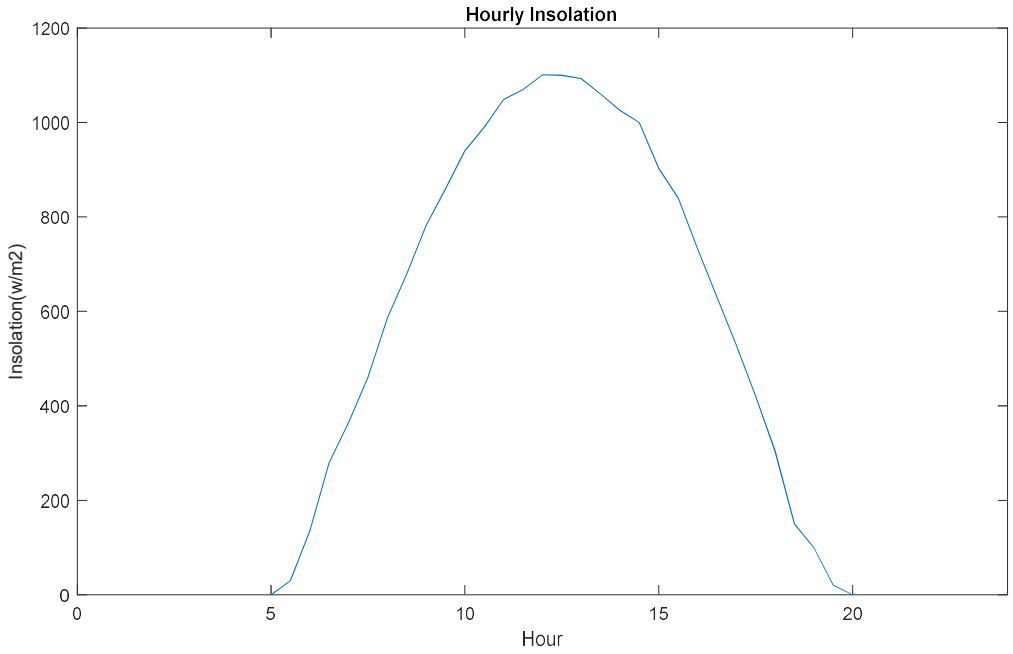

Figure 6-5. Insolation on August 18, 2010 in Moscow Idaho.

The RTDS simulator provides users with real time simulation results which limits the analysis of results on the scale of time period. MATLAB is adopted to retrieve instantaneous data from the simulation results of RTDS and process them over a time period. For each insolation data point in Table 6-1, the real power of PV model can be obtained in RTDS simulation and retrieved by MATLAB into a pre-defined array. After RTDS completes the simulation for all 33 insolation data in Table 6-1, MATLAB will get the associated 33 real

power outputs of PV model written in the array and draw the graph shown in Figure 6-6. The trend of the graph is similar with that in Figure 6-5. Adding the variable temperature data from Table 6-2 in the simulation, the real power curve of PV model output shown in Figure 6-7 is more comparable with the insolation graph shown in Figure 6-5. These simulation results prove that the dominant factor to affect the real power production of PV model is insolation level.

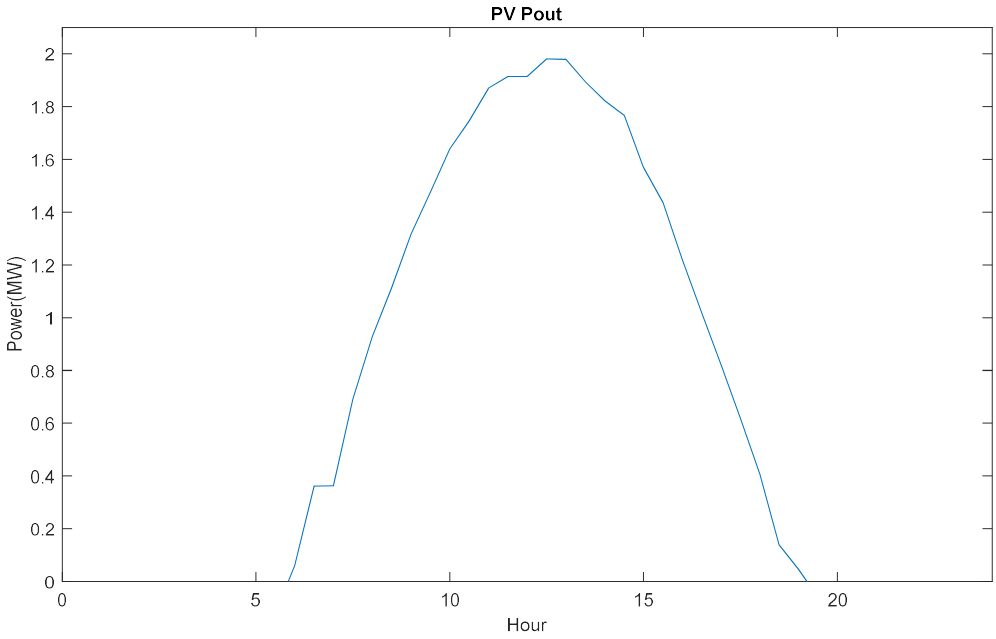

Figure 6-6. The real power of PV system with daily insolation data.

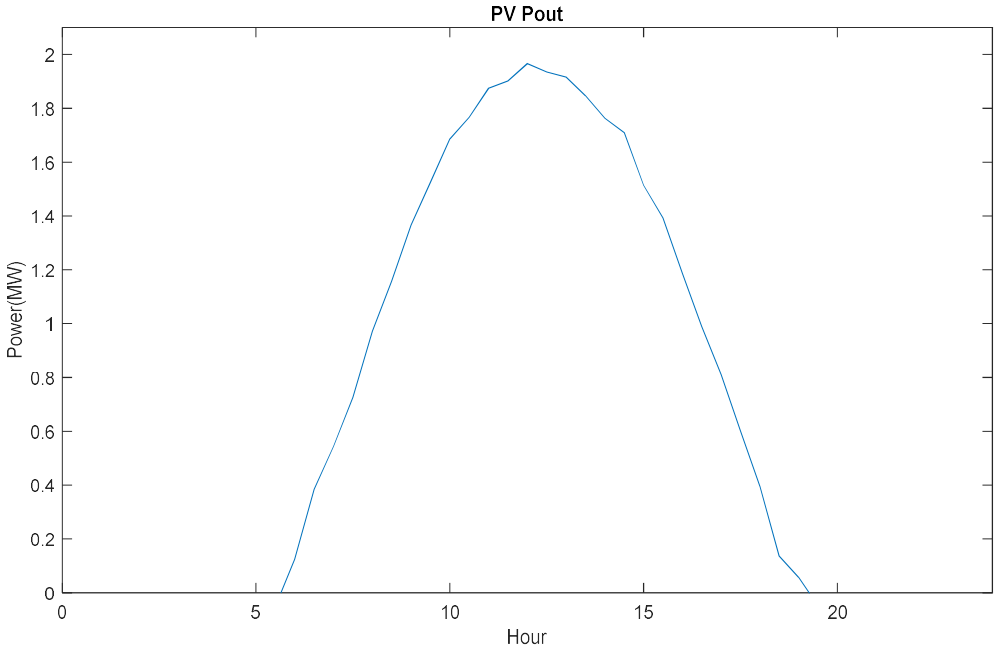

Figure 6-7. The real power of PV system with daily insolation and temperature data.

6.3 Integrated System with two PVs and five WTGs

In the real world PV plants are installed with tens or hundreds of PV arrays each on the order of 1-2 MW, and wind farms with many WTGs each with ratings of 2-10 MW. For simulating the realistic configuration, the integrated system with one PV and one WTG mentioned in the previous section is extended to include more PV and WTG renewable generators. Considering the different geographical and climate condition, the system integrating two PVs and five Type 3 WTGs is discussed for the renewable resource rich area with wind energy potentially greater than solar energy. The simplified system one-line diagram is illustrated in Figure 6-8.

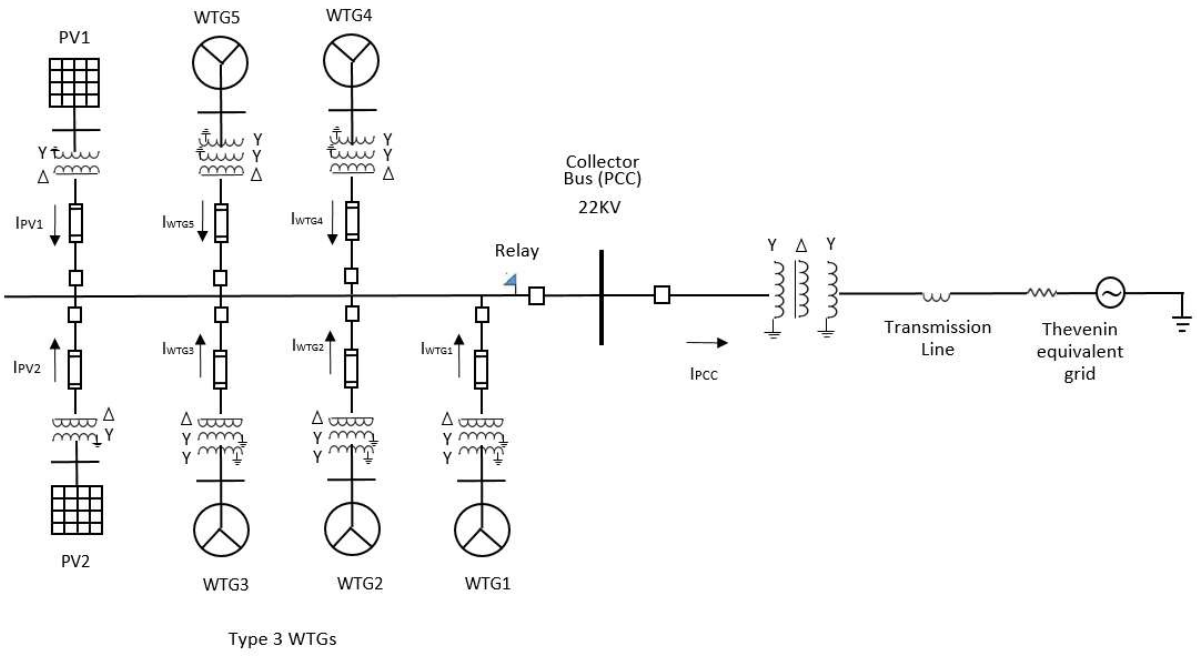

Figure 6-8. Simplified one-line diagram of the system integrating two PVs and five WTGs.

Due to the limited number of nodes that can be modeled in the simulation circuit, two RTDS racks are required for the implementation of the integrated two PVs and five WTGs system, and each rack is associated with one subsystem. A subsystem is defined as a portion of a power system model which is mathematically isolated from other portions of the system, and is usually linked only by travelling wave transmission lines to other subsystems [11]. Figure 6-9 shows the subsystem 1 circuit simulated by the hardware on rack1, and Figure 6-10 for the subsystem 2 on rack2.

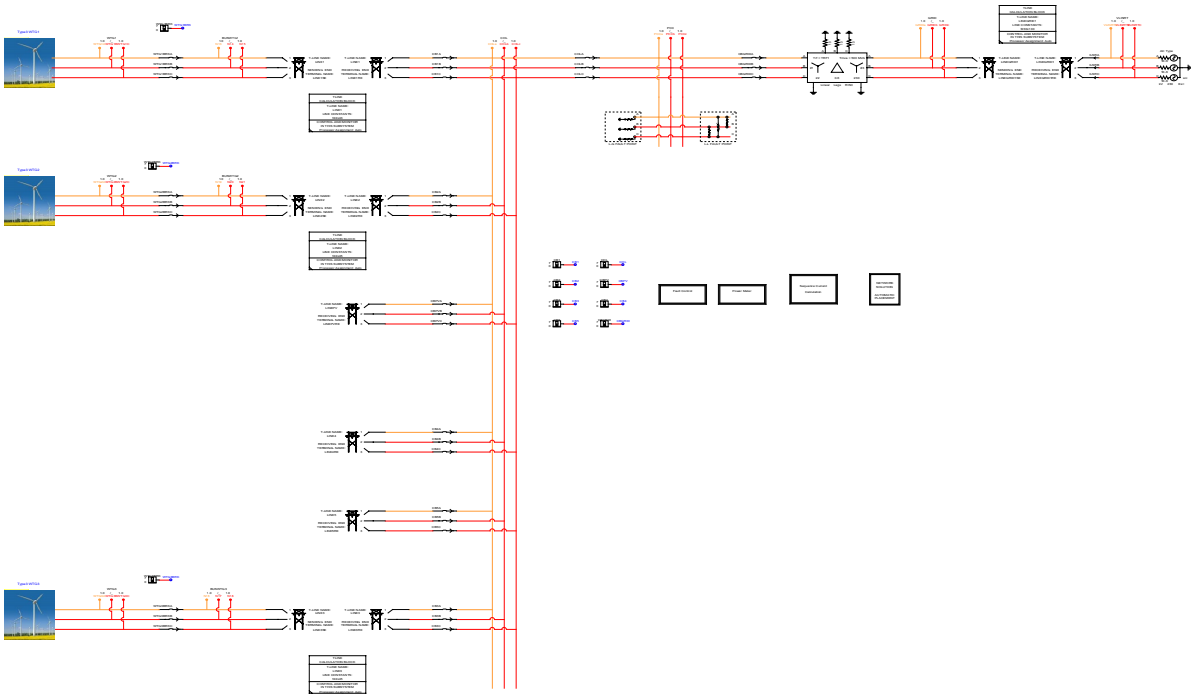

Figure 6-9. The RSCAD implementation of subsystem 1 on rack1.

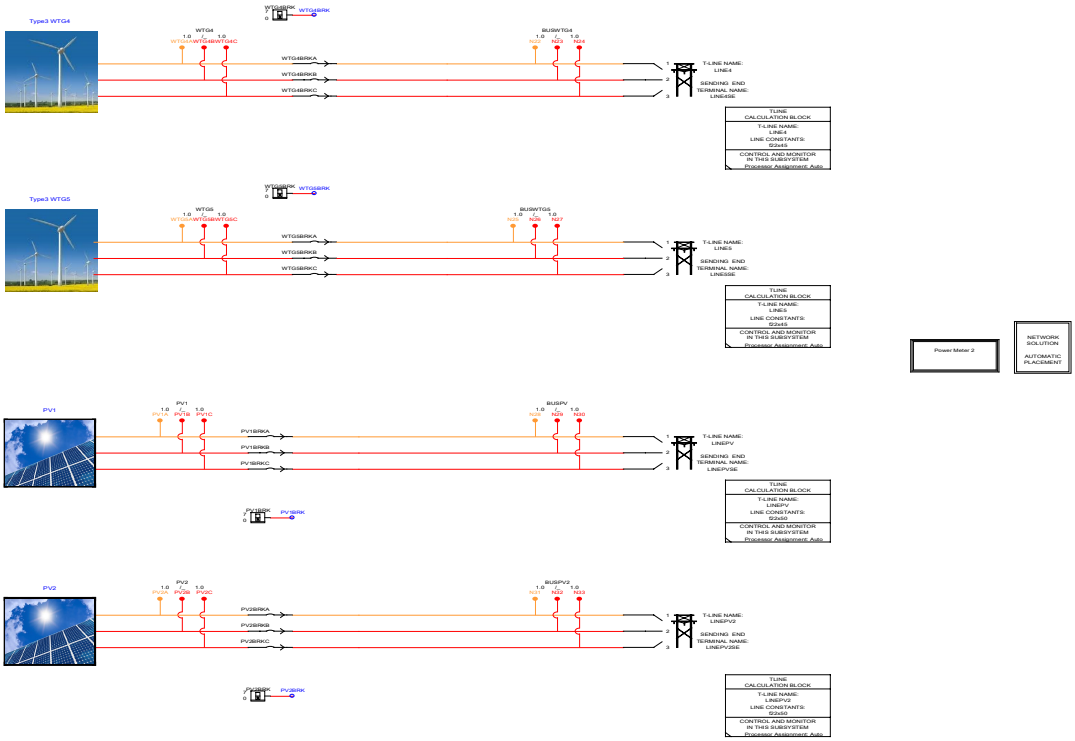

Figure 6-10. The RSCAD implementation of subsystem 2 on rack2.

The parameters of transmission line used for the 22 kV collector is listed in Table 6-3, and the length of collector lines for each PV or WTG generation is listed in Table 6-4. The differences of transmission line length among WTGs and PVs can remove the oscillation caused by reinforcement the travelling waves. Since the travel time of travelling wave for any transmission line must be greater than or equal to the minimum time step of the simulation circuit, the line lengths listed in Table 6-4 cannot be reduced to a realistic value, like 0.5 km. Due to the long collector line, the power ratings of PV and WTG generation have to be increased to make the integrated system to run normally. The power rating of PV is increased to 5 MVA, and WTG to 10 MVA. Besides the power rating, the DC link capacitors of Type 3 WTG model have bigger capacitance, 40000 μF, but other parameters in the PV model and the WTG model keep same. The parameters of the three-winding transformer in the collector substation are described in Table 6-5.

Table 6-3. Parameters of 22 kV collector line.

Line Data			
Model	Bergeron		
Ground resistivity	100 Ω-m		
Rated frequency	60 Hz		
Tower Data			
Number of Conductors on Tower	3		
Number of Circuits on Tower	1		
Number of Ground Wires on Tower	1		
Conductor Data			
Transposition	Transposed		
Conductor Name	336400 ACSR		
Sub-Conductor Radius	0.864 cm		
DC Resistance per Sub-Conductor	0.19 Ω/km		
Shunt Conductance	1.0e-11 mho/m		
Number of Sub-Conductors per Bundle	2		
Bundle Configuration	Symmetrical		
Sub-Conductor Spacing	15.72 cm		
Conductor Bundle	Bundle #1	Bundle #2	Bundle #3
Horizontal Distance (x)	0.0 m	0.762 m	1.372 m
Conductor Height at Tower (y)	8.839 m	8.839 m	8.839 m
Sag at Mid-Span	0.8 m		
Ground Wires Data			
Ground Wire Name	4/0 6/1 ACSR		
Ground Wire Radius	0.715 cm		
DC Resistance per Wire	0.368 Ω/km		
Horizontal Distance (x)	1.219 m		
Height at Tower (y)	7.62 m		
Sag at Mid-Span	0.8 m		

Table 6-4. The collector line length used in the system with two PVs and five WTGs.

Model	Transmission line length(km)
AC grid	100
PVs	50
WTG1	43
WTG2	45
WTG3	45
WTG4	45
WTG5	45

Table 6-5. Three-winding parameters for collector station transformer in two PVs and five WTGs system.

MVA rating	500 MVA
Frequency	60 Hz
Leakage reactance	0.01 pu
Primary winding 1 voltage (Wye)	22 kV
Secondary winding 2 voltage (Delta)	0.6 kV
Tertiary winding 3 voltage (Wye)	230 kV

6.3.1 Simulation Results in Normal Operation

The three-phase current in steady-state for PV1, WTG1 and at the PCC are shown in Figure 6-11, Figure 6-12 and Figure 6-13 respectively. The simulation is executed with five WTGs in the same wind condition (the torque 1 pu) and two PVs with same insolation (1000 w/m^2) and temperature (77 °F) level. The RMS current value of PV1 is 130 A at 22 kV, 260 A for WTG1 at 22 kV and 1.49 kA at the collector station on the 22 kV side of the transformer. The current profiles of WTG2/3/4/5 are same as that of WTG1, and the current of PV2 is same as that of PV1. The three-phase voltage in steady-state at the collector 22 kV bus is shown in Figure 6-14, and the RMS value is 12.5 kV. The power meters for each PV and WTG generation, and at the collector 22 kV bus are shown in Figure 6-15. These results match the expected values from theoretical calculations.

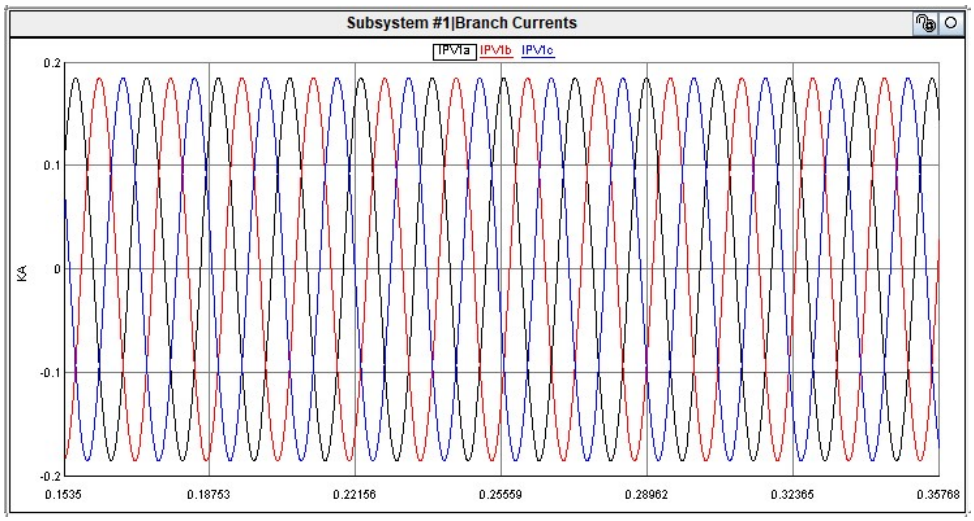

Figure 6-11. Three-phase current of PV1 in steady-state.

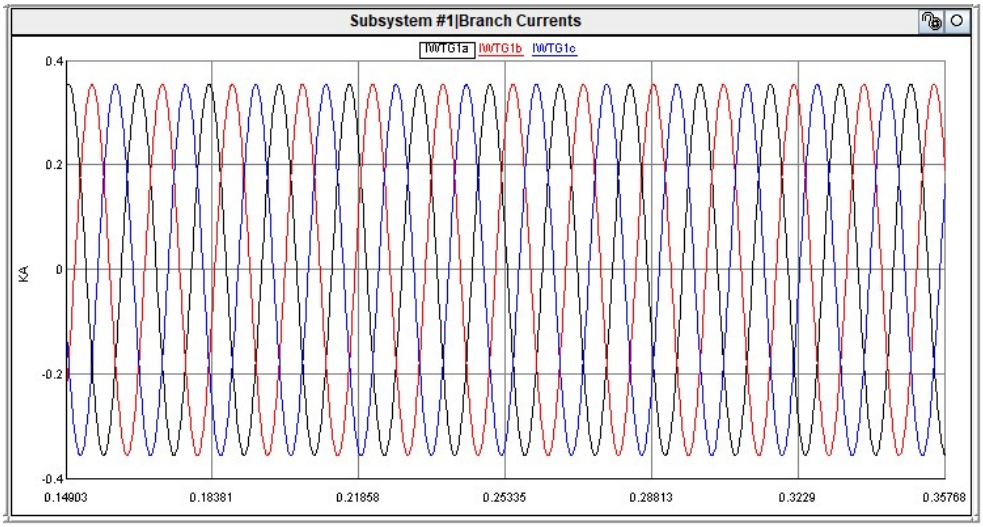

Figure 6-12. Three-phase current of WTG1 in steady-state.

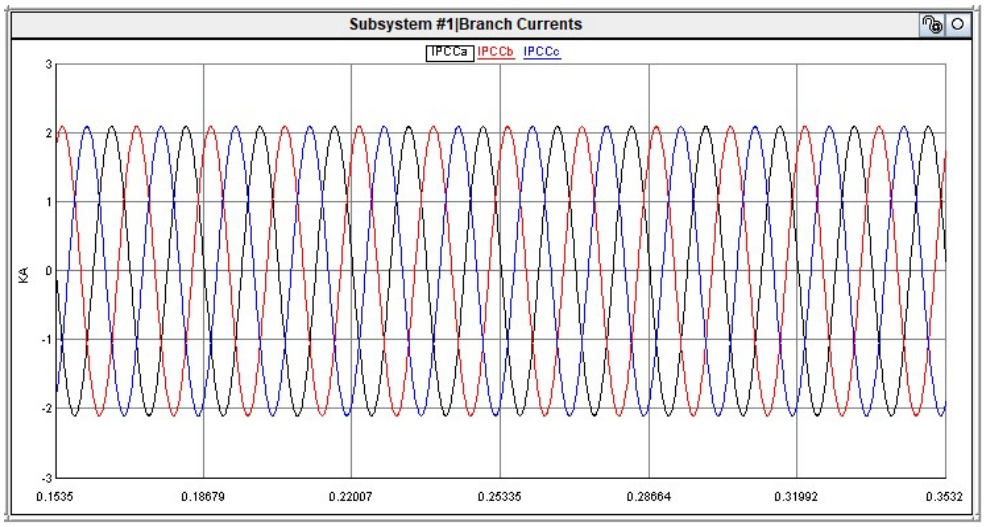

Figure 6-13. Three-phase current at the collector bus in steady-state.

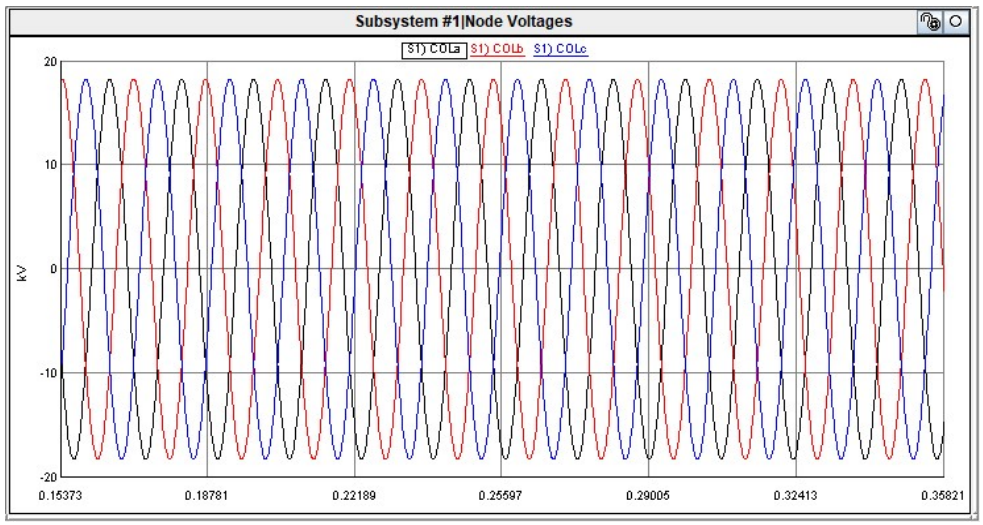

Figure 6-14. Line to ground voltage at the collector bus in steady-state.

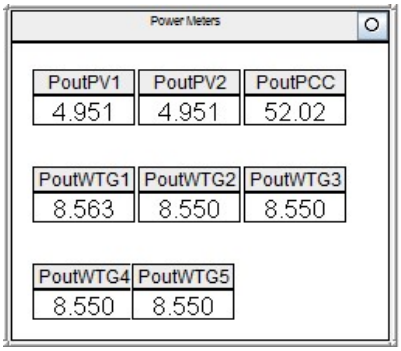

Figure 6-15. Power meters in steady-state.

6.4 Summary

In this chapter an integrated system with one PV model from Chapter 4 and one Type 3 WTG from Chapter 5 is implemented. MATLAB is used to retrieve instantaneous data from the RTDS simulation and process them in order to obtain the real power characteristic of PV model with daily insolation and temperature variation in steady-state and compare it with expected performance to validate the model. The system is expanded to integrate two PVs and five Type 3 WTGs with 22 kV collector lines, and the normal operation of the system is tested.

Chapter 7 Review of Available Protection Schemes

7.1 Introduction

Protection schemes are necessary for the power system when a fault occurs. The objective of a protection scheme is to keep the power system stable by isolating only the components under fault and leave as much of the network as possible still in operation. Protective relays are devices designed to trip a circuit breaker when a fault is detected, and are used widely throughout the power system for components from ongoing generators to distribution systems. Nowadays, microprocessor-based digital relays have largely replaced conventional electromechanical relays in all areas of power system protection. However, many of the same relaying principles of protection are still playing a dominant role to date.

During a short circuit fault high currents and voltages are measured by instrument transformers, current and voltage transformers, which step down the large values of current or voltage to small, convenient levels for the relays to deal with. These transformers also provide isolation from the high voltage system. There are various types of relay functions that can either be in stand-alone devices or with multiple functions in one device. The commonly used relays for the applications in this thesis are discussed in this chapter.

7.2 Overcurrent Relay

The overcurrent relay is defined as an element that operates or picks up only when its current exceeds a setting value. Figure 7-1 shows the logical representation of an overcurrent relay. It is used to protect power system equipment from fault currents. Since the simplest fault indicator is a sudden and generally significant increase in the current, overcurrent relays are widely used in low voltage systems.

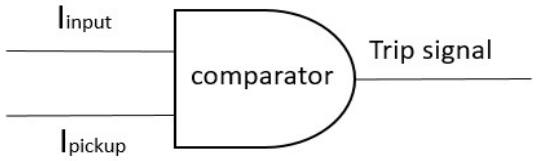

Figure 7-1. Logical representation of an overcurrent relay

The current setting of the overcurrent relay should not exceed the current carrying capacity of the conductors. Generally the over load current setting is selected at 125% of rated current based on supplied load.

7.2.1 Types of Overcurrent Relay

Depending on the time of operation the overcurrent relay is classified into the following types.

• Instantaneous Overcurrent relay

The instantaneous overcurrent relay is also called definite current relay. The relay has no intentional time delay for operation, and picks up instantaneously when the current magnitude reaches the setting value. Speed of operation is the most important feature of the relay. The instantaneous overcurrent relay ANSI/IEEE standard device number is 50.

• Definite Time Overcurrent Relay

A definite time overcurrent relay can be set to issue a trip at definite amount of time after it picks up, so it has current thresholds and definite time delays associated with thresholds. The relay will operate if the current exceeds the setting threshold for a period longer than the time delay. The relay may have multiple thresholds, each with a different delay. The highest threshold has a delay of 0, longer delays for each successive lower threshold to act as back up for downstream elements. The delays are set based on relay and circuit breaker response time

for the downstream elements. Figure 7-2 presents the tripping characteristic of definite time overcurrent relay.

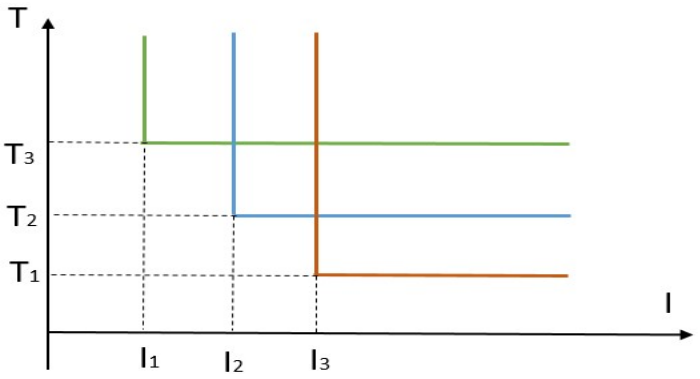

Figure 7-2. Tripping characteristic of definite time overcurrent relay.

• Inverse Time Overcurrent Relay

In this type of relays, operating time is inversely proportional to the fault current. Inverse time relays are also referred to as inverse definite minimum time (IDMT) relays and the ANSI number is 51. The relay will operate faster in the case with high fault current than that with low current in order to be able to coordinate with fuses. The time-current characteristics of the relay are fixed, and there are standard curve shapes available for inverse, very inverse and extremely inverse types [27]. Figure 7-3 illustrates the time-current characteristics of inverse overcurrent relays, and a moderately inverse curve is placed between inverse curve and very inverse curve. For time dial setting of 1 s, inverse curve has least change in time per pickup current, and extremely inverse curve has most change in time. When the multiples of pickup current is greater than 7, for the same pickup current setting, the relay with extremely inverse curve will operate faster than the relays with other curves. The relays with inverse curve are frequently used in the distribution lines in solidly grounded systems.

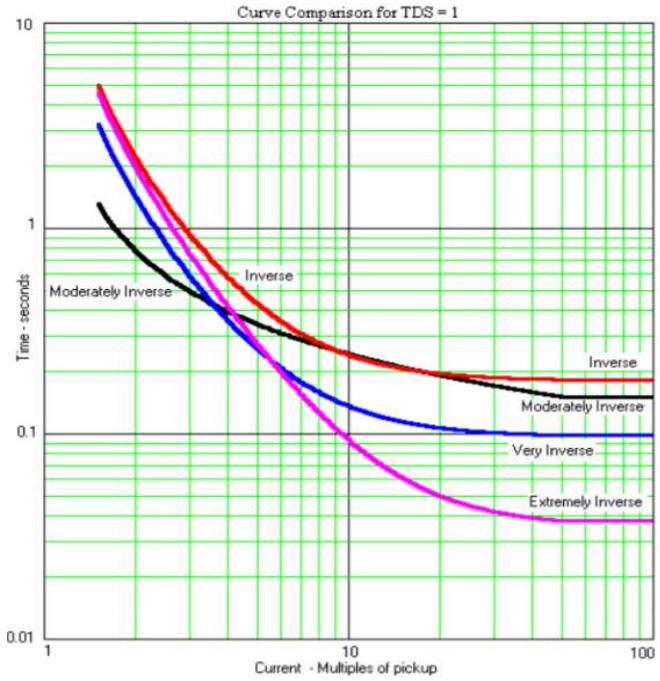

Figure 7-3. Time-current characteristics of inverse overcurrent relays.

7.3 Directional Relay

Directional relays are designed to sense the direction of current flow and determine fault direction. These elements are fundamental to the security and selectivity of protection schemes, by controlling overcurrent elements and supervising distance elements. A trip logic for the coordination of overcurrent element 50 and directional element 32 is presented in Figure 7-4.

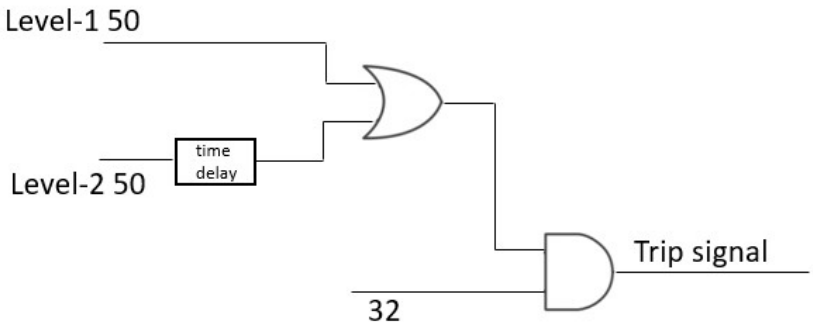

Figure 7-4. A trip logic for the coordination of overcurrent and directional elements.

Directional elements usually require a reference or polarization signal to measure the angle of the fault current and determine whether or not the relay should operate. Generally, the polarization signal is a voltage but it can also be a current quantity. In this research a directional power relay, ANSI device 32, is used for the protection scheme, since this type of relay measures real power and operates best at a high power factor. For balanced fault and unbalanced fault different methods of directional element are discussed.

• Phase directional element (32P) for balanced fault

For balanced three phase fault, the method of torque equations for voltage-polarized directional elements can be referred to [28]. In this research an alternate approach is used to compare the angle of single phase impedance calculated from measurements to thresholds. The impedance seen by the relay is calculated as per Equation (7-1).

$$Z_1 = \frac{|V_1|}{|I_1| \cdot e^{j \cdot \mathrm{PhaseI1v}}} \tag{7-1}$$

Where, Z_1 is the measured positive sequence impedance,

V_1 is the measured positive sequence voltage,

I_1 is the measured positive sequence current,

PhaseI1v is the difference between the angles of I_1 and V_1.

PhaseI1v can be given in Equation (7-2), (7-3) and (7-4).

$$\mathrm{PhaseI1v} = \arg(I_1) - \arg(V_1),\ if\ |\arg(I_1) - \arg(V_1)| < \pi \tag{7-2}$$

$$\mathrm{PhaseI1v} = \arg(I_1) - \arg(V_1) - 2\pi,\ if\ \arg(I_1) - \arg(V_1) > \pi \tag{7-3}$$

$$\mathrm{PhaseI1v} = \arg(I_1) - \arg(V_1) + 2\pi,\ if\ \arg(I_1) - \arg(V_1) < -\pi \tag{7-4}$$

Where, $\arg(V_1)$ is the measured positive sequence voltage angle,

$\arg(I_1)$ is the measured positive sequence current angle.

The criteria for declaring forward and reverse fault conditions are:

· $-90° + \angle Z_{1ang} < \arg(Z_1) < 90° + \angle Z_{1ang}$, forward fault.

· $\arg(Z_1) < -90° + \angle Z_{1ang}$, reverse fault.

Where, $\arg(Z_1)$ is the measured impedance angle,

$\angle Z_{1ang}$ is the line positive sequence impedance angle.

• Negative-sequence voltage-polarized directional element (32Q) for unbalanced faults

A negative-sequence directional element can be used to determine the directional of fault when an unbalanced fault with a sufficient amount of negative sequence current is detected. The 32Q element measures the apparent negative-sequence impedance magnitude seen by the relay and compares the result against simple thresholds to determine fault direction. The equation for 32Q element is shown in Equation (7-5).

$$Z_2 = \frac{Re[V_2 \cdot (I_2 \cdot 1\angle Z_{1an}\ )^*]}{|I_2|^2} \tag{7-5}$$

Where, Z_2 is the measured negative-sequence impedance,

V_2 is the measured negative sequence voltage in secondary volts,

I_2 is the measured negative sequence current in secondary amperes,

$\angle Z_{1ang}$ is the line positive sequence impedance angle.

The directional element 32Q compares Z_2 with two thresholds. If Z_2 is below a forward fault threshold Z2F, the element declares a forward fault. If Z_2 is above a reverse fault threshold Z2R, the element declares a reverse fault. In the application, Z2F must be less than Z2R to avoid any overlap where Z_2 satisfies both forward and reverse fault conditions. If the magnitude of the measured V_2 is so small as to give a Z_2 result near zero, simply increase the

Z2F threshold to gain directional security [28]. In this research the thresholds of negative directional element are given in Equation (7-6) and (7-7).

$$\text{Z2F} = \frac{|Z_{2L}|}{2} \tag{7-6}$$

$$\text{Z2R} = \frac{|Z_{2L}|}{2} + \varepsilon \tag{7-7}$$

Where, Z_{2L} is the line negative sequence impedance in secondary ohms.

ε is 0.1 ohm secondary.

7.4 Differential Relay

Differential relays operate on the difference of two or more electrical quantities within a protection zone. It works on the principle of comparison between the phase angle and the magnitude of the same electrical quantities, such as current and voltage. Differential relays are used for the protection of generators, transformers, transmission lines, and bus-bars etc. The ANSI number is 87. The types of commonly used differential relays are discussed as follows.

• Current Differential Relay

A relay which senses and operates the difference between the currents entering a protection zone and the currents leaving that zone. A fault within the protection zone results in a difference in current, but faults outside the zone give the same fault current at the entry and exit of the zone. Figure 7-5 and Figure 7-6 illustrates the concepts of responses of differential relays for internal and external fault respectively. The operating current flows through the relay in the internal fault case and the relay will assert an internal fault and pick up. For security of the element response, current transformers in a differential scheme must be chosen to have identical response to high overcurrent.

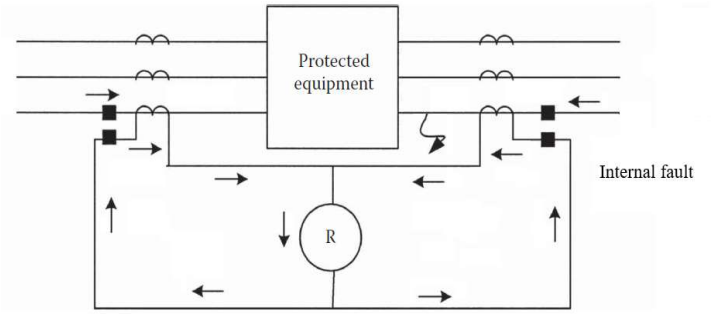

Figure 7-5. Concept of differential relay with a fault within the protection zone.

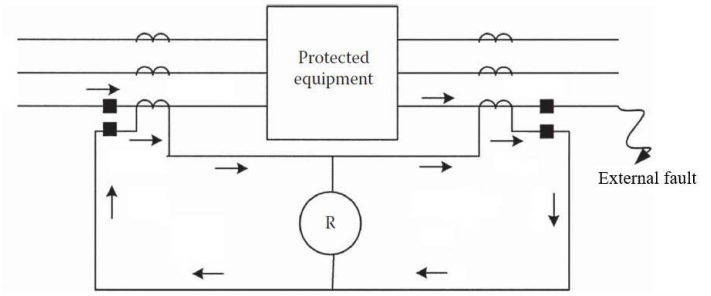

Figure 7-6. Concept of differential relay with a fault outside the protection zone.

• Percentage Differential Relay

Variants on this type of relay element are the most used form of differential relay in transformers, lines and generators. Comparing to basic current differential relay, an electromechanical percentage differential relay has additional restraining coils R_1 and R_2 connected to taps as shown in Figure 7-7. An internal fault in the protection zone will unbalance the secondary currents of current transformers, forcing an operating current I_O in the relay operating coil. During external faults I_O is too small to operate the coil. For a fixed-percentage differential relay, the operating current required is a fixed percentage of restraint current as shown in Figure 7-8, where I_{opmin} is the minimum value of operate current. The

restraint coils limit the impact of uneven saturation on the performance of the element. These schemes are also programmed in microprocessor relays.

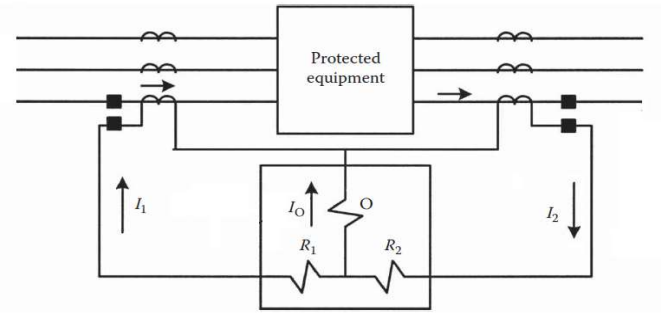

Figure 7-7. Concept of percentage differential relay.

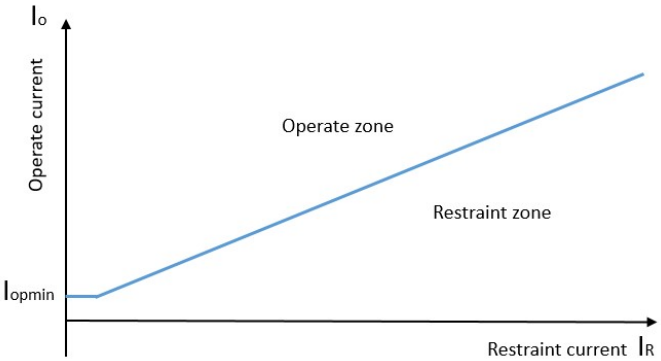

Figure 7-8. The current characteristic of fixed-percentage differential relay.

7.5 Distance Relay

Distance relay, also known as impedance relay, is governed by the effective impedance calculated by the relay based on the current and voltage measured at relay location. The relay element determines the effective impedance between the fault location and the relay location. Distance relays are extensively used for transmission line protection, and the ANSI device number is 21. In the majority of installations communication circuits are used to improve speed of performance. The relay continuously monitors the line current and voltage through the current transformer and potential transformer respectively. In the normal operation, the

effective impedance is large, and is largely resistive. When a fault happens on the protected line, the magnitude of the current rises on the faulted phase and the voltage on the phase decreases. If calculated effective impedance is less than the threshold setting, the relay will give a trip command to the circuit breaker.

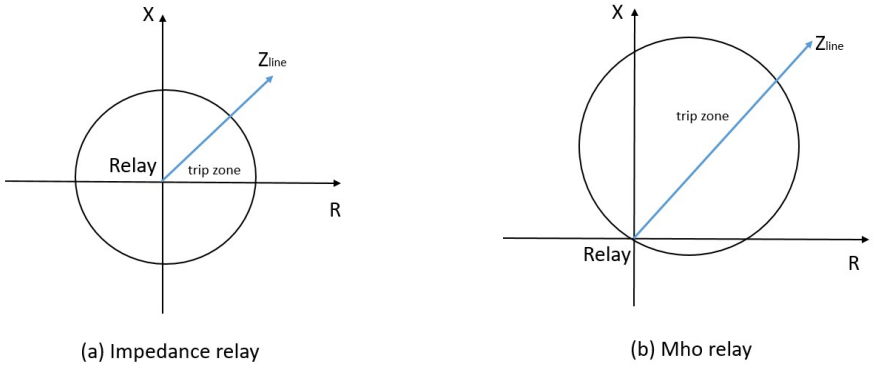

Figure 7-9. Distance relay characteristics.

The characteristic of a simple impedance element is shown in Figure 7-9 (a). The origin is the relay location. If the effective impedance seen by the relay falls within the circle, the relay operates. This sort of element has many drawbacks and is no longer used. Instead, a modified impedance relay called a mho relay is used. Figure 7-9 (b) shows an example of a mho relay. This offset adds a directional operating characteristic and widely used for line protection for phase elements. In North America, many utilities use quadrilateral elements for single line to ground faults for better fault resistance coverage.

7.6 Summary

In this chapter the commonly used protection schemes including overcurrent relay and directional relay are reviewed. Phase directional elements with single phase angle method for balanced faults and negative sequence directional elements for unbalanced faults are introduced. Differential relay and distance relay are also briefly reviewed.

Chapter 8 Simulation Results and Protection Scheme Performance

8.1 Introduction

The protection scheme performance of the integrated system with two PVs and five WTGs described in Section 6.3 is discussed in this chapter. The responses of the system to different types of faults are analyzed using symmetrical components from the simulation results, and the protection performance is also analyzed. The protection scheme is verified with the fault response when different wind speeds among WTGs.

8.2 System Configuration and Sequence Networks

Figure 8-1 shows the test integrated system with fault occurring on the 22 kV collector bus zone. An overcurrent element 50 and a directional element 32 are placed on the collector feeder marked by the blue pennant labelled Relay. The CT and PT ratios are calculated as per Equation (8-1) and (8-2).

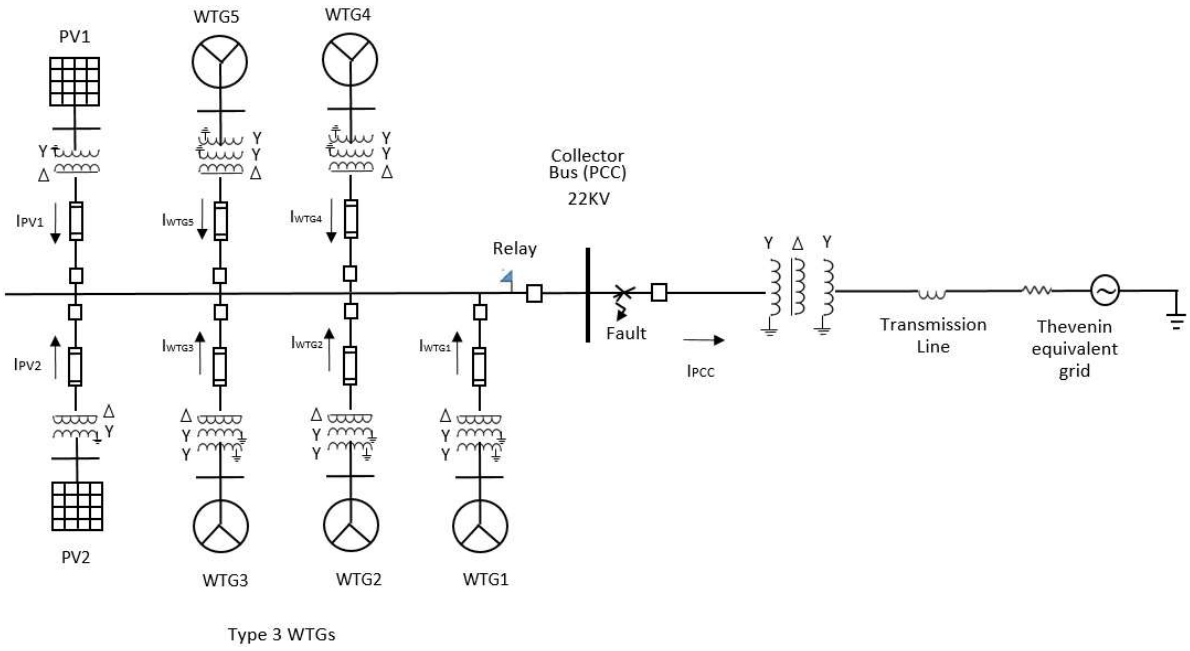

Figure 8-1. Test system with a possible fault location.

$$\text{CTR} = \frac{1500\ A}{5\ A} \tag{8-1}$$

$$\text{PTR} = \frac{22\ kV}{120\ V} \tag{8-2}$$

According to Equation (7-6) and (7-7), the thresholds of the directional element can be set to 1.9 ohm for Z2F and 2.0 ohm for Z2R based on the system impedances.

In short circuit studies a Type 3 wind power plant can be modelled as a single equivalent machine and it behaves as a current limited generator with an equivalent generator impedance for phasor analyses for faults that occur on the collector feeders. PV generators are modelled as an equivalent current source. Based on these equivalent units, the sequence networks of test system are illustrated in Figure 8-2. Z_{PV} is the equivalent impedance of the equivalent PV generator, Z_{PVT} is the equivalent step-up transformer for PVs, and Z_{PVLine} is the impedance of collector feeder between equivalent PV generation and the collector bus. Z_{WTG} is the equivalent impedance of the equivalent WTG generator, Z_{WTGT} is equivalent impedance of the equivalent step-up transformer for WTGs, and Z_{WTGLi} is the equivalent impedance of collector feeder between WTGs and the collector bus. Z_{PVLine} and $Z_{WTGLine}$ can be calculated based on the 22 kV collector line parameter listed in Table 6-3 and the line lengths listed in Table 6-4. The three-winding transformer in the substation can be represented in the positive and negative sequence networks as a single impedance Z_{ST1} and Z_{ST} where $Z_{ST} = Z_{ST1} = Z_{STL} + Z_{STH}$. However in zero sequence network shown in Figure 8-2 (c), the impedances for three windings should be represented since the transformer is connected Yg-D-Yg, and Z_{STL}, Z_{STH}, and Z_{STM} are the impedance of low voltage, high voltage and medium voltage winding respectively. Z_{Line} is the impedance of transmission line connecting collector station to the

grid, and Z_S is the Thevenin equivalent impedance of the grid. The subscript numbers 1, 2 and 0 for each impedance symbol represent the positive, negative and zero impedance respectively.

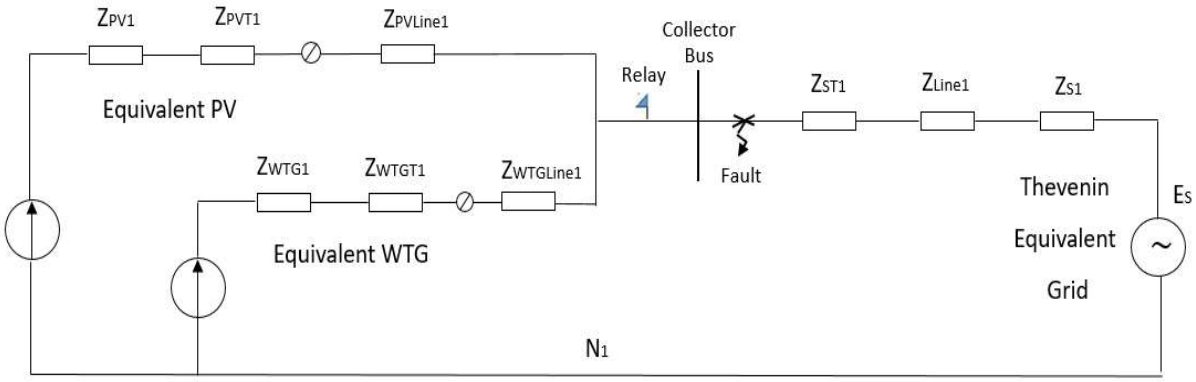

(a) Positive sequence network

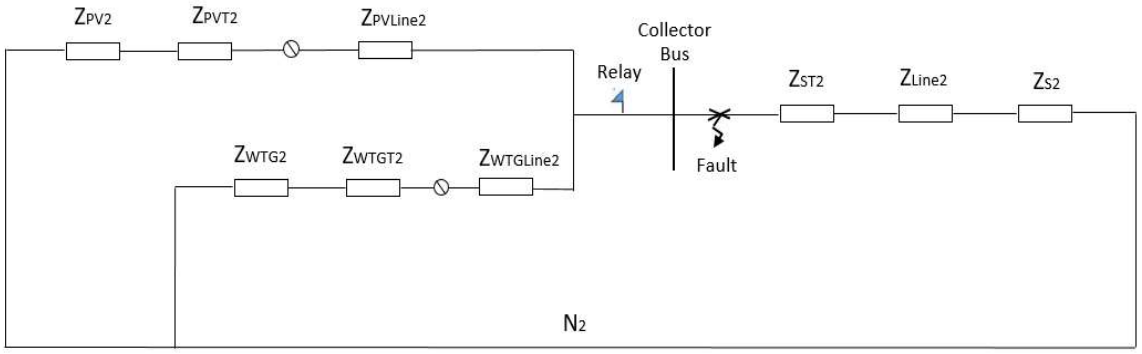

(b) Negative sequence network

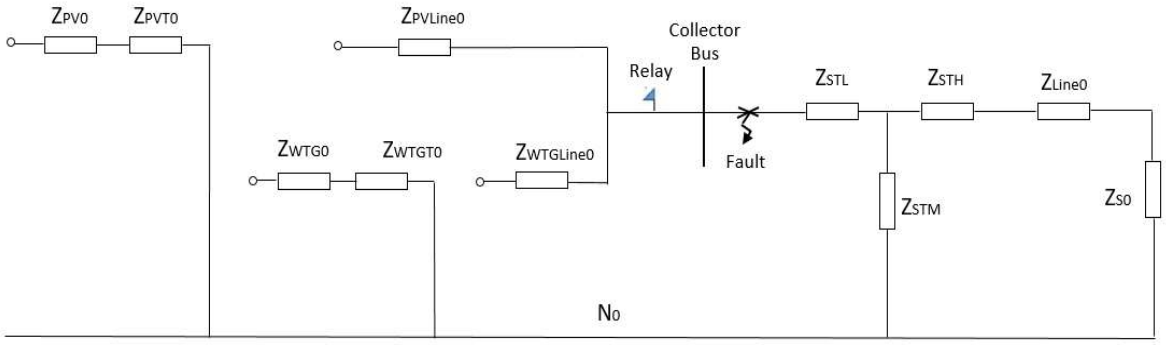

(c) Zero sequence network

Figure 8-2. Sequence networks of test system.

8.3 System Response to Faults

There are two main classes of short circuit faults in power systems, symmetrical (balanced) and unsymmetrical (unbalanced) faults. These types of faults will be simulated at the location indicated in Figure 8-1. The measured current and voltage at the relay location and the calculated negative sequence secondary impedance will be plotted and analyzed for each fault. The DC link voltage and the power dissipated by the resistor in the crowbar circuit of Type 3 WTG for each fault will also be presented and investigated.

8.3.1 Single Line to Ground (SLG) Fault

Figure 8-3 shows the phase currents at the relay location for an A-phase to ground fault, and Figure 8-4 presents the sequence current magnitudes. Figure 8-5 shows the line to ground voltages. The fault occurs at t=0.2 s and lasts for a period of 9 cycles (0.15 s). Since the transformers windings facing the collector for the PVs and WTGs are delta connected, the value of zero sequence current is contributed by renewables is zero, and the voltage response looks somewhat like a line to line fault. For the collector feeder protection, negative sequence current can be used for 50Q element picking up the fault. As expected the ground element 50G shows no response.

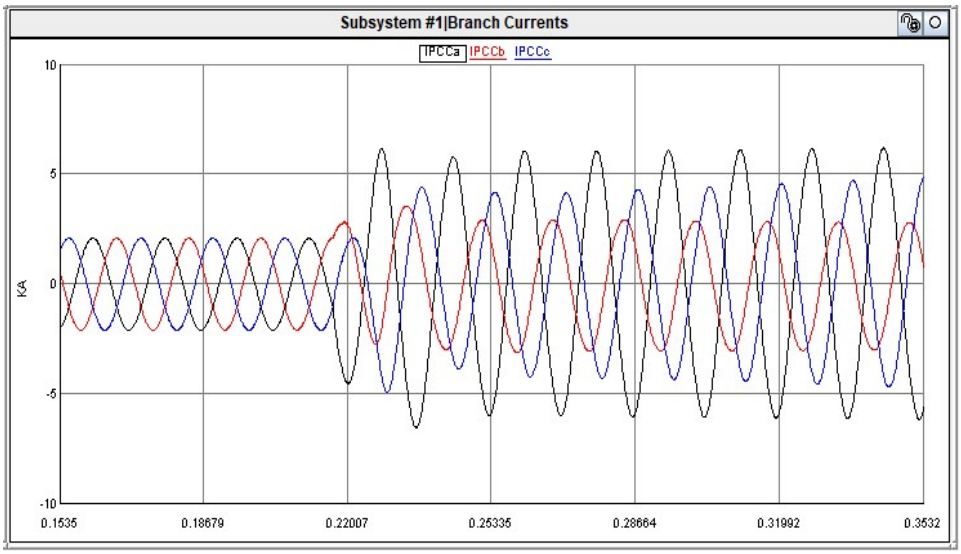

IPCCa, IPCCb, IPCCc – Current on phases A, B & C respectively
Figure is zoomed in to show onset of the fault.

Figure 8-3. Three-phase current at the relay location for SLG fault.

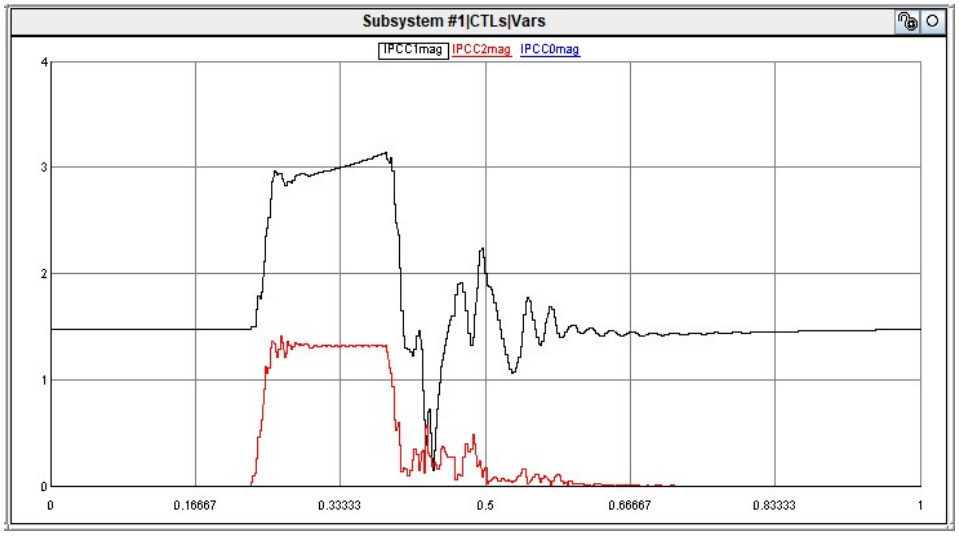

IPCC1mag – Positive sequence current magnitude
IPCC2mag – Negative sequence current magnitude
IPCC0mag – Zero sequence current magnitude

Figure 8-4. Sequence current magnitudes for SLG fault.

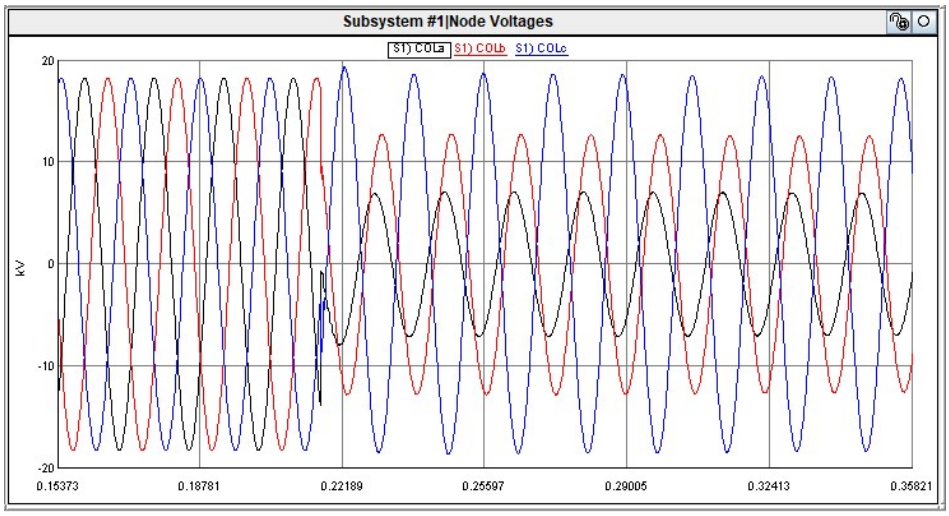

COLa, COLb, COLc – Voltage on phases A, B & C respectively
Figure is zoomed in to show onset of the fault.

Figure 8-5. Line to ground voltages at the relay location for SLG fault.

The effective negative sequence impedance for SLG fault shown in Figure 8-6 is above the reverse fault threshold, so this result can be used for negative-sequence directional element 32Q to declare a reverse fault.

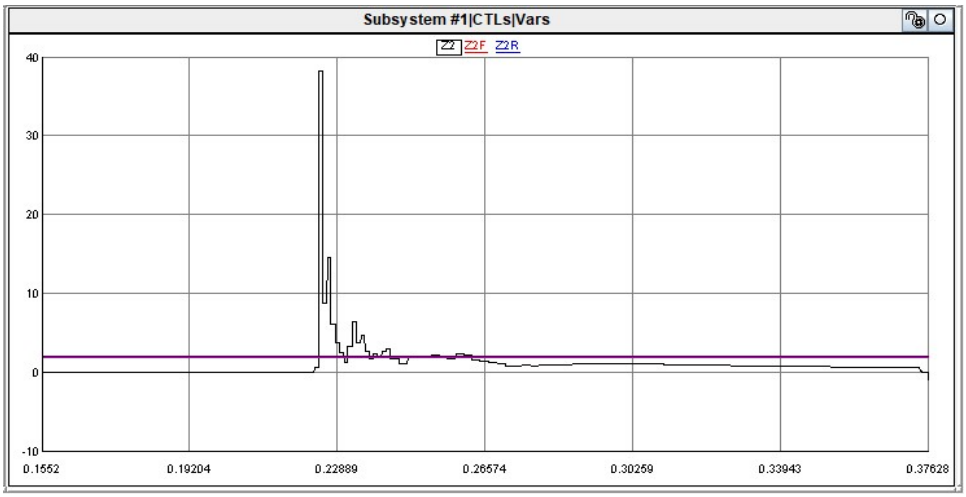

Z2 – Effective negative sequence secondary impedance
Z2F – Negative sequence forward threshold setting
Z2R – Negative sequence reverse threshold setting
Figure is zoomed in to show onset of the fault.

Figure 8-6. Effective negative sequence impedance for SLG fault.

The DC link voltage and the power dissipated by the resistor in the crowbar circuit of Type 3 WTG1 are shown in Figure 8-7 and Figure 8-8. The crowbar circuit dissipates 0.0178 MW power for the voltage of 4.22 kV, and as expected this power is greater than the theoretical result of 0.0176 MW for the threshold voltage setting described in Section 5.1.

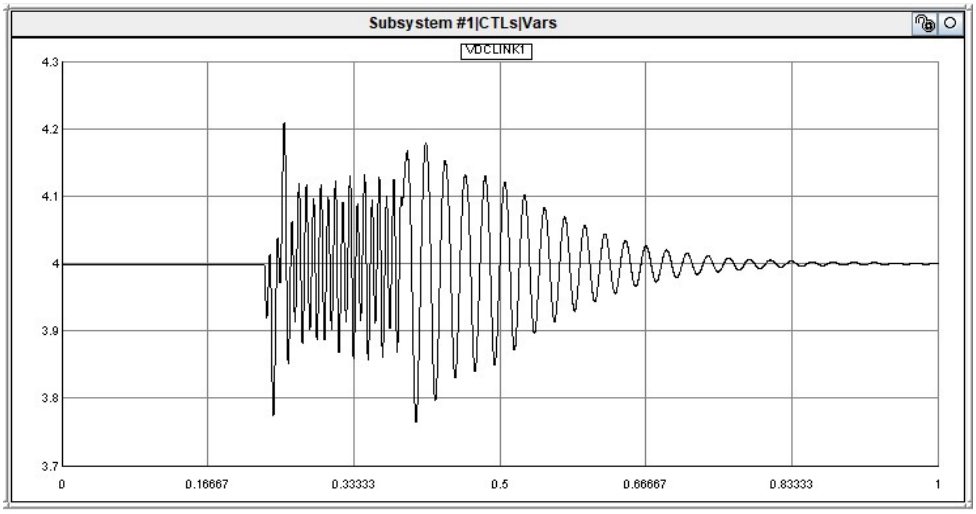

Figure 8-7. DC link voltage of Type 3 WTG for SLG fault.

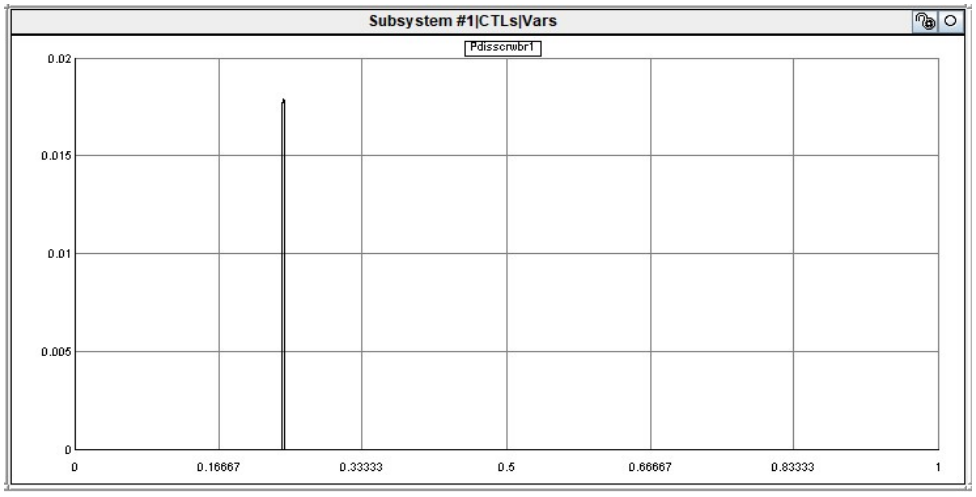

Figure 8-8. Power dissipated in the crowbar circuit of Type 3 WTG for SLG fault.

8.3.2 Line to Line (LL) Fault

Figure 8-9 shows the phase currents at the relay location for a B-phase to C-phase fault. The fault occurs at t=0.225 s and lasts for a period of 9 cycles. The fault current is not big enough for the phase overcurrent element 50P to pick up. However the negative sequence currents shown in Figure 8-10 is large enough for the negative sequence overcurrent element 50Q. Since the transformers of PVs and WTGs connected to the collector bus are delta configuration, the value of zero sequence current contributed by renewables is zero, so the ground element 50G will not respond for this fault. Figure 8-11 shows the line to ground voltages.

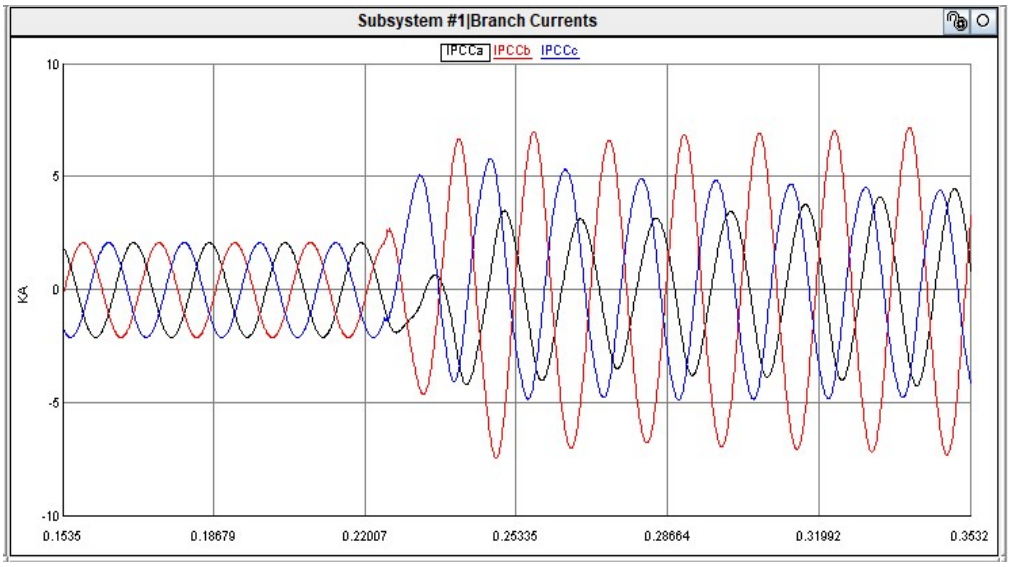

IPCCa, IPCCb, IPCCc – Current on phases A, B & C respectively
Figure is zoomed in to show onset of the fault.

Figure 8-9. Three-phase current at the relay location for LL fault.

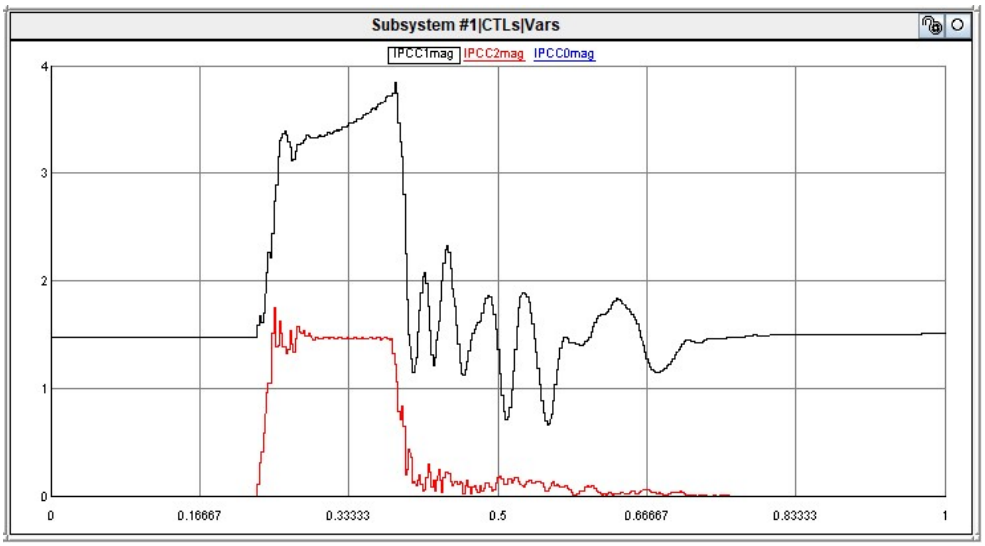

IPCC1mag – Positive sequence current magnitude
IPCC2mag – Negative sequence current magnitude
IPCC0mag – Zero sequence current magnitude

Figure 8-10. Sequence current magnitudes for LL fault.

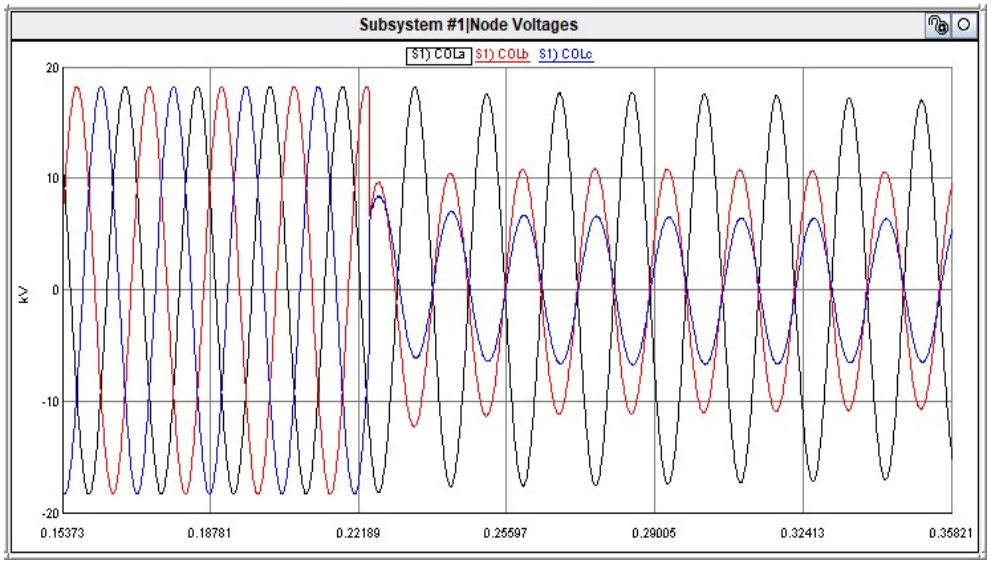

COLa, COLb, COLc – Voltage on phases A, B & C respectively
Figure is zoomed in to show onset of the fault.

Figure 8-11. Line to ground voltages at the relay location for LL fault.

The effective negative sequence impedance for LL fault shown in Figure 8-12 is above the reverse fault threshold, so this result can be used for negative-sequence directional element 32Q to declare a reverse fault.

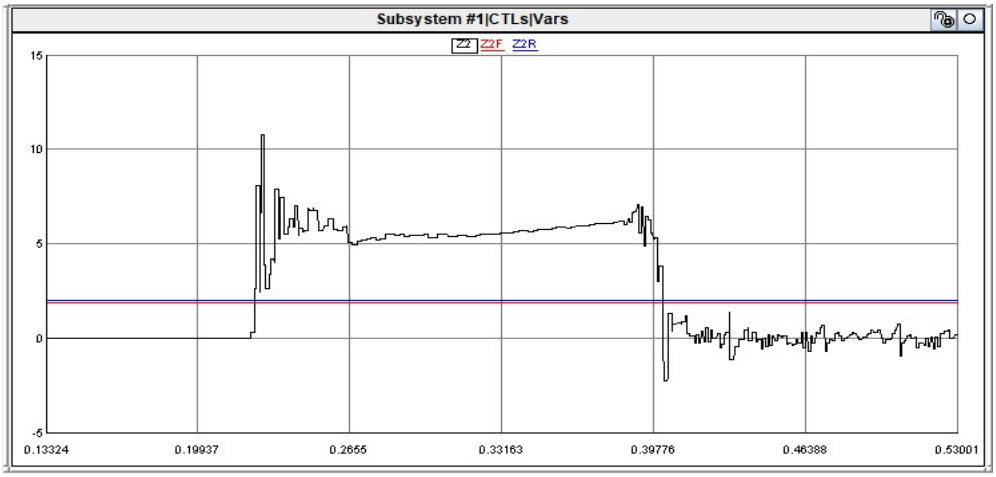

Z2 – Effective negative sequence secondary impedance
Z2F – Negative sequence forward threshold setting
Z2R – Negative sequence reverse threshold setting
Figure is zoomed in to show onset of the fault.

Figure 8-12. Effective negative sequence impedance for LL fault.

The DC link voltage and the power dissipated by the resistor in the crowbar circuit of Type 3 WTG1 for LL fault are shown in Figure 8-13 and Figure 8-14. The simulation result for the power has a minimum value 0.0178 MW during the fault condition, which is greater than the theoretical result 0.0176 MW for the threshold voltage setting as expected.

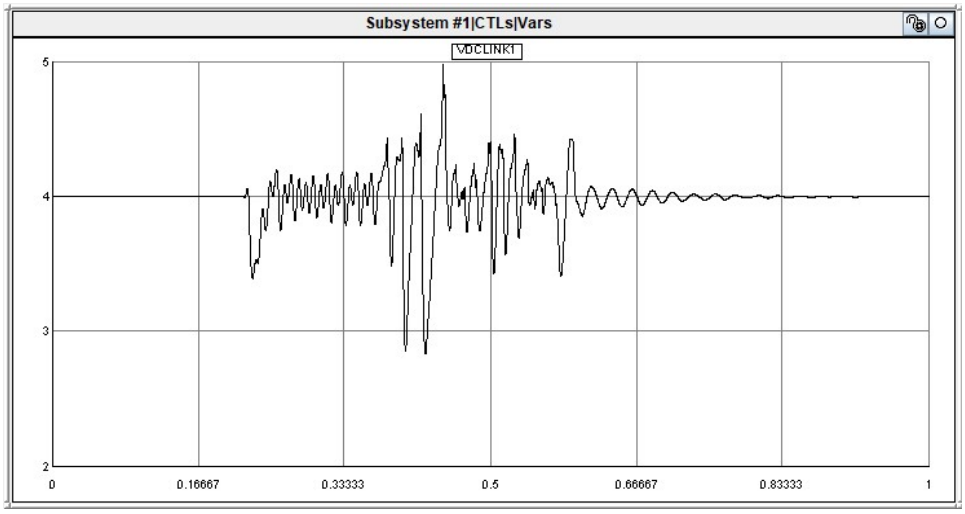

Figure 8-13. DC link voltage of Type 3 WTG for LL fault

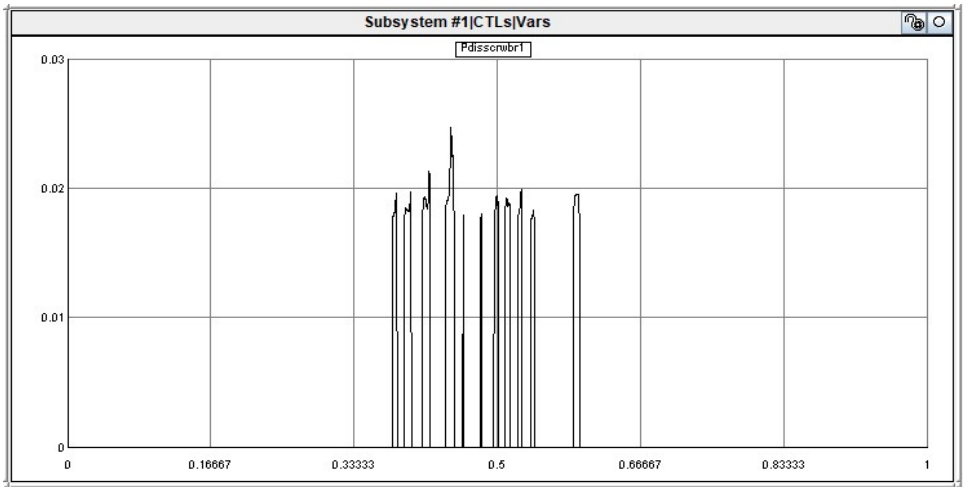

Figure 8-14. Power dissipated in the crowbar circuit of Type 3 WTG for LL fault.

8.3.3 Double Line to Ground (DLG) Fault

Figure 8-15 shows the phase currents at the relay location for a B-phase and C-phase to ground fault. The fault occurs at t=0.23 s and lasts for a period of 9 cycles. The fault current is not big enough for the phase overcurrent element 50P to pick up. However the sequence currents shown in Figure 8-16 show that the negative sequence current can be used for 50Q

element. Since there is no zero sequence current for the generators, the ground element 50G will not respond for this fault. Figure 8-17 shows the line to ground voltages.

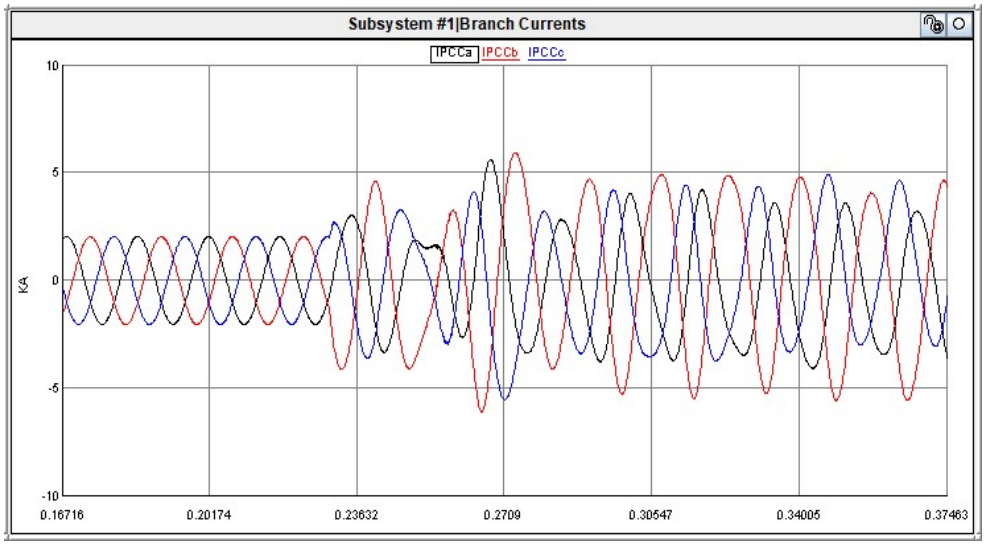

IPCCa, IPCCb, IPCCc – Current on phases A, B & C respectively
Figure is zoomed in to show onset of the fault.

Figure 8-15. Three-phase current at the relay location for DLG fault.

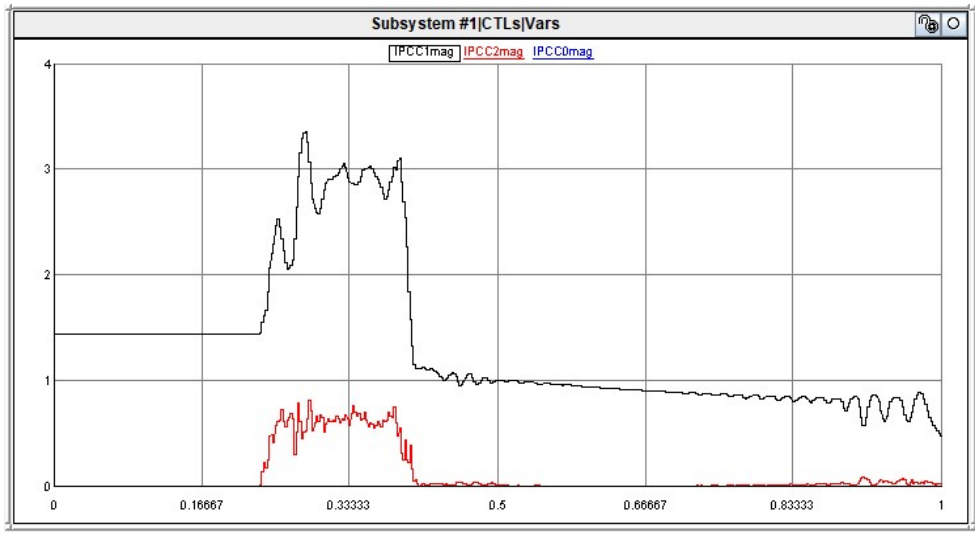

IPCC1mag – Positive sequence current magnitude
IPCC2mag – Negative sequence current magnitude
IPCC0mag – Zero sequence current magnitude

Figure 8-16. Sequence current magnitudes for DLG fault.

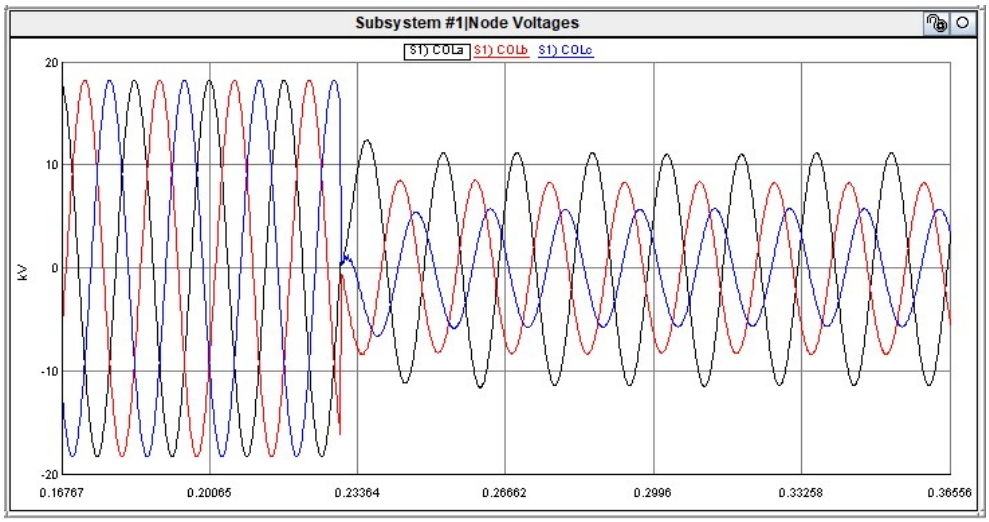

COLa, COLb, COLc – Voltage on phases A, B & C respectively
Figure is zoomed in to show onset of the fault.

Figure 8-17. Line to ground voltages at the relay location for DLG fault.

The effective negative sequence impedance for DLG fault shown in Figure 8-18 is above the reverse fault threshold, so this result can be used for negative-sequence directional element 32Q to declare a reverse fault.

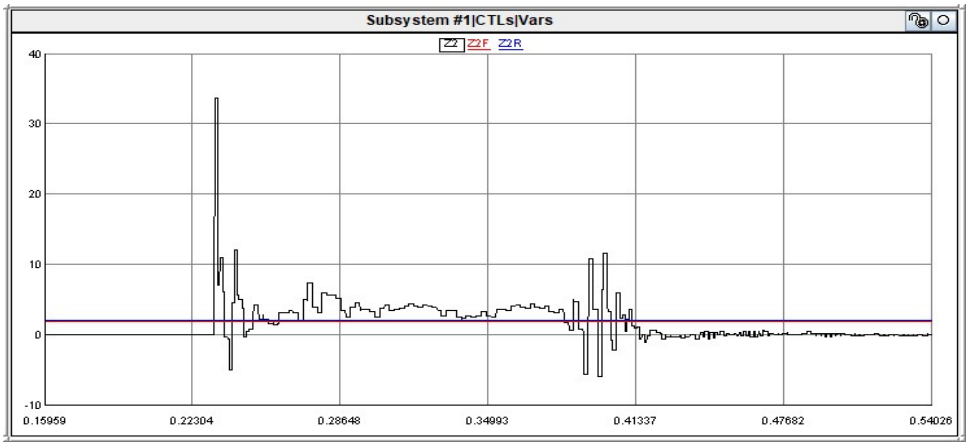

Z2 – Effective negative sequence secondary impedance
Z2F – Negative sequence forward threshold setting
Z2R – Negative sequence reverse threshold setting
Figure is zoomed in to show onset of the fault.

Figure 8-18. Effective negative sequence impedance for DLG fault.

The DC link voltage and the power dissipated by the resistor in the crowbar circuit of Type 3 WTG1 for DLG fault are shown in Figure 8-19 and Figure 8-20. The simulation result for the power has a minimum value 0.0177 MW during the fault condition, which is greater than the theoretical result 0.0176 MW for the threshold voltage setting as expected.

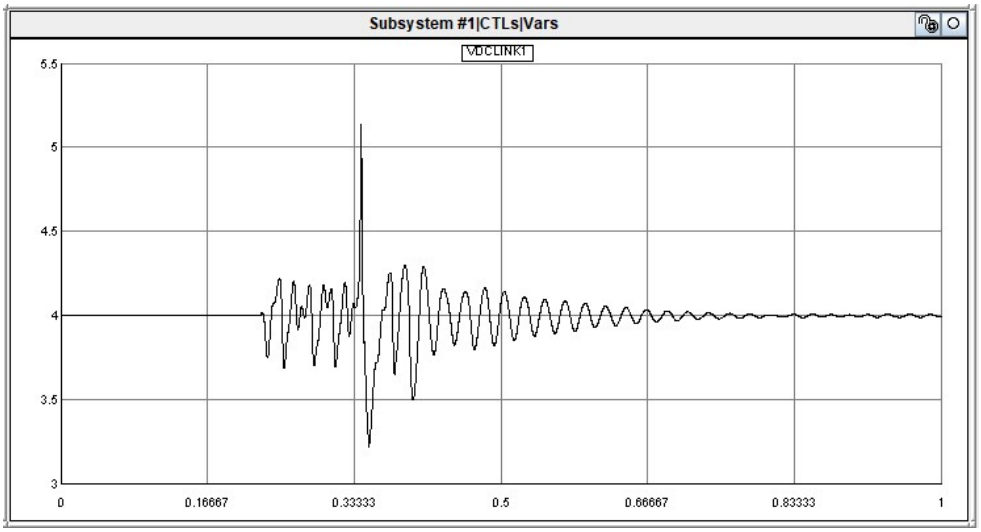

Figure 8-19. DC link voltage of Type 3 WTG for DLG fault.

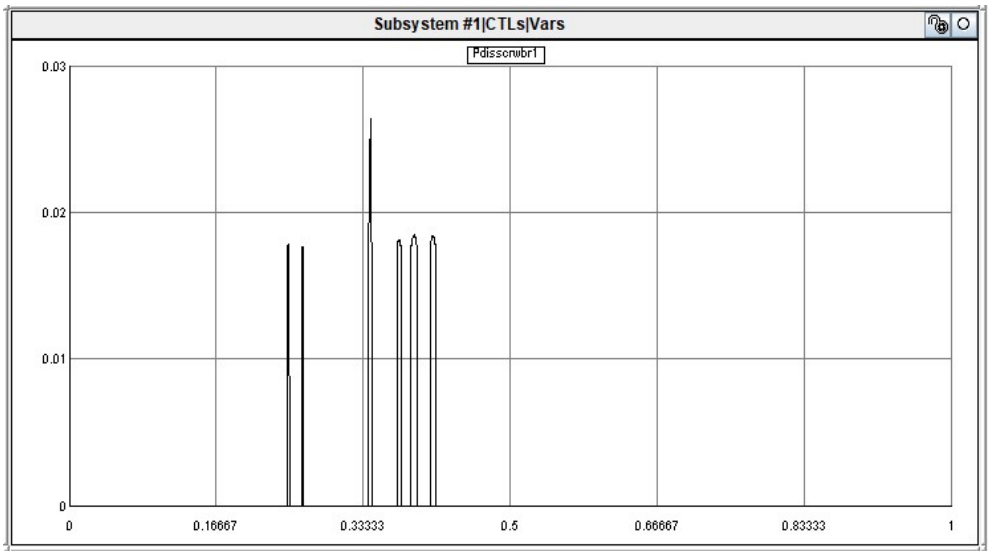

Figure 8-20. Power dissipated in the crowbar circuit of Type 3 WTG for DLG fault.

8.3.4 Three Phase Fault

Figure 8-21 shows the phase currents at the relay location for a balanced, three-phase fault. Figure 8-22 presents the sequence current magnitudes and Figure 8-23 shows the line to ground voltages. The fault occurs at t=0.218 s and lasts for a period of 9 cycles. The phase fault currents and voltages present the balanced fault characteristic, but the phase fault current is not big enough for the overcurrent element 50P to pick up. Compared to the three unbalanced faults discussed earlier, the sequence current transient response for the three-phase fault has more fluctuation, but it does not affect the relay operation since the positive sequence current threshold wound need to set similar to that of the element 50P. The fact that the negative sequence current is nearly zero verifies the three-phase balanced fault, which only has a positive sequence component.

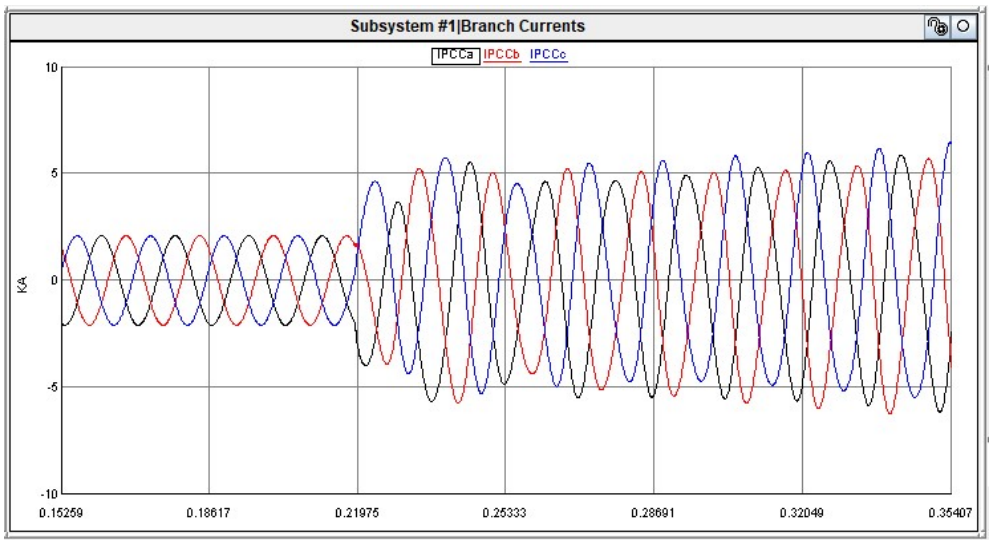

IPCCa, IPCCb, IPCCc – Current on phases A, B & C respectively
Figure is zoomed in to show onset of the fault.

Figure 8-21. Three-phase current at the relay location for three-phase fault.

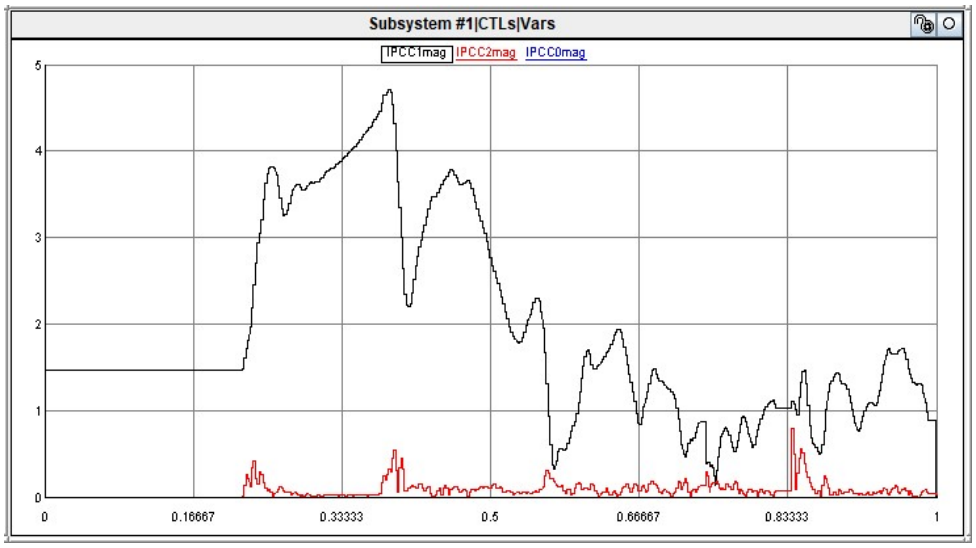

IPCC1mag – Positive sequence current magnitude
IPCC2mag – Negative sequence current magnitude
IPCC0mag – Zero sequence current magnitude

Figure 8-22. Sequence current magnitudes for three-phase fault.

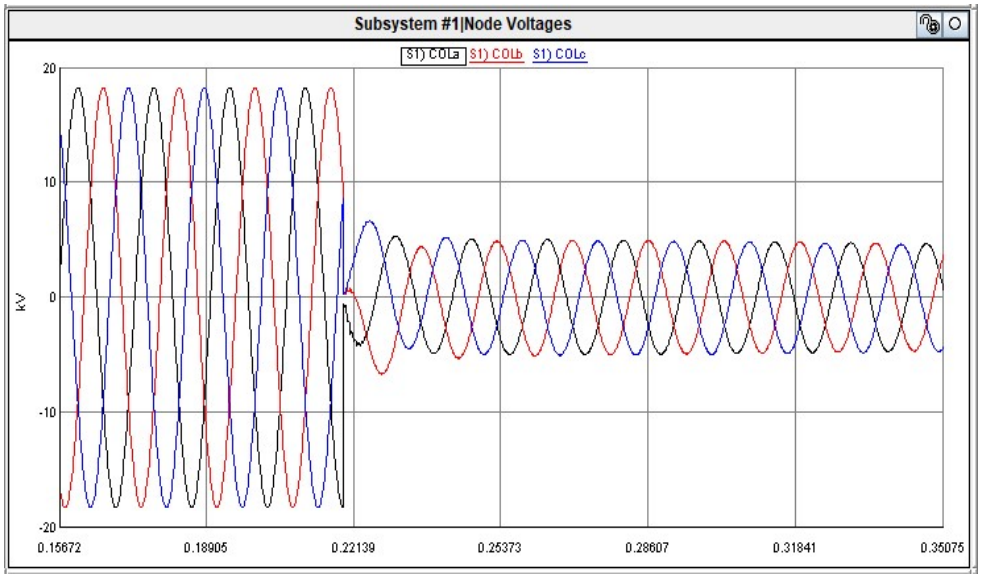

COLa, COLb, COLc – Voltage on phases A, B & C respectively
Figure is zoomed in to show onset of the fault.

Figure 8-23. Line to ground voltages at the relay location for three-phase fault.

The measured single phase positive impedance angle for three-phase fault shown in Figure 8-24 is below the reverse fault threshold, so this element can be used for a phase directional element 32P to declare a reverse fault.

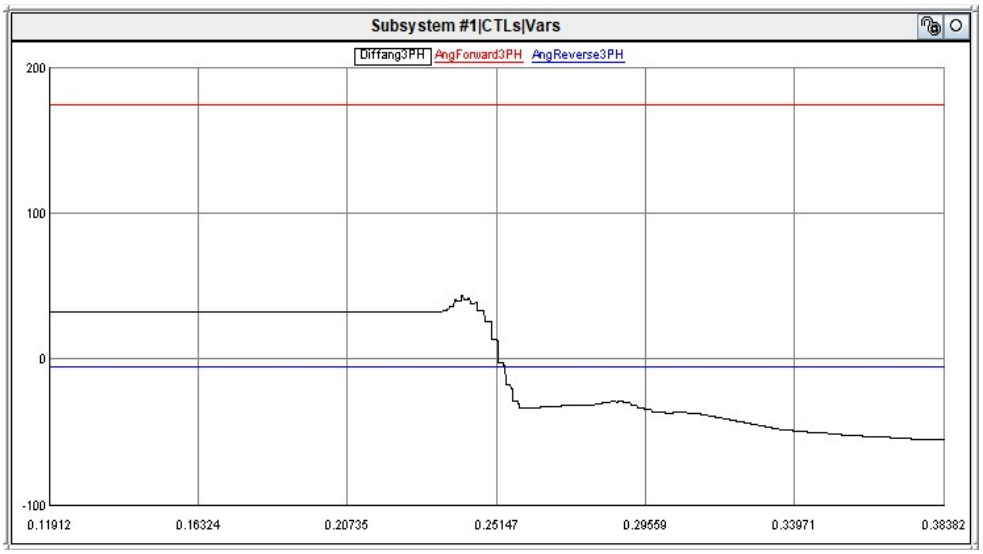

Diffang3PH – Measured single phase impedance angle
AngForward3PH – Forward threshold angle setting
AngReverse3PH – Reverse threshold angle setting
Figure is zoomed in to show onset of the fault.

Figure 8-24. Measured single phase impedance angle for three-phase fault.

The DC link voltage and the power dissipated by the resistor in the crowbar circuit of Type 3 WTG1 for three-phase fault are shown in Figure 8-25 and Figure 8-26. The simulation result for the power has a minimum value 0.0177 MW during the fault condition, which is greater than the theoretical result 0.0176 MW for the threshold voltage setting as expected.

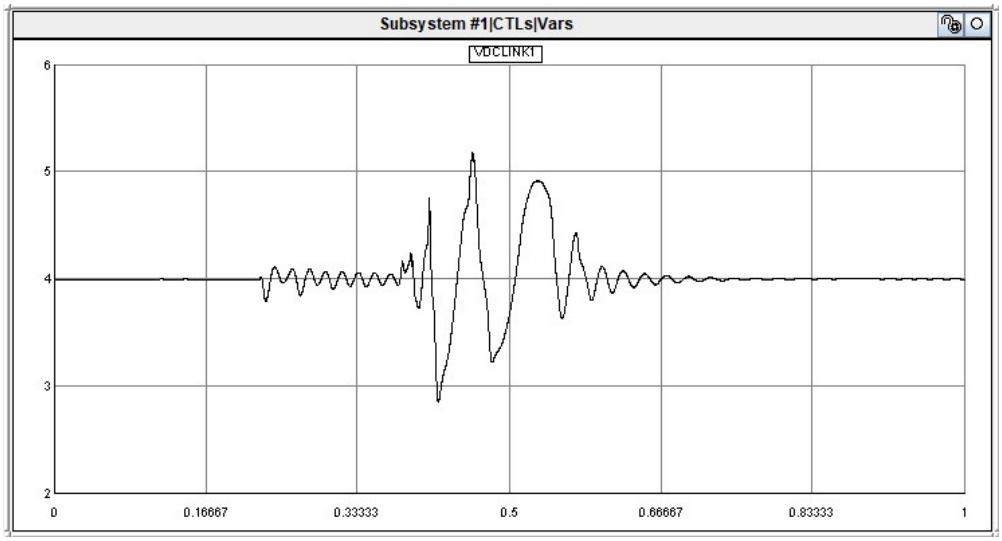

Figure 8-25. DC link voltage of Type 3 WTG for three-phase fault.

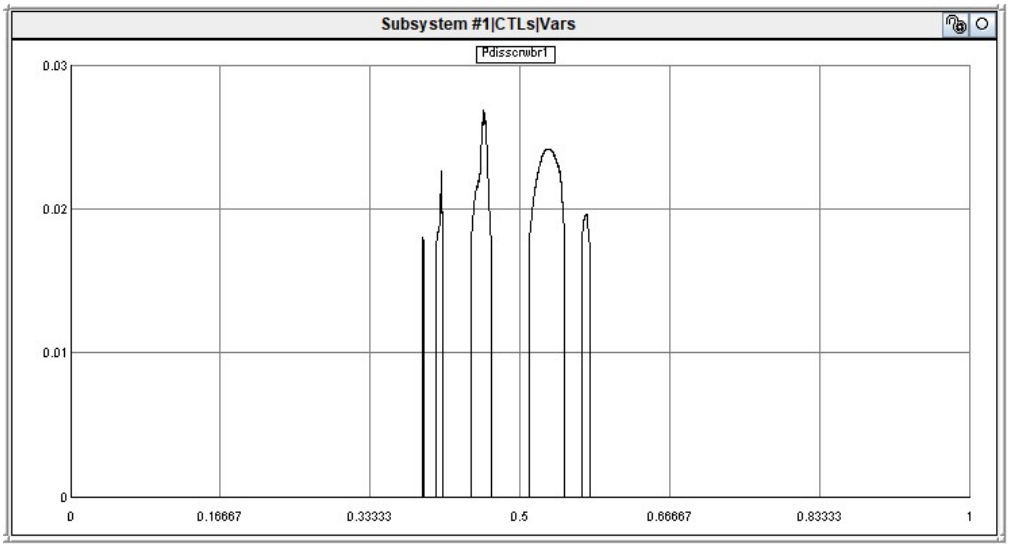

Figure 8-26. Power dissipated in the crowbar circuit of Type 3 WTG for three-phase fault.

8.4 System Response with Different Wind Speeds for Different WTGs

For a wind farm covering a large area, the wind turbines might not all operate in the same wind condition. It's necessary to investigate the effect on the protection performance from the different wind speeds for different turbines. In the integrated system with two PVs and five WTGs, one WTG is assumed to operate with higher wind speed, and the others with a lower

wind speed. The system response for normal operation and faults with mixed wind condition will be discussed in this section, and the fault scenarios applied in this section are same as those of Section 8.3.

8.4.1 Normal Operation with Different Wind Speeds

In RTDS the wind speed change can be implemented by changing the input mechanical torque to the DFIG machine of the Type 3 WTG. The RTDS induction machine component provides two modes to control the rotor speed, speed (free) mode and torque (lock) mode. In torque mode the mechanical torque is regulated by a control signal. This torque is used to calculate the rotor speed. The simulation results in the early sections are based on the default value of input mechanical torque, 1 pu, which can generate the same rotor speed with 1pu (10 m/s) wind speed when operated in speed mode. One of the five WTGs in the integrated system is changed to have 1.5 pu input mechanical torque, and the other four WTGs keep the torque at 1 pu. The insolation level still keeps 1000 w/m^2 and temperature 77 °F. Figure 8-27 shows the phase currents of WTG4 with 1 pu torque in steady-state, and the RMS current is 0.26 kA, which is same as that of WTG1 shown in Figure 6-12 in Section 6.3.1. Figure 8-28 presents the phase currents of WTG4 with 1.5 pu torque in steady-state, and the RMS current increases to 0.51 kA. The RMS phase currents at the PCC also rises to 1.55 kA shown in Figure 8-29. The power meters for each PV and WTG generator, and at the collector 22 kV bus are shown in Figure 8-30.

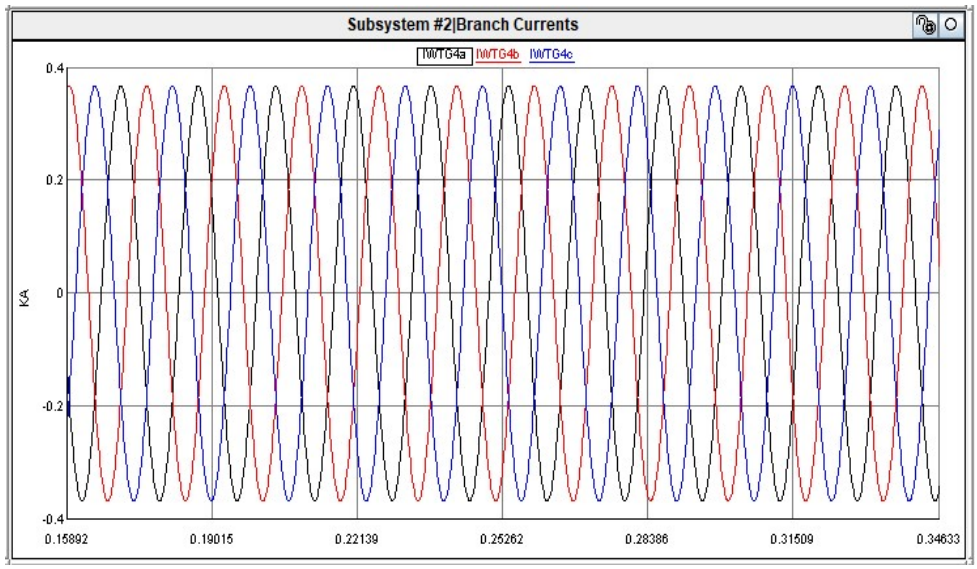

Figure 8-27. Three phase currents of WTG4 with 1pu torque in steady-state.

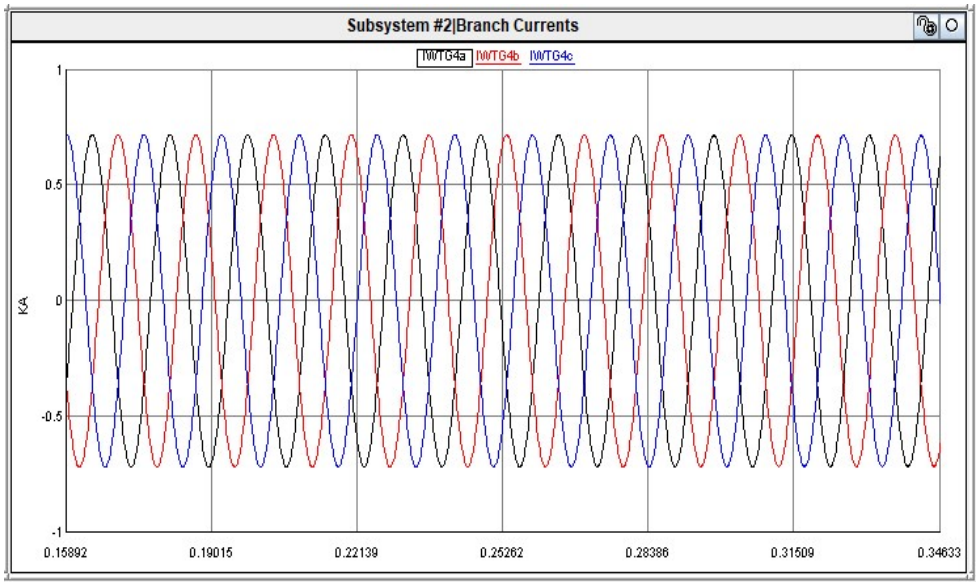

Figure 8-28. Three phase currents of WTG4 with 1.5pu torque in steady-state.

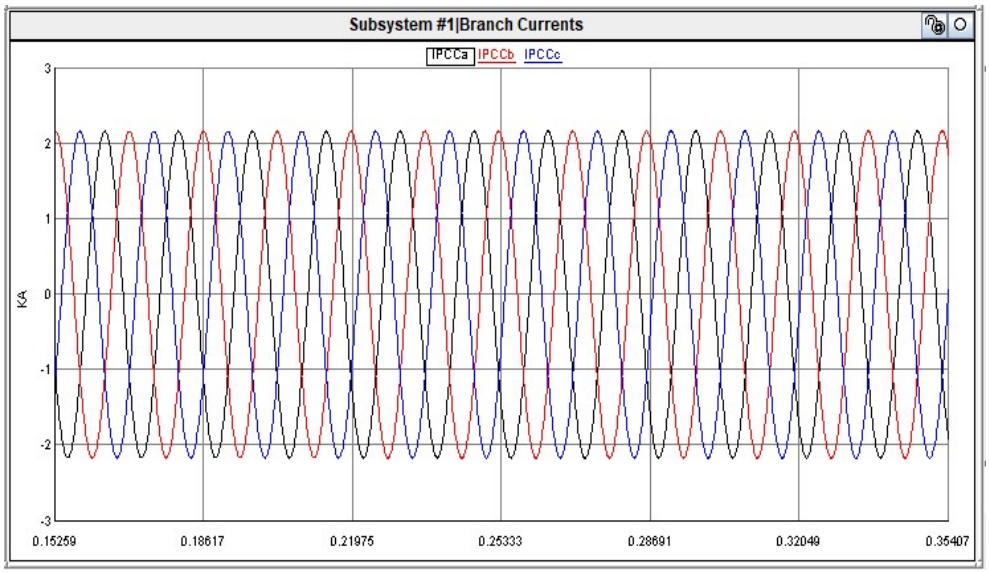

Figure 8-29. Three phase currents at the PCC with 1.5pu torque in steady-state.

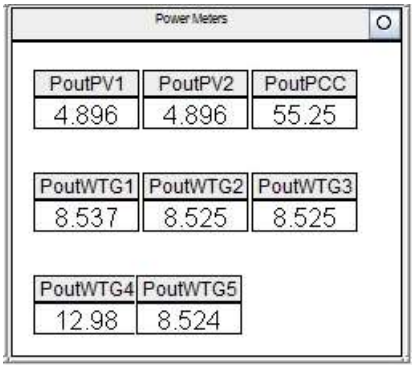

Figure 8-30. Power meters with 1.5pu torque in steady-state.

8.4.2 Single Line to Ground Fault

Figure 8-31 shows the phase currents at the relay location for an A-phase to ground fault at the designated fault location in Figure 8-1, and Figure 8-32 presents the sequence current magnitudes. Figure 8-33 shows the line to ground voltages. The fault occurs at t=0.23 s and lasts for a period of 9 cycles. Since the transient fault current is not significantly higher than the pre-fault load current, it is not possible to use 50P element for protection. The negative

sequence fault current can be used for 50Q element. Since there is no zero sequence current, the ground element 50G cannot be used.

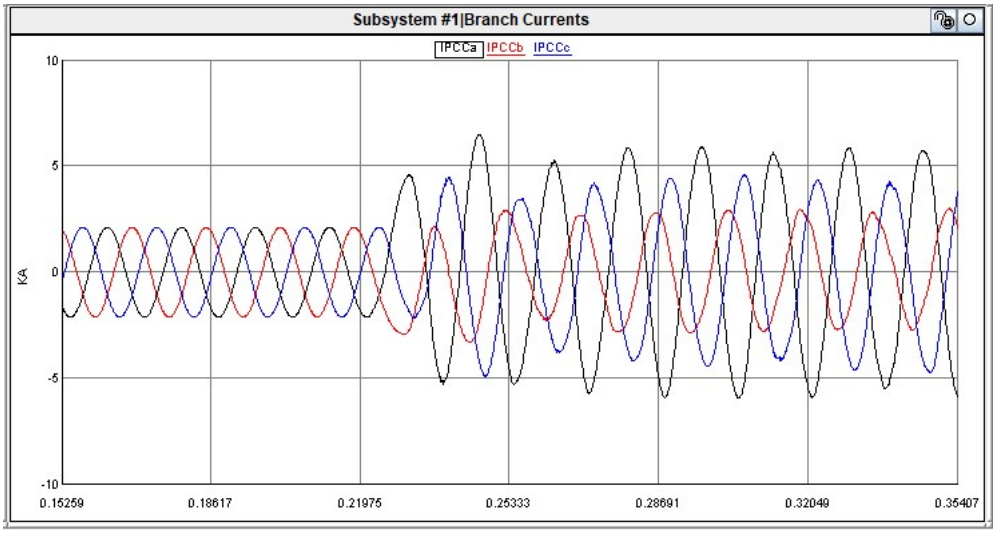

IPCCa, IPCCb, IPCCc – Current on phases A, B & C respectively
Figure is zoomed in to show onset of the fault.

Figure 8-31. Three-phase current at the relay location for SLG fault with mixed wind condition.

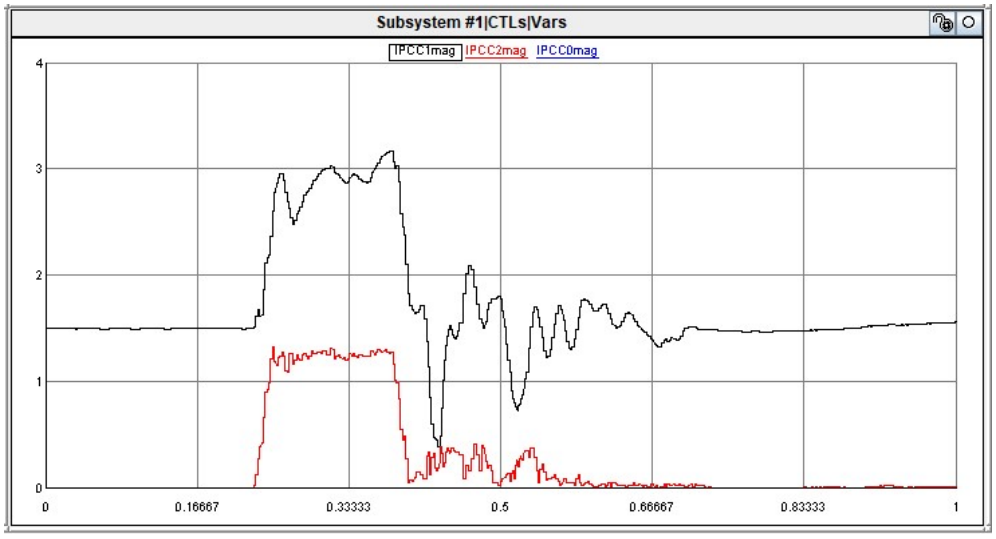

IPCC1mag – Positive sequence current magnitude
IPCC2mag – Negative sequence current magnitude
IPCC0mag – Zero sequence current magnitude

Figure 8-32. Sequence current magnitudes for SLG fault with mixed wind condition.

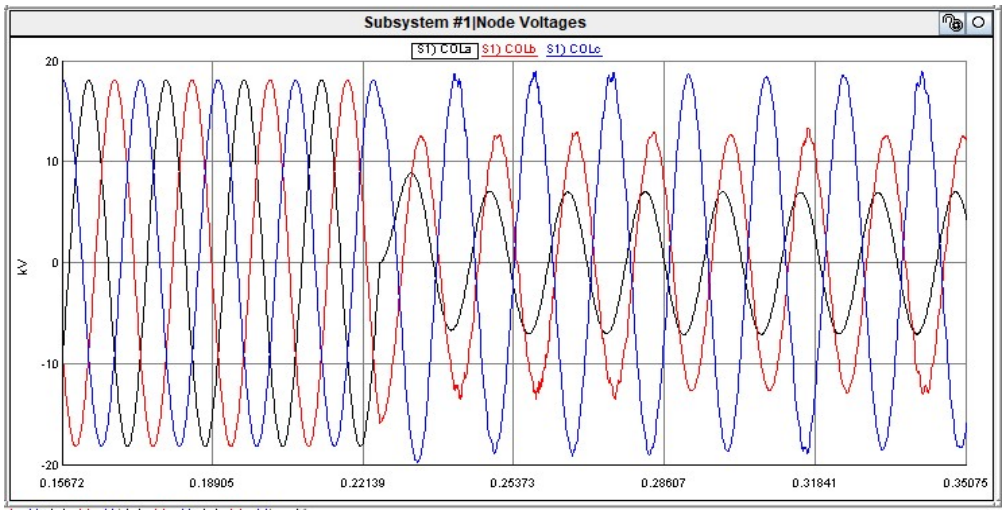

COLa, COLb, COLc – Voltage on phases A, B & C respectively
Figure is zoomed in to show onset of the fault.

Figure 8-33. LG voltages at the relay location for SLG fault with mixed wind condition.

The effective negative sequence impedance for SLG fault shown in Figure 8-34 is above the reverse fault threshold, so this result can be used for negative-sequence directional element 32Q to declare a reverse fault.

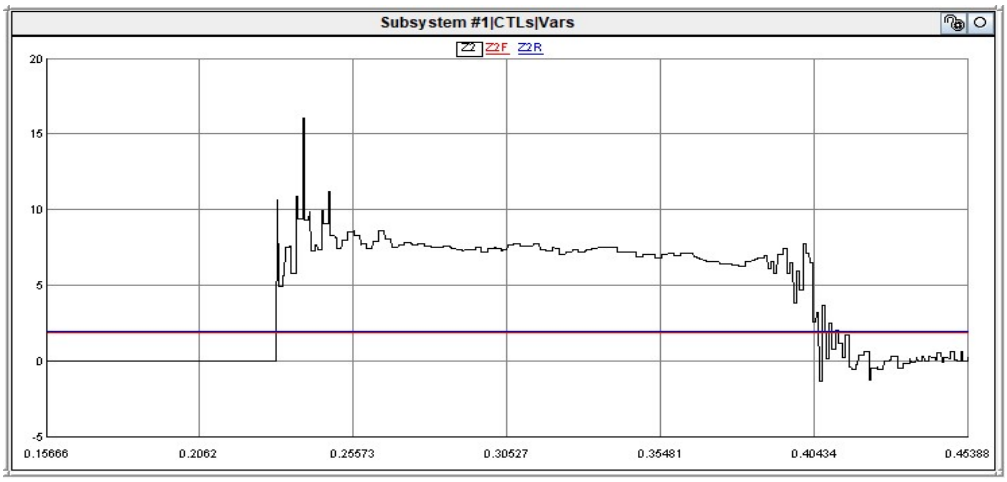

Z2 – Effective negative sequence secondary impedance
Z2F – Negative sequence forward threshold setting
Z2R – Negative sequence reverse threshold setting
Figure is zoomed in to show onset of the fault.

Figure 8-34. Effective negative sequence impedance for SLG fault with mixed wind condition.

8.4.3 Line to Line Fault

Figure 8-35 shows the phase currents at the relay location for a B-phase to C-phase fault. The fault occurs at t=0.23 s and lasts for a period of 9 cycles. Again fault current is not big enough for secure phase overcurrent element 50P to pick up. However the negative sequence current magnitude shown in Figure 8-36 is large enough for negative sequence overcurrent element 50Q. Since there is no zero sequence current, the ground element 50G cannot be used. Figure 8-37 shows the line to ground voltages.

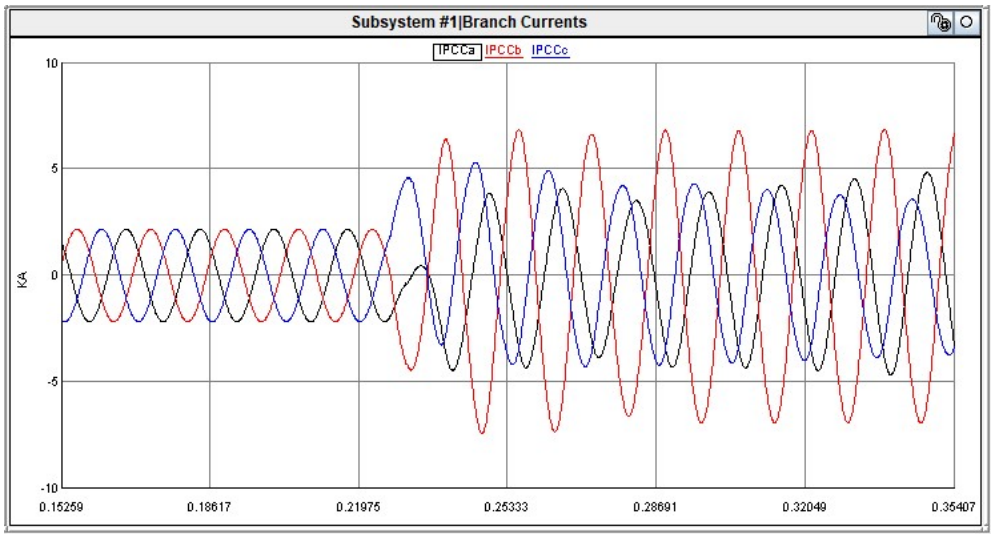

IPCCa, IPCCb, IPCCc – Current on phases A, B & C respectively
Figure is zoomed in to show onset of the fault.

Figure 8-35. Three-phase currents at the relay location for LL fault with mixed wind condition.

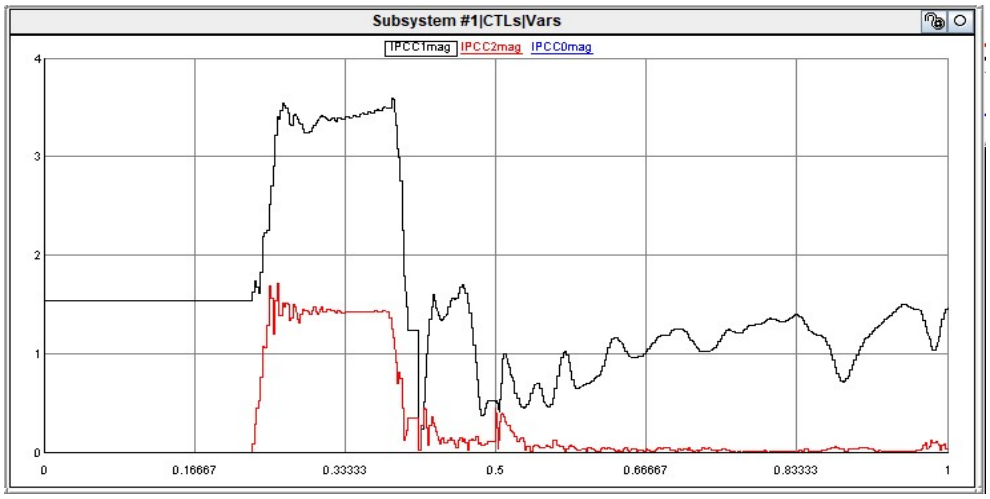

IPCC1mag – Positive sequence current magnitude
IPCC2mag – Negative sequence current magnitude
IPCC0mag – Zero sequence current magnitude

Figure 8-36. Sequence current magnitudes for LL fault with mixed wind condition.

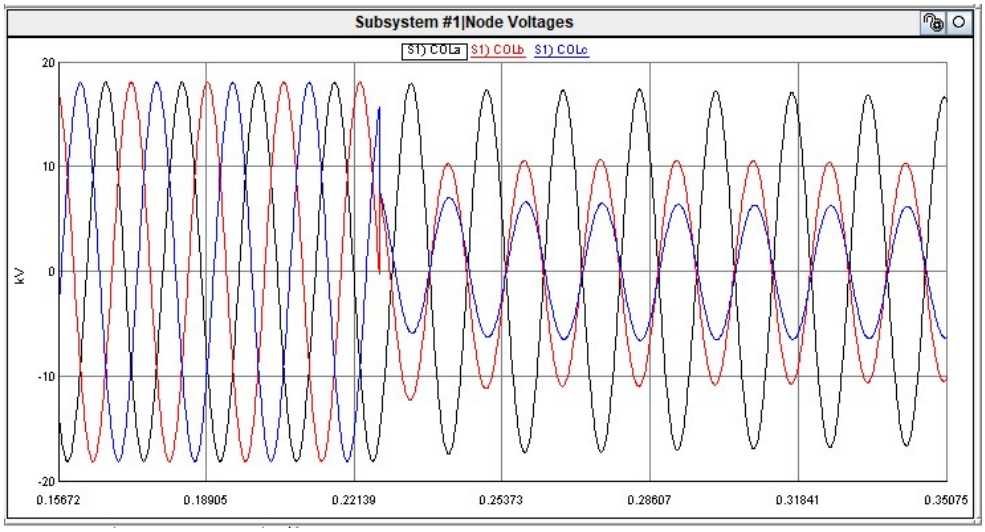

COLa, COLb, COLc – Voltage on phases A, B & C respectively
Figure is zoomed in to show onset of the fault.

Figure 8-37. LG voltages at the relay location for LL fault with mixed wind condition.

The effective negative sequence impedance calculated from the voltage and current measurement for LL fault shown in Figure 8-38 is above the reverse fault threshold, so the

negative sequence directional element 32Q can be used to declare reverse fault for this type of fault.

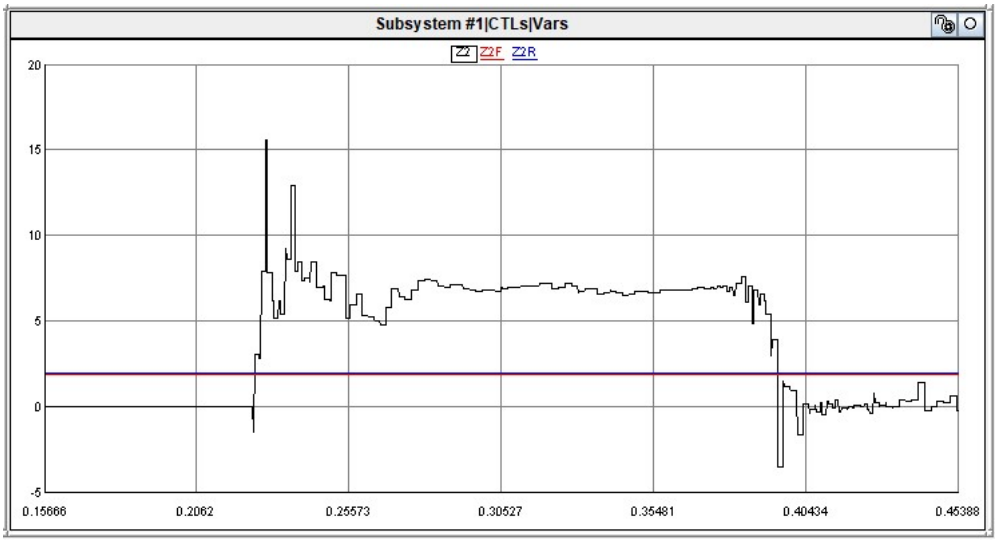

Z2 – Effective negative sequence secondary impedance
Z2F – Negative sequence forward threshold setting
Z2R – Negative sequence reverse threshold setting
Figure is zoomed in to show onset of the fault.

Figure 8-38. Effective negative sequence impedance for LL fault with mixed wind condition.

8.4.4 Double Line to Ground Fault

Figure 8-39 shows the phase currents at the relay location for a B-phase to C-phase to ground fault. The fault occurs at t=0.23 s and lasts for a period of 9 cycles. The fault current is not big enough for the phase overcurrent element 50P to pick up. The negative sequence current magnitude shown in Figure 8-40 can be used for 50Q element to pick up. Since there is no zero sequence current, the ground element 50G does not respond for this fault. Figure 8-41 shows the line to ground voltages.

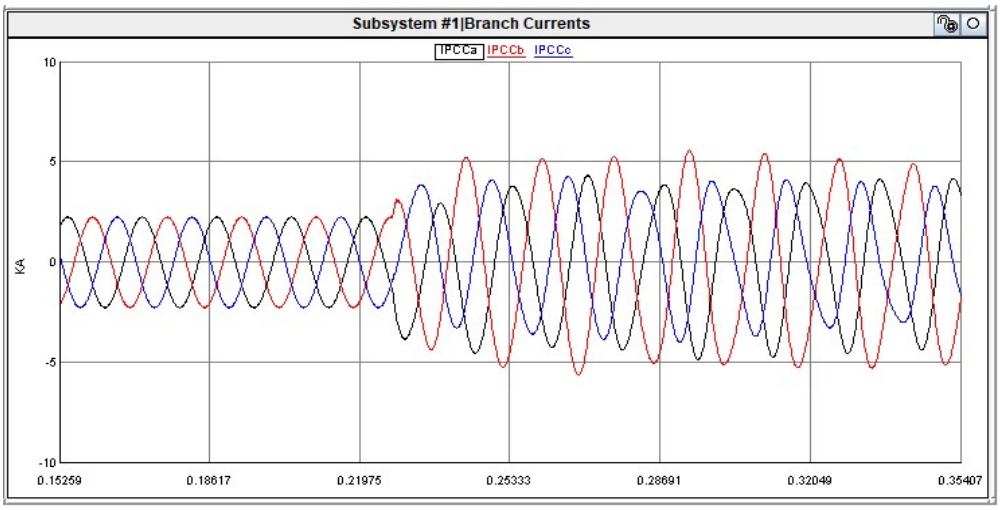

IPCCa, IPCCb, IPCCc – Current on phases A, B & C respectively
Figure is zoomed in to show onset of the fault.

Figure 8-39. Three-phase currents at the relay location for DLG fault with mixed wind condition.

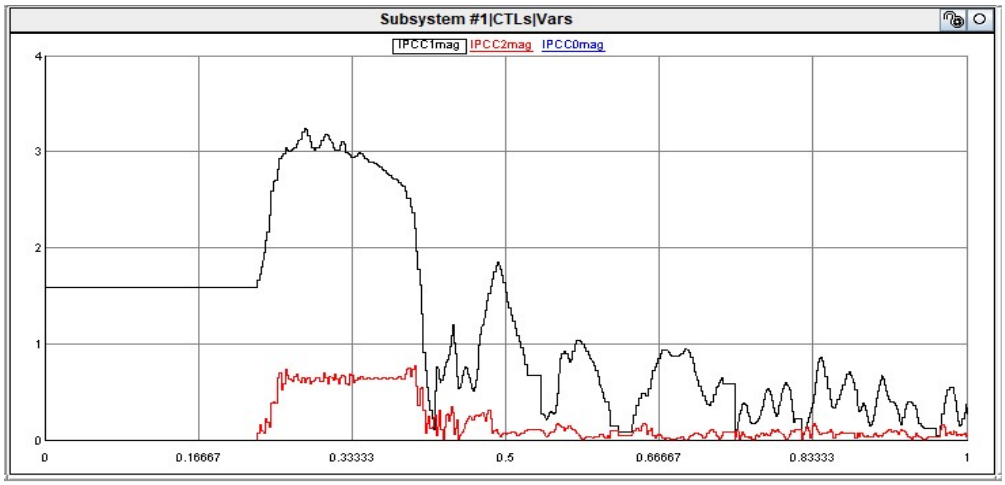

IPCC1mag – Positive sequence current magnitude
IPCC2mag – Negative sequence current magnitude
IPCC0mag – Zero sequence current magnitude

Figure 8-40. Sequence current magnitudes for DLG fault with mixed wind condition.

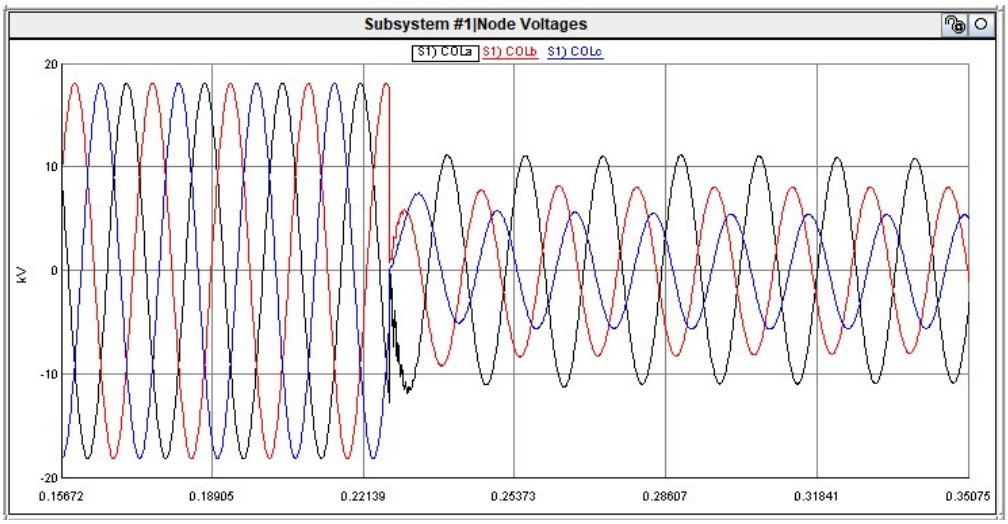

COLa, COLb, COLc – Voltage on phases A, B & C respectively
Figure is zoomed in to show onset of the fault.

Figure 8-41. LG voltages at the relay location for DLG fault with mixed wind condition.

The effective negative sequence impedance for the DLG fault shown in Figure 8-42 is above the reverse fault threshold, so this result can be used for the negative sequence directional element 32Q to declare a reverse fault.

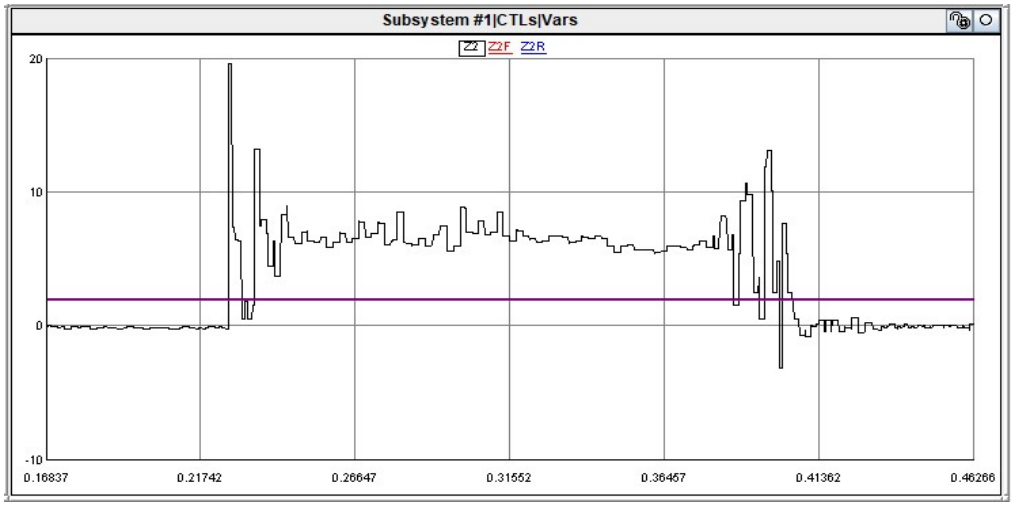

Z2 – Effective negative sequence secondary impedance
Z2F – Negative sequence forward threshold setting
Z2R – Negative sequence reverse threshold setting
Figure is zoomed in to show onset of the fault.
Figure 8-42. Effective negative sequence impedance for DLG fault with mixed wind condition.

8.4.5 Three Phase Fault

Figure 8-43 shows the phase currents at the relay location for a balanced fault, three-phase fault. Figure 8-44 presents the sequence current magnitudes, and Figure 8-45 shows the line to ground voltages. The fault occurs at t=0.23 s and lasts for a period of 9 cycles. The fault currents and voltages present a balanced fault characteristic, but the phase fault currents are not big enough for the phase overcurrent element 50P to pick up. Similar with the case of three-phase fault with identical wind condition, the positive sequence current magnitude with mixed wind condition as shown in Figure 8-44 suffers more fluctuation in its transient response, but it does not affect the relay operation since the positive sequence current threshold would need to set similar to that of the 50P element.

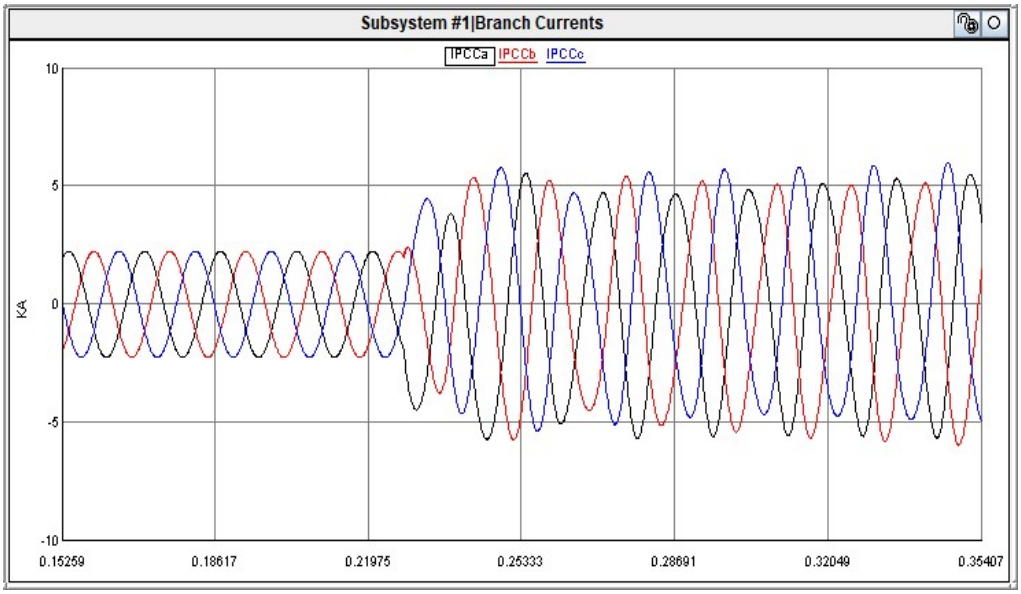

IPCCa, IPCCb, IPCCc – Current on phases A, B & C respectively
Figure is zoomed in to show onset of the fault.

Figure 8-43. Three-phase currents at the relay location for three-phase fault with mixed wind condition.

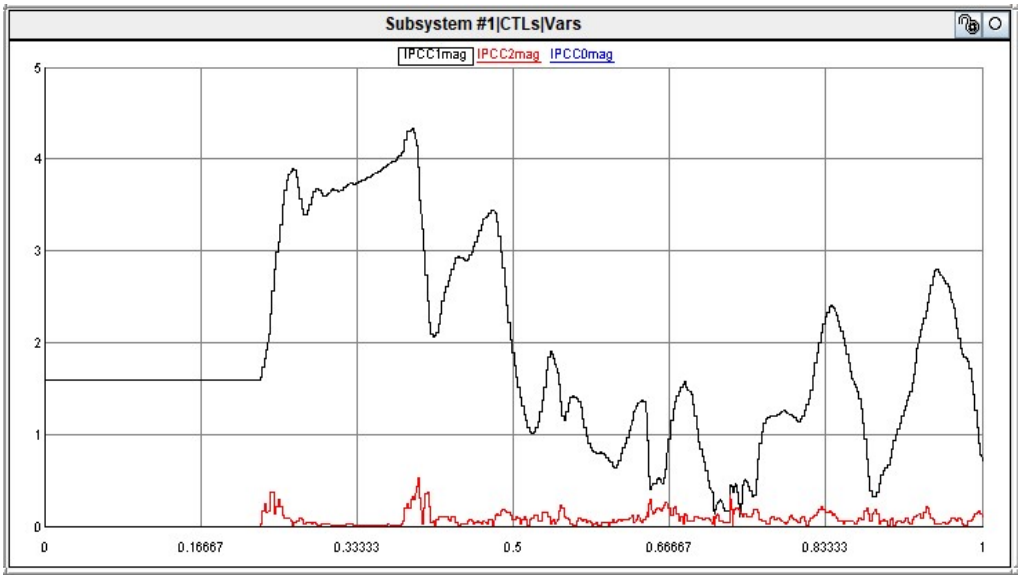

IPCC1mag – Positive sequence current magnitude
IPCC2mag – Negative sequence current magnitude
IPCC0mag – Zero sequence current magnitude

Figure 8-44. Sequence current magnitudes for three-phase fault with mixed wind condition.

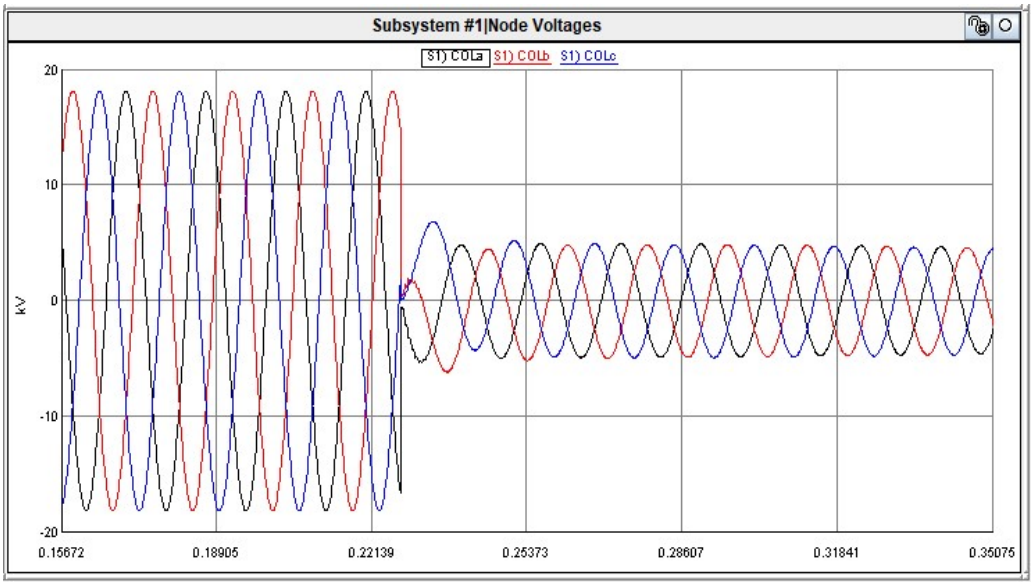

COLa, COLb, COLc – Voltage on phases A, B & C respectively
Figure is zoomed in to show onset of the fault.

Figure 8-45. LG voltages at the relay location for three-phase fault with mixed wind condition.

The measured single phase positive impedance angle for three-phase fault shown in Figure 8-46 is below the reverse fault threshold, so this element can be used for a phase directional element 32P to declare a reverse fault.

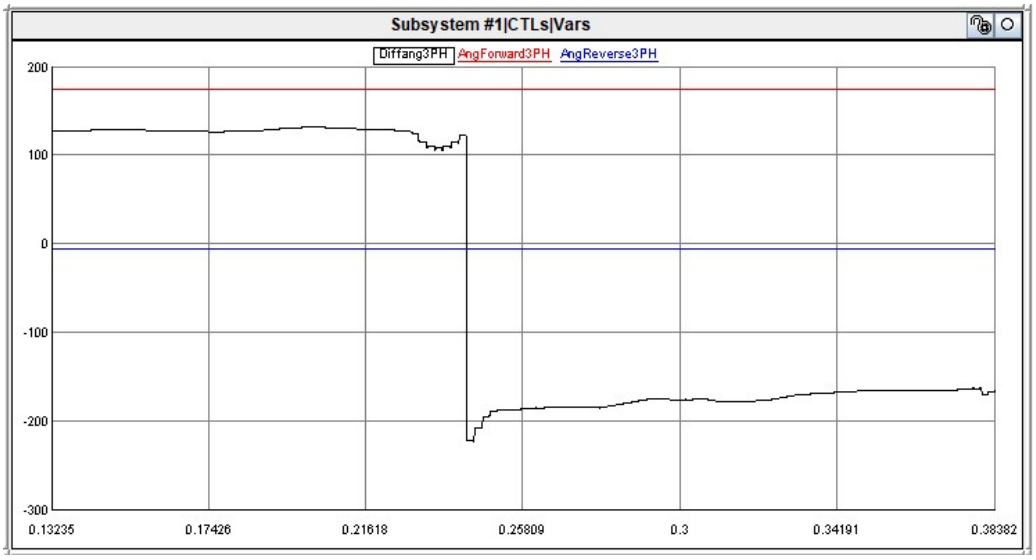

Diffang3PH – Measured single phase impedance angle
AngForward3PH – Forward threshold angle setting
AngReverse3PH – Reverse threshold angle setting
Figure is zoomed in to show onset of the fault.

Figure 8-46. Measured single phase impedance angle for three-phase fault with mixed wind condition.

8.5 Protection Performance Summary

For the faults that happen near the 22 kV collector bus, the performance of overcurrent protection on the collector feeder can be summarized in Table 8-1 based on the analysis of the simulation results. In the table "Y" represents that the element can be used to pick up the fault, and "N/A" means that the element should not be applied for the type of fault.

Table 8-1. Summary of the response of protection scheme.

Type of Fault		Identical wind condition					Mixed wind condition				
		50P	50Q	50G	30P	30Q	50P	50Q	50G	30P	30Q
Unbalanced fault	SLG (A-G)	N/A	Y	N/A	N/A	Y	N/A	Y	N/A	N/A	Y
	LL (B-C)	N/A	Y	N/A	N/A	Y	N/A	Y	N/A	N/A	Y
	BLG (BC-G)	N/A	Y	N/A	N/A	Y	N/A	Y	N/A	N/A	Y
Balanced fault	3 phase (ABCG)	N/A	N/A	N/A	Y	N/A	N/A	N/A	N/A	Y	N/A

From the response of relays in Table 8-1, the negative sequence overcurrent element 50Q and directional element 32Q can be used for unbalanced faults and the phase directional element 32P can be applied to balanced three-phase fault.

8.6 Summary

In this chapter, the protection scheme performance on the collector feeder of the system integrated with two PVs and five WTGs is discussed. The simulation results of the system response to unbalanced and balanced faults show the good performance of overcurrent protection scheme on the 22 kV collector feeder, and negative sequence overcurrent element 50Q and directional element 32Q can be used for unbalanced faults and phase directional element 32P for balanced three-phase fault. The protection scheme is also verified with the fault responses when different wind speeds among WTGs, and the same protection performance is achieved.

Chapter 9 Summary, Conclusions and Future Work

9.1 Summary

A system with PV inverters and Type 3 WTGs integrated on the same collector bus is studied in this thesis. A PV model is developed and control strategies for grid connected VSC are designed. An averaged VSC model is implemented. The real power characteristic of the PV model with daily insolation and temperature in steady-state is investigated by simulation in RTDS/RSCAD and post-processing in MATLAB. A Type 3 WTG is also developed using averaged VSC model.

For the study of protection, an integrated system with two PV inverters and five Type 3 WTGs is considered and an overcurrent protection scheme using symmetrical components on the collector feeder is investigated with simulation results. The protection scheme performance is also verified with the fault responses when different wind speeds are among WTGs.

9.2 Conclusions

The integrated system modeled in this thesis shows a flexible expansion feature that allows it to integrate different amount of PVs and Type 3 WTGs on the same collector bus according to the geographical and climate conditions. This integration method also shows the complementary benefits of having a mix of different types of generation on the same collector.

The test for the real power characteristic of the PV model shows that insolation level is the dominant parameter to affect the real power production of PV model.

The protection performance study for the integrated system with two PVs and five Type 3 WTGs shows the good performance of a sequence current based overcurrent protection scheme on the collector feeder, and negative sequence overcurrent element 50Q and directional

element 32Q can be used for unbalanced faults and phase directional element 32P for balanced three-phase fault. The protection scheme was also verified with the fault responses when different wind speeds are present among WTGs, where the same protection performance was achieved. This protection performance study also shows that the collector feeder protection is not affected by having different types of renewable generation with different fault characteristics integrated together.

9.3 Future Work

Based on the PV model used in this research and the integrated system with PVs and WTGs, further studies on the model and the performance of different protection schemes are proposed to the following.

- Use single diode PV cell model to build a PV array instead of using the default RSCAD PV array component. Use MATLAB script to get the current-voltage (I-V) characteristic of the PV cell with the variation of solar insolation and temperature, and generate corresponding MPPT data to apply in the converter controls.
- Design and implement the functions of islanding detection, and implement an anti-islanding protection scheme.
- Add GTAO or GSE component into the integrated system circuit in RSCAD and connect the RTDS to a commercial relay to verify the protection scheme performance.
- Model the integrated system with the realistic line length in collector feeders in other simulation tools, such as PSCAD/EMTDC, ATP, or EMTP-RV and determine if the same level of protection performance is still achieved.

• Develop and apply protection schemes for other fault locations, including on the transmission line, as well as dc fault locations inside the PV generator, such as PV array and inside the converter.

• Improve the AC grid model with a more detailed system model plus more detailed source and load models, instead of an ideal AC source. Investigate performance of protection schemes on the transmission line with this model. Frequency droop control tests and reactive power and voltage control tests to evaluate response of control system.

References

[1] BP Plc., *BP Statistical Review of World Energy*, June 2018.

[2] SRE Team, *When Will Fossil Fuels Run Out? All About Fossil Fuel Sustainability,* [Online], Available: https://www.survivalrenewableenergy.com/when-will-fossil-fuels-run-out/, February 2019.

[3] IRENA, IEA and REN21, *Renewable Energy Policies in a Time of Transition,* 2018.

[4] McKinsey Energy Insights, *Global Energy Perspective 2019 Reference Case Summary*, January 2019.

[5] *PV education*, [Online], Available: https://www.pveducation.org, March 2019.

[6] *Solar (PV) Cell Module, Array* [Online], Available: http://www.samlexsolar.com/learning-center/solar-cell-module-array.aspx, March 2019.

[7] S. Gupta, H. Tiwari, M. Fozdar, and V. Chandna, "Development of a Two Diode Model for Photovoltaic Modules Suitable for Use in Simulation Studies," in APPEEC, Shanghai, China, March 2012.

[8] Fayad Abdulal, Nader Anani, and Nick Bowring, "Comparative Modelling and Parameter Extraction of a Single- and Two-diode Model of a Solar Cell," 2014 9th International Symposium on Communication Systems, Networks & Digital Sign, 23-25 July 2014.

[9] Simon Lineykin, Moshe Averbukh and Alon Kuperman, "Five-parameter model of photovoltaic cell based on STC data and dimensionless," 2012 IEEE 27th Convention of Electrical and Electronics Engineers in Israel, 14-17 Nov. 2012.

[10] Md Tofael Ahmed, Teresa Goncalves, Mouhaydine Tlemcani, "Single Diode Model Parameters Analysis of Photovoltaic Cell," IEEE International Conference on Renewable Energy Research and Applications (ICRERA) in Birmingham, UK, 20-23 Nov. 2016.

[11] RTDS technologies. *Real time digital simulator manuals*, July 2013.

[12] Syed Islam, "Challenges and opportunities in grid connected commercial scale PV and wind farms." IEEE 9th International Conference on Electrical and Computer Engineering (ICECE), Dhaka, Bangladesh, 20-22 December, 2016.

[13] Remus Teodorescu, Marco Liserre and Pedro Rodriguez: *Grid Converters for Photovoltaic and Wind Power Systems*. Wiley, 2011.

[14] NREL News, *Ten Years of Analyzing the Duck Chart*. [Online], Available: https://www.nrel.gov/news/program/2018/10-years-duck-curve.html, Feb. 26, 2018.

[15] Han Chen, Chunlin Guo, Jianting Xu and Pengxin Hou, "Overview of Sub-synchronous Oscillation in Wind Power System." Energy and Power Engineering, Page(s): 454-457, May 2013.

[16] Bin Wu, Yongqiang Lang, Navid Zardari and Samir Kouro, *Power conversion and control of wind energy systems*, New Jersey: John Wiley & Sons, Inc., 2011.

[17] Reza Iravani and Amirnaser Yazdani, *Voltage-Sourced Converters in Power Systems*, New Jersey: John Wiley & Sons, Inc., 2010.

[18] *Torque Slip Characteristic*, [Online], Available, http://www.eeeguide.com/torque-slip-characteristic/, September, 2016.

[19] Dean Miller, "Fault Current Contributions from Wind Plants," 2012 IEEE Power & Energy Society General Meeting, San Diego, California USA, 22–27 July 2012.

[20] IEEE PES Wind Plant Collector System Design Working Group, "Characteristics of wind turbine generators for wind power plants," 2009 IEEE Power & Energy Society General Meeting, Calgary, AB, Canada, 26-30 July 2009.

[21] David Wenzhong Gao, Eduard Muljadi, Tian Tian, Mackay Miller and Weisheng Wang, *Comparison of Standards and Technical Requirements of Grid Connected Wind Power Plants in China and the United States*, Technical Report NREL/TP-5D00-64225, September 2016.

[22] Abishek Mann, Amit Karalkar, Lili He and Morris Jones, "The Design of A Low-Power Low-Noise Phase Lock Loop," 2010 11th International Symposium on Quality Electronic Design, San Jose, CA, USA, 22-24 March 2010.

[23] Amirnaser Yazdani, Prajna Paramita Dash, "A Control Methodology and Characterization of Dynamics for a Photovoltaic (PV) System Interfaced With a Distribution Network," IEEE Transactions on Power Delivery, Page(s): 1538 – 1551, Volume: 24, Issue: 3, July 2009.

[24] Rishabh Jain, Herbert L. Hess and Brian K. Johnson, "DFIG based wind turbine system modeling in the Real Time Digital Simulator," 2014 North American Power Symposium, Pullman, WA, USA, 7-9 Sept. 2014.

[25] National Solar Radiation Data Base, [Online], Available: https://rredc.nrel.gov/solar/old_data/nsrdb/1991-2010/, March 2019.

[26] Past Weather in Moscow, Idaho, USA. [Online], Available: https://www.timeanddate.com/weather/usa/moscow/historic?month=8&year=2010, March 2019.

[27] J.C. Das: *Power System Protective Relaying*. CRC Press, Taylor & Francis Group, 2018.

[28] Jeff Roberts and Armando Guzman, "Directional Element Design and Evaluation", 49th Annual Georgia Tech Protective Relaying Conference, May 1995.